



LIBRARY  
Michigan State  
University

This is to certify that the

dissertation entitled

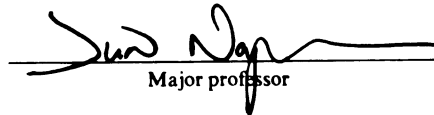
SCANNING TUNNELING MICROSCOPY  
STUDY OF Dy,Gd DISILICIDE NANOSTRUCTURES ON Si (001)

presented by

Bangzhi Liu

has been accepted towards fulfillment  
of the requirements for

Ph.D. degree in Materials Science  
and Engineering

  
Major professor

Date 12/12/02

**PLACE IN RETURN BOX** to remove this checkout from your record.  
**TO AVOID FINES** return on or before date due.  
**MAY BE RECALLED** with earlier due date if requested.

DATE DUE	DATE DUE	DATE DUE

**SCANNING TUNNELING MICROSCOPY  
STUDY OF Dy,Gd DISILICIDE NANOSTRUCTURES ON Si (001)**

By

Bangzhi Liu

**A DISSERTATION**

Submitted to  
Michigan State University  
in partial fulfillment of the requirements  
for the degree of

**DOCTOR OF PHILOSOPHY**

Department of Chemical Engineering and Materials Science

2002



## **ABSTRACT**

### **SCANNING TUNNELING MICROSCOPY STUDY OF Dy, Gd DISILICIDE NANOSTRUCTURES ON Si (001)**

By

Bangzhi Liu

The epitaxial growth of rare earth (RE) silicides on the silicon (001) surface has received some recent interest after it was discovered that self-assembled silicide nanowires form in the initial stages of growth. In this dissertation, Dy and Gd are chosen as prototypical systems for the study of RE silicide growth on Si (001) using scanning tunneling microscopy and low energy electron diffraction, with an aim of optimizing nanowire growth.

When depositing Dy and Gd on the Si (001) surface, three types of nanostructures can be formed: 2D reconstructions, nanowires, and 3D islands. The growth behavior of all of these structures is a function of growth temperature, annealing duration, and metal coverage. Two types of 2D reconstructions ( $2\times 4$  and  $2\times 7$ ) are found, and their close relationship is revealed. Dy and Gd disilicide nanowire growth is achieved on both normal Si (001) and vicinal Si (001) substrates. 3D silicide islands which grow in competition with the nanowires can be suppressed by manipulating growth conditions. A relationship between the grown nanostructures and the crystallographic structures of bulk RE disilicides is established.

## ACKNOWLEDGMENTS

I would first like to express my sincere thanks to my advisor, Professor Jun Nogami. I was so lucky to be his first student here at MSU, and have been fortunate to learn the details of running STM from him hand to hand. I know how much time he has spent on me in doing things like taking images, processing data, repairing problems in STM, writing manuscripts and finally finishing this thesis. I have also been deeply impacted by Jun's character qualities and his pleasant personality. He always greets others with a smile and I never saw him getting angry, even when I made mistakes! Without Jun's excellent supervision and huge contribution, it would not have been possible for me to complete this endeavor so successfully nor to graduate so soon.

Thanks also to my labmates Michael Katkov, Chigusa Ohbuchi, and Gangfeng Ye for the help you gave me and for the companionship and fun we had together these last few years. Each of you have truly become a part of my life.

I also want to express my appreciation to Professor Norman Birge for his help with transport measurements and to Professor Martin Crimp for his guidance on TEM experiments. Thanks also to these two professors who, along with Professor Tim Hogan, served on my graduate committee and for all the help you gave me on this thesis.

I would like to give my thanks to my lovely wife, Yi Zhang. She faithfully stood by me during these last four years and especially during this arduous period of thesis writing. I was always deeply moved by her when I still saw her awake waiting for me back home as late as 2:00 am in the morning. Without her love and support, none of this would have been possible.

Special thanks to my friends, Richard and Gretchen Roberts for making me and my wife a part of their family so we could really know them and know what life is like in an America family and for praying for us to successfully complete this difficult time with peace and joy in our hearts.

Finally, I would like to give my thanks to my parents for allowing me to go so “far away” to pursue my dreams. I understand that it is a big sacrifice to them for my not being around them and for their not being able to see their son and his wife for such a long time. I also want to extend my thanks to my sisters and their families, to my wife’s family, and to friends here in the U.S. and back in China for caring about me.

# TABLE OF CONTENTS

<b>LIST OF TABLES .....</b>	<b>vii</b>
<b>LIST OF FIGURES .....</b>	<b>viii</b>
<b>CHAPTER 1 INTRODUCTION .....</b>	<b>1</b>
1.1 BACKGROUND: RE SILICIDE NANOWIRES .....	1
1.2 SILICIDES.....	4
1.2.1 Transition metal silicides .....	4
1.2.2 RE silicides.....	4
1.2.3 Epitaxial growth of RE disilicides .....	10
1.2.3.1 Epitaxial growth on Si (111) .....	11
1.2.3.2 Epitaxial growth on Si (001) .....	13
1.2.4 Resistivity of RE silicides .....	16
1.3 THESIS ORGANIZATION.....	17
<b>CHAPTER 2 EXPERIMENTAL BACKGROUND .....</b>	<b>19</b>
2.1 EXPERIMENTAL METHODS .....	19
2.2 Si (001) SUBSTRATES.....	20
2.3 SCANNING TUNNELING MICROSCOPY AND IMAGE PROCESSING.....	25
2.4 INDEXING OF HEXAGONAL CLOSE-PACKED STRUCTURE.....	27
<b>CHAPTER 3 THE Si (001)(2×4)-Dy SURFACE.....</b>	<b>28</b>
3.1 EXPERIMENTAL OBSERVATIONS .....	28
3.2 DISCUSSION.....	35
3.3 CONCLUSIONS .....	39
<b>CHAPTER 4 Dy SILICIDE NANOWIRE GROWTH ON Si (001).....</b>	<b>40</b>
4.1 EXPERIMENTAL OBSERVATIONS .....	40
4.1.1 Coverage dependence.....	40
4.1.2 Width and height distribution of nanowires .....	43
4.1.3 Nanowire top surface reconstruction.....	45
4.1.4 Nanowire nucleation .....	47
4.1.5 Effect of annealing duration .....	48
4.2 DISCUSSION.....	49
4.3 CONCLUSIONS .....	55
<b>CHAPTER 5 THE Si (001)(2×7)-Gd, Dy SURFACES .....</b>	<b>56</b>
5.1 EXPERIMENTAL OBSERVATIONS .....	56
5.1.1 General observations .....	56
5.1.2 Bias dependence .....	61
5.1.3 Atomic structure .....	63
5.1.4 Coverage dependence.....	65
5.2 DISCUSSION.....	69

5.3 CONCLUSIONS .....	71
<b>CHAPTER 6 A COMPARISON OF Dy AND Gd SILICIDE NANOWIRE GROWTH.....</b>	<b>72</b>
6.1 GROWTH ON NORMAL Si (001) .....	72
6.1.1 General observations.....	72
6.1.2 Gd silicide nanowire growth .....	73
6.1.3 Dy silicide nanowire growth .....	76
6.1.4 3D islands.....	78
6.1.5 Height quantization .....	81
6.1.6 Coverage dependence.....	82
6.1.7 Growth behaviour at 500°C .....	86
6.1.8 Room temperature growth with PDA.....	87
6.1.9 Higher temperature growth .....	89
6.2 GROWTH ON VICINAL Si (001).....	89
6.3 DISCUSSION.....	94
6.3.1 Effects of annealing and growth temperature .....	94
6.3.2 Multiphase coexistence and atomic model.....	94
6.3.3 Lattice mismatch and strain relaxation.....	98
6.4 CONCLUSIONS .....	101
<b>CHAPTER 7 FUTURE WORK.....</b>	<b>102</b>
7.1 EPITAXY .....	102
7.2 LATTICE MISMATCH.....	104
7.3 STRAIN RELAXATION .....	107
7.4 POSSIBLE SYSTEMS TO FORM NANOWIRES .....	108
7.5 FUTURE WORK.....	110
7.5.1 Growth of nanowires with other systems.....	110
7.5.2 Strain relaxation in RE silicide/Si (001) systems.....	112
7.5.3 TEM work .....	113
<b>APPENDIX .....</b>	<b>115</b>
<b>REFERENCES .....</b>	<b>116</b>

## LIST OF TABLES

Table 1.1 Technology roadmap for semiconductors

Table 1.2 Known bulk metal silicides

Table 1.3 Comparison between three classes of transition metal silicides

Table 1.4 RE metals in periodic table

Table 1.5 Space group and stoichiometry of RE disilicides

Table 1.6  $\text{RESi}_2$  lattice parameters and mismatches with Si substrate

Table 1.7 Relationship between rare earth metals and disilicide structures

Table 1.8 Growth conditions, and orientation of appeared phases in  $\text{RESi}_2$  growth on Si (001)

Table 1.9 Resistivity of RE silicides (RT)

Table 4.1 Measured mismatches between the  $c(2 \times 2)$  structure and Si substrate

Table 6.1 Measured amplitude, wavelength and height of wavy islands.

Table 7.1 Lattice matching of some RE disilicides with Si (001)

## LIST OF FIGURES

Figure 1.1 (a) Hexagonal  $\text{AlB}_2$  structure, and (b) tetragonal  $\text{ThSi}_2$  or orthorhombic  $\text{GdSi}_2$  structure.

Figure 1.2 Relationship between (b) hexagonal  $\text{AlB}_2$  structure and (c) tetragonal  $\text{ThSi}_2$ /orthorhombic  $\text{GdSi}_2$  structures, which are built from the same unit block (a).

Figure 1.3 Lattice matching between (a)  $\text{RESi}_2$  (0001) and Si (111), and (b)  $\text{RESi}_2$  ( $\bar{1}100$ ) and Si (001).

Figure 2.1 (a) Diamond structure of silicon, and (b) ideal Si (001) terminated surface.

Figure 2.2 Features observed under (a) filled and (b) empty states STM imaging, and their correspondence with the dimer model. The  $2\times 1$  unit cell is marked by the two rectangular boxes in both images.

Figure 2.3 Schematic drawing of Si: $2\times 1$  reconstruction, as well as  $S_A$  and  $S_B$  types of steps.

Figure 2.4 Filled states image of the two types of steps on Si (001) surface.

Figure 2.5 Empty states image ( $19\text{ nm}\times 19\text{ nm}$ ) of  $4^\circ$  tilted vicinal Si (001) surface.

Figure 2.6 Indices of hcp structure.

Figure 3.1 STM topography of Si (001) surface with 0.5 ML Dy deposited. At a sample bias of +1.39 V, the maximum apparent height of the nanowire is about 0.4 nm, the width is about 5 nm.

Figure 3.2  $2\times 4$  LEED pattern of 0.53 ML Dy on Si (001), grown at  $600^\circ\text{C}$ . The beam energy is 49.2 eV. The Si:  $1\times 1$  spots are indexed. Two  $2\times 4$  reciprocal unit cells are marked by two white boxes which are  $90^\circ$  rotated, reflecting the two domain structure of the Si (001) surface.

Figure 3.3 Large empty states image ( $50\times 50\text{ nm}^2$ ) of the reconstructed surface with 0.5 ML Dy deposited,  $V_T=+1.05\text{ V}$ . The inset is an FFT of this image. The spots in the right half of the FFT pattern are accentuated by the black dots. The Si:  $2\times 1$  reciprocal unit cell is marked by the crosses, and the  $2\times 4$  by the open circles. A close-up of the area enclosed in the square box is shown in Figure 3.4, and that in the rectangular box is shown in Figure 3.5.

Figure 3.4 (a) and (b) are two empty states images of the area enclosed in the square box ( $10\times 10\text{ nm}^2$ ) in Figure 3.3, taken at +1.05 V and +0.46 V, respectively. Clean Si areas (A) and metal reacted areas (B) are marked. Image (a) shows all the maxima in

the metal covered areas have similar height. Image (b) shows two types of maxima, one higher than the other. The broken white boxes in both images show the  $2\times 4$  unit cell. The two small boxes in (b) mark the HLH (type I) and LHL (type II) features.

Figure 3.5 (a)-(c) are three empty states images of the area enclosed in the rectangular box ( $15\times 12\text{ nm}^2$ ) in Figure 3.3, taken at +0.46, +1.05 and +1.85 V, respectively. The heights marked by the black and white arrows along the profiles correspond to the positions marked by the same arrows along the dotted traces.

Figure 3.6 Filled states image ( $15\times 15\text{ nm}^2$ ) of the surface with 0.17 ML deposited,  $V_T=-1.93\text{ V}$ . The surface is separated into areas of clean Si (A) and areas reacted with the metal (B).

Figure 3.7 Registry of the maxima features in the  $2\times 4$  structure with respect to adjacent clean Si dimer positions. A unit cell is marked by a rectangular box.

Figure 3.8 3D model of  $2\times 4$  reconstruction, in which the orientation relationship between nanowires and Si (001) surface is marked. Bonds are added to the Dy atoms for illustration purpose only.

Figure 3.9 Local position of Dy atom in the bulk silicide, which is similar to that on the 2D surface.

Figure 4.1 (a)-(d) are STM images (all  $300\times 300\text{ nm}$ ) which show coverage dependent topography of the Dy/Si (001) surface.

Figure 4.2 3D islands formed at the junction of the nanowires. The image size is  $150\times 150\text{ nm}$ , taken from the same sample surface as Figure 4.1(b). The inset is a height profile of the trace marked by the broken line.

Figure 4.3 Filled states STM image ( $50\times 50\text{ nm}$ ,  $V_T=-1.2\text{ V}$ ) shows that Dy silicide nanowires coexist with  $2\times 4$  and  $2\times 7$  reconstructed Si (001) surface. The nanowires bundle together and form wider structures. A single nanowire can be seen in the lower right corner. The Si dimer row direction is marked in the image.

Figure 4.4 Examples of height and width measurement of the nanowires. The height profiles of traces (1) and (2) in the left-hand side panel are shown in the right-hand side panel, respectively. The image size is  $70\times 70\text{ nm}$ ,  $V_T=+1.04\text{ V}$ .

Figure 4.5 (a) Width distribution of bundled nanowires, and (b) height distribution of additional layers on nanowires.

Figure 4.6 Various reconstructions of the nanowire top surfaces. All the images have the same size,  $10\times 10\text{ nm}$ . Roman numerals in images (b), (d)-(f) correspond to the marked positions in Figure 4.4.



Figure 4.7 Nanowire nucleates (a) on a flat terrace, forming a new step around it by consuming the Si atoms in the neighborhood, and (b) at a step edge, interacting with Si steps on both ends during growth.

Figure 4.8 STM image showing that only a few nanowires survive when continuing to anneal a sample at 600°C for 30 min after deposition of 0.68 ML Dy, mostly large square and elongated islands are formed. The image size is 400×400 nm.

Figure 4.9 (a) Hexagonal AlB<sub>2</sub> type structure of Dy disilicide; (b) lattice matching between the silicide (1  $\bar{1}$  00) plane and Si (001) surface; (c) side view of Dy disilicide growing on Si (001) substrate.

Figure 5.1 STM images (50 nm × 50 nm) showing nanowires coexisting with 2×4 and 2×7 superstructures on a (a) 0.18 ML Dy deposited Si (001) surface,  $V_T = -1.25$  V, and (b) 0.63 ML Gd deposited Si surface,  $V_T = +0.6$  V.

Figure 5.2 (a) STM image (60 nm × 60 nm) showing a 2×7 reconstructed surface with 0.46 ML Gd deposited at 500°C,  $V_T = +1.17$  V. (b) LEED pattern from the sample shown in (a). (c) FFT pattern of image (a). The black box and white box in (b) and (c) denote Si:1×1 and Gd: 2×7 reciprocal unit cells, respectively.

Figure 5.3 Close ups (15 nm × 18 nm) of (a) Gd: 2×7 superstructure,  $V_T = +1.17$  V, and (b) Dy: 2×7 and 2×4 mixtures,  $V_T = +1.24$  V. Image (a) is taken from the same sample as Figure 5.2.

Figure 5.4 STM images (12 nm × 15 nm) showing 2×7 bias dependence in the empty states (a)-(c) and in the filled states (d) and (e). Relative shifts of the maxima in both the subunit rows and the bright strips are marked near the straight lines in (b), (d) and (e).

Figure 5.5 Bias voltage ranges for three different regimes in empty states imaging of the subunits in the Gd:2×7, Dy:2×7 and Dy:2×4 structures. Bias voltages for the individual measurements are shown.

Figure 5.6 Diagram showing the atomic registry of the maxima in the 2×7 superstructure with respect to the Si (001) substrate. The 2×7 unit cell is marked by a black box, and a broken line is drawn to show the anti-phase shift of both the subunit maxima and bright strip maxima.

Figure 5.7 Coverage dependence of 2D and 3D phases appearing for (a) Gd grown on Si at 600°C with post deposition annealing; and Dy on Si at 600°C without (b) and with (c) post deposition annealing.

Figure 5.8 The calculated coverage of the three cases shown in Figure 5.7 is plotted against the nominal coverage.

Figure 5.9 Sum of squared deviation between the actual and calculated coverage plotted versus the assumed number of metal atoms in the  $2 \times 7$  superstructure.

Figure 6.1 Topography of Si (001) surface with 0.4 ML Dy deposited, showing coexistence of nanowires and 3D islands, and second layer growth.

Figure 6.2 (a)-(c) ( $350 \text{ nm} \times 350 \text{ nm}$ ) and (d) ( $300 \text{ nm} \times 300 \text{ nm}$ ) are STM images which show coverage dependent topography of the Gd/Si (001) surface. (e) ( $60 \text{ nm} \times 60 \text{ nm}$ ) is a closer view of the area enclosed in the white box in (b). (f) ( $75 \text{ nm} \times 75 \text{ nm}$ ) is a closer view of the white box in (d).

Figure 6.3 Width distribution of single Gd silicide nanowires in bundle.

Figure 6.4 (a)-(c) are STM images (all  $350 \text{ nm} \times 350 \text{ nm}$ ) showing coverage dependent topography of the Dy/Si (001) surface prepared by PDQ. (d) ( $75 \text{ nm} \times 75 \text{ nm}$ ) is a closer view of the area enclosed in the square box in (b).

Figure 6.5 Topography of (a) 0.6 ML Dy deposited sample prepared by 10 min PDA, image size is  $200 \text{ nm} \times 200 \text{ nm}$ , and (b) the same sample shown in (a) which was annealed another 1 hour, image size is  $350 \text{ nm} \times 350 \text{ nm}$ . The inset in (b) is the height profile of island (1) along the broken line.

Figure 6.6 (a) 3D rendering of wavy island (2) shown in Figure 6.5(b). (b) The height profile of the wavy island along the broken line in (a). (c) Wavy island formed by deposition of 0.92 ML Gd.

Figure 6.7 Coverage dependence of 2D and 3D phases appearing for (a) Gd grown on Si at  $600^\circ\text{C}$  with PDA; and Dy on Si at  $600^\circ\text{C}$  with (b) PDQ and (c) PDA.

Figure 6.8 The calculated coverage of the three cases shown in Figure 6.7 is plotted versus the nominal coverage.

Figure 6.9 STM images ( $180 \text{ nm} \times 180 \text{ nm}$ ) showing coverage dependent topography of the Gd/Si (001) surface grown at  $500^\circ\text{C}$  with (a) 0.46 ML Gd deposited, taken at  $V_T = +0.44 \text{ V}$ ; and (b) 0.54 ML Gd deposited, taken at  $V_T = +1.12 \text{ V}$ . (c) is a high resolution image ( $40 \text{ nm} \times 40 \text{ nm}$ ,  $V_T = -0.67 \text{ V}$ ) of the 2D reconstruction appeared in (b). (d) is an STM image ( $180 \text{ nm} \times 180 \text{ nm}$ ) of the same sample shown in (b) which was annealed at  $600^\circ\text{C}$ , taken at  $V_T = +1.35 \text{ V}$ .

Figure 6.10 (a) and (b) (size:  $60 \text{ nm} \times 70 \text{ nm}$ ), and (c) and (d) (size:  $45 \text{ nm} \times 45 \text{ nm}$ ) are two pairs of dual bias images of a sample prepared by depositing 0.16 ML Dy onto Si at room temperature then annealing at  $600^\circ\text{C}$ .

Figure 6.11 Scanning tunneling microscope (STM) images showing (a) a clean vicinal Si (001) surface with  $4^\circ$  miscut ( $19 \text{ nm} \times 19 \text{ nm}$ ), and (b) the vicinal surface after deposition of Dy at  $600^\circ\text{C}$  with 10 min postannealing ( $300 \text{ nm} \times 300 \text{ nm}$ ).

Figure 6.12 (a) STM image (800 nm×800 nm) showing parallel nanowires formed on a 0.38 ML Dy deposited vicinal Si (001) surface without PDA. A small number of 3D islands still can be seen. After annealing this sample 30 min, the topography is shown in (b) of image size 420 nm×420 nm. 3D islands of various shapes appeared, and only a small number of nanowires survived.

Figure 6.13 STM images showing a parallel nanowire covered surface free of islands formed by depositing 0.77 ML Gd on a vicinal Si (001) substrate (300 nm×300 nm). The sample was prepared with 5 min PDA.

Figure 6.14 Side views of (b) hexagonal and (c) tetragonal RE silicides grown on Si (001) substrate, both of which can be built from the unit block shown in (a).

Figure 7.1 Equilibrium phase diagram in function of the coverage  $\theta$  and misfit  $\epsilon$ . The small panels on the top and the bottom illustrate the morphology of the surface.

Figure 7.2 Lattice matching in heteroepitaxial systems, where  $a_s$  denotes substrate lattice parameter, and  $a_o$  denotes the overlayer lattice parameter. The overlayer lattice is the shaded area.

Figure 7.3 Registry between overlayer and substrate.

Figure 7.4 (a) Bright field image (1 $\mu$ m×0.9 $\mu$ m) of a Dy/Si (001) sample at a metal coverage of 3.4 ML. (b) The diffraction pattern from the same sample.

# **Chapter 1 Introduction**

## **1.1 Background: RE silicide nanowires**

Rare-earth (RE) silicides have been studied since 1979 as a natural extension of the study of transition metal silicides [1], and attracted more attention shortly after Tu et al. found that they have the lowest Schottky barrier height on n-type silicon [2]. In 1986, it was found that the RE disilicides grow epitaxially on Si (111) [3]. Thereafter, most of the work on RE silicide growth has been on Si (111) substrates.

In 1998, Preinesberger et al. found that nanowires can be formed by depositing a small amount of Dy on the Si (001) surface with subsequent high temperature annealing [4]. However, nobody paid attention to this phenomenon until the November 1, 1999, the New York Times reported that Hewlett-Packard (HP) research labs in Palo Alto made a breakthrough in making nanowires on Si surface [5]. Later, Chen et al. [6] from the HP group reported that the formation of the self-assembled erbium disilicide nanowires on Si (001) is due to the anisotropic lattice mismatch between the hexagonal  $\text{AlB}_2$  type structure of the disilicide and Si (001) surface, which can work as a strategy for the intentional epitaxial growth of nanowires for other RE disilicides. Following the NY Times article, we arrived at this conclusion independently and started studying the growth of RE silicides on Si (001) extensively, and found that Ho, Y and Gd disilicides form nanowires, but that other silicides, such as  $\text{NdSi}_2$  only form compact islands, depending on the details of the lattice mismatch between the RE silicides and the Si (001) surface [7-9]. Fairly recently, another RE silicide, scandium disilicide, was also found to form nanowires [10].

As shown in Table 1.1, the minimum feature size achievable with current photolithographic technology is 65 nm, and this minimum is projected to reach 9 nm in 15 years as the scaling down of integrated circuits continues. RE silicide nanowire widths can be as small as 0.8 nm, which is probably beyond the limits of photolithography. Therefore, it would be of technological interest to grow and of scientific interest to understand the properties of these wires at such a small scale. To date, very few data have been published on the RE silicide nanowires [4, 6, 7, 10-12], and their growth behavior and properties are still unclear.

Dysprosium is a prototypical nanowire forming RE metal. Preinesberger et al. published only the barest outlines of the growth behavior in this system in their first paper [4]. In this thesis, the growth of Dy on Si (001) is studied in detail, with different chapters focusing on various aspects such as silicon surface reconstruction, detailed nanowire morphology, growth kinetics, and formation of non-nanowire silicide islands. The primary experimental techniques were scanning tunneling microscopy (STM) and low energy electron diffraction (LEED). In addition, some data on Gd growth is presented and compared with Dy, and some insight into the behavior of both metals is gained by this comparison. The contents of this thesis correspond to four or five papers that have either been published, or are at some stage along the path to publication [13-17]. In the context of the other work on RE silicide nanowires, almost all of which appeared in print after this thesis research was well underway, these studies on Dy and Gd present a significant addition to this literature.

In the remainder of this introductory chapter, the current understanding of RE silicides and RE silicide thin film properties will be reviewed.

Table 1.1 Technology roadmap for semiconductors [18]

Year of	1993	1995	1997	1999	2001	2003	2005	2007	2010	2013	2016
Generation(nm)	500	350	250	180	130	100	80	65	45	32	22
Gate length(nm)	500	350	200	130	65	45	32	25	18	13	9

Table 1.2 Known bulk metal silicides [19-21]

Transition metals												Noble metals
Rare earth	Refractory metals				Near noble metals							
Sc <sub>5</sub> Si <sub>3</sub>	Ti <sub>5</sub> Si <sub>3</sub>	V <sub>3</sub> Si	Cr <sub>3</sub> Si	Mn <sub>3</sub> Si	Fe <sub>3</sub> Si	Co <sub>3</sub> Si	Ni <sub>3</sub> Si	Ni <sub>3</sub> Si <sub>2</sub>	Cu <sub>3</sub> Si			
ScSi	Ti <sub>5</sub> Si <sub>4</sub>	V <sub>5</sub> Si <sub>3</sub>	Cr <sub>5</sub> Si <sub>3</sub>	Mn <sub>5</sub> Si <sub>3</sub>	Fe <sub>5</sub> Si <sub>3</sub>	Co <sub>2</sub> Si	Ni <sub>5</sub> Si <sub>2</sub>	NiSi				
Sc <sub>2</sub> Si <sub>3</sub>	TiSi	VSi <sub>2</sub>	CrSi	MnSi	FeSi	CoSi	Ni <sub>2</sub> Si	NiSi <sub>2</sub>				
Sc <sub>3</sub> Si <sub>5</sub>	TiSi <sub>2</sub>		CrSi <sub>2</sub>	MnSi <sub>2</sub>	FeSi <sub>2</sub>	CoSi <sub>2</sub>						
Y <sub>5</sub> Si <sub>3</sub>	Zr <sub>4</sub> Si	Nb <sub>4</sub> Si	Mo <sub>3</sub> Si		Ru <sub>2</sub> Si	Rh <sub>2</sub> Si	Pd <sub>3</sub> Si					
Y <sub>5</sub> Si <sub>4</sub>	Zr <sub>2</sub> Si	Nb <sub>5</sub> Si <sub>3</sub>	Mo <sub>5</sub> Si <sub>3</sub>		RuSi	Rh <sub>5</sub> Si <sub>3</sub>	Pd <sub>2</sub> Si					
YSi	Zr <sub>5</sub> Si <sub>3</sub>	NbSi	Mo <sub>3</sub> Si <sub>2</sub>		RuSi <sub>2</sub>	Rh <sub>3</sub> Si <sub>2</sub>	PdSi					
Y <sub>3</sub> Si <sub>5</sub>	Zr <sub>3</sub> Si <sub>2</sub>	NbSi <sub>2</sub>	MoSi <sub>2</sub>			Rh <sub>2</sub> Si <sub>3</sub>						
	Zr <sub>4</sub> Si <sub>3</sub>											
La <sub>5</sub> Si <sub>3</sub>	Hf <sub>5</sub> Si <sub>3</sub>	Ta <sub>4.5</sub> Si	W <sub>3</sub> Si	Re <sub>3</sub> Si	OsSi	Ir <sub>3</sub> Si	Pt <sub>3</sub> Si					
La <sub>3</sub> Si <sub>2</sub>	HfSi	Ta <sub>2</sub> Si	W <sub>5</sub> Si <sub>3</sub>	Re <sub>5</sub> Si <sub>3</sub>	OsSi <sub>2</sub>	Ir <sub>2</sub> Si	Pt <sub>2</sub> Si					
LaSi	HfSi <sub>2</sub>	Ta <sub>5</sub> Si <sub>3</sub>	WSi <sub>2</sub>	ReSi	OsSi <sub>3</sub>	IrSi <sub>3</sub>	PtSi					
LaSi <sub>2</sub>	Hf <sub>3</sub> Si <sub>2</sub>	TaSi <sub>2</sub>		ReSi <sub>2</sub>		Ir <sub>3</sub> Si <sub>2</sub>						
Ce <sub>5</sub> Si <sub>3</sub>	Pr <sub>3</sub> Si <sub>2</sub>	Sm <sub>5</sub> Si <sub>3</sub>	EuSi	Gd <sub>5</sub> Si <sub>3</sub>	Tb <sub>5</sub> Si <sub>3</sub>	Dy <sub>5</sub> Si <sub>3</sub>	Ho <sub>5</sub> Si <sub>3</sub>	Er <sub>5</sub> Si <sub>3</sub>	Tm <sub>5</sub> Si <sub>3</sub>	Yb <sub>5</sub> Si <sub>3</sub>	Lu <sub>5</sub> Si <sub>3</sub>	
Ce <sub>2</sub> Si	PrSi	SmSi	EuSi <sub>2</sub>	GdSi	TbSi	DySi	HoSi	ErSi	TmSi	YbSi	LuSi	
Ce <sub>3</sub> Si <sub>2</sub>	PrSi <sub>2</sub>	SmSi <sub>2</sub>		GdSi <sub>1.7</sub>	TbSi <sub>1.7</sub>	DySi <sub>1.7</sub>	HoSi <sub>1.7</sub>	ErSi <sub>1.7</sub>	TmSi <sub>1.7</sub>	YbSi <sub>1.7</sub>	LuSi <sub>1.7</sub>	
CeSi	PrSi <sub>3</sub>			GdSi <sub>2</sub>	TbSi <sub>2</sub>	DySi <sub>2</sub>	HoSi <sub>2</sub>				Lu <sub>2</sub> Si <sub>5</sub>	
CeSi <sub>2</sub>												

## **1.2 Silicides**

### ***1.2.1 Transition metal silicides***

Many elements in the periodic table react with silicon to form different types of compounds. The compounds formed between metals and silicon are called silicides. Of all these, the transition metal silicides are the largest group, of which RE silicides are a subclass, as shown in Table 1.2 [19-21]. The other two subclasses are refractory metal silicides, and near noble metal silicides. The silicides occur in three major stoichiometries: metal rich silicides, in the form of  $M_5Si_3$ ,  $M_5Si_4$ ; monosilicides, in the form of  $MSi$ ; and silicon rich silicides, in the form of  $MSi_2$ ,  $M_3Si_5$ . In much of the published work in these silicides, the compounds are prepared by depositing metal or co-depositing metal and silicon onto Si substrates with high temperature annealing. The final phase formed is the most Si-rich silicide which is frequently the disilicide [19, 22-24]. In addition, most of the silicides used in integrated circuit technology are disilicides, such as  $TiSi_2$ ,  $CoSi_2$ ,  $WSi_2$ ,  $TiSi_2$  and  $FeSi_2$ , etc [19, 22, 25]. Therefore, our interest is narrowed down to the discussion of disilicides.

The RE silicides are classified as a separate class of silicides due to their distinct and interesting physical and chemical properties, amongst them a low temperature of formation, the lowest known Schottky barrier heights on n type Si, good electrical and thermal conductivity, and unusual kinetics of formation [23, 26]. A detailed comparison of the three classes of silicides is listed in Table 1.3.

### ***1.2.2 RE silicides***

Speaking of RE metals, traditionally this category refers to lanthanides inclusively, but now it also tends to include Y and Sc since they have very similar properties [27].





Chemically, the rare earths are classified as members of the IIIB subgroup of the periodic table, as shown in Table 1.4. Based largely on trivalent ionic radii, the RE elements are broadly classified into two groups:

- Light rare earth elements (LREE), or the cerium subgroup, comprise the first seven lanthanides (atomic number 57 through 63);
- Heavy rare earth elements (HREE), or the yttrium subgroup, comprises the remaining lanthanides and yttrium (atomic numbers 64 through 71 and 39).

Yttrium is categorized with the HREE because of its occurrence, ionic radius and other similar properties. Scandium (atomic number 21) occurs widely distributed in nature at low concentrations and is not typically classified as either a LREE or HREE [27].

Table 1.5 Space group and stoichiometry of RE disilicides [21, 26, 33, 34]

<b>structure</b>	<b>Space group</b>	<b>stoichiometry</b>
tetragonal ThSi <sub>2</sub>	I4/amd	RESi <sub>2</sub>
orthorhombic GdSi <sub>2</sub>	Imma	RESi <sub>1.75~1.9</sub>
hexagonal AlB <sub>2</sub>	P6/mmm	RESi <sub>1.67</sub> (Re <sub>3</sub> Si <sub>5</sub> )

Accordingly, the RE disilicides are classified into two groups, light RE silicides and heavy RE silicides. They crystallize in three different structures: tetragonal ThSi<sub>2</sub>, hexagonal AlB<sub>2</sub>, and orthorhombic GdSi<sub>2</sub>. Usually the stoichiometry of the disilicide is written as RESi<sub>2-x</sub> due to the existence of Si vacancies [33, 35]. The tetragonal phase has a composition close to the stoichiometric disilicide (x=0) and the hexagonal phase forms the RE<sub>3</sub>Si<sub>5</sub> stoichiometry (x=0.25), whereas the orthorhombic phase exists for intermediate compositions, as shown in Table 1.5. It is believed that there is one silicon atom out of six is missing in the hexagonal AlB<sub>2</sub> type structure, giving a stoichiometry of  $3/5 \approx 1.67$  or 1.7. Therefore, the disilicides are usually written as RESi<sub>1.7</sub>, RESi<sub>1.67</sub>, or

RESi<sub>2-x</sub> with  $x \approx 0.3$  [1, 36-38]. The notation RE<sub>3</sub>Si<sub>5</sub> is reserved for such compounds as Yb<sub>3</sub>Si<sub>5</sub> with their own structure, not for the defected AlB<sub>2</sub> structure [1].

The three types of structures are closely related. The hexagonal AlB<sub>2</sub> type structure is of the P6/mmm space group; the unit cell is shown in Figure 1.1(a). The tetragonal ThSi<sub>2</sub> type structure is of the I4/amd space group; the unit cell is shown in Figure 1.1(b). The orthorhombic GdSi<sub>2</sub> type structure is of the Imma space group, which is a deformation of the tetragonal ThSi<sub>2</sub> type structure. As shown in Figure 1.2, the three structures can be described as different arrangements of trilayers of the same building element: a parallelepiped with eight silicon atoms as apexes, and a RE atom at the center. These trilayers are stacked along the [001] direction in the tetragonal and orthorhombic structures, and along the  $[10\bar{1}0]$  direction in the hexagonal one. The hexagonal structure also differs from the others by the stacking sequence: successive plates are systematically translated by  $a/2$  in the hexagonal structure, while they are alternatively translated by  $a/2$  or  $b/2$  in the tetragonal and orthorhombic structures. In addition, the largest face of the building element is square in the tetragonal structure, and rectangular in the orthorhombic and hexagonal structures [33]. As a result, the lattice parameters of the tetragonal and hexagonal structures are related,  $a=b \approx (a_{hex}+c_{hex})/2$  and  $c \approx 2 a_{hex} \sqrt{3}$  [39]. Most of the known RE disilicides lattice parameters are listed in Table 1.6.

For bulk disilicides, the type of structure adopted has a dependence on the particular RE metal, as shown in Table 1.7. Although there are discrepancies between different references, a tendency can be seen that the tetragonal and/or orthorhombic structures appear mainly for light RE silicides, the hexagonal structure appears mainly for heavy RE silicides, and a mixture of these structures appears for the RE silicides of medium weight.

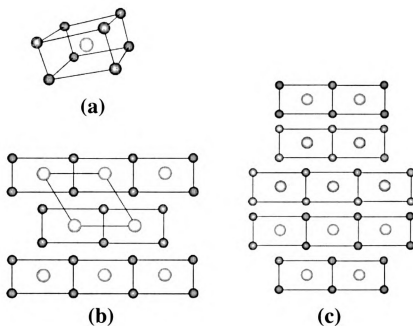
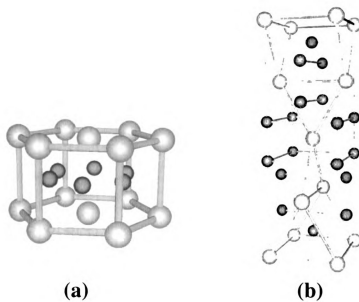


Table 1.5 RESi<sub>2</sub> lattice parameters and mismatches with Si substrate [3, 21, 33, 40]

Silicide	Structure	a (Å)	b (Å)	c (Å)	Area (Å <sup>2</sup> )	Mismatch		
						a (%)	b (%)	c (%)
GdSi <sub>2</sub>	hexagonal AlB <sub>2</sub>	3.877		4.172	16.17	0.96		8.65
	tetragonal ThSi <sub>2</sub>	4.10	4.10	13.61	16.81	6.77	6.77	
	orthorhombic GdSi <sub>2</sub>	4.09	4.01	13.44	16.40	6.51	4.43	
	hexagonal AlB <sub>2</sub>	3.831		4.121	15.79	-0.23		7.32
DySi <sub>2</sub>	tetragonal ThSi <sub>2</sub>	4.03	4.03	13.38	16.24	4.95	4.95	
	orthorhombic GdSi <sub>2</sub>	4.04	3.945	13.34	15.94	5.21	2.73	
	hexagonal AlB <sub>2</sub>	3.816		4.107	15.67	-0.63		6.95
	tetragonal ThSi <sub>2</sub>							
HoSi <sub>2</sub>	orthorhombic GdSi <sub>2</sub>	4.03	3.944	13.30	15.89	4.95	2.71	
	hexagonal AlB <sub>2</sub>	3.798		4.088	15.53	-1.09		6.46
	tetragonal ThSi <sub>2</sub>	3.96	3.96	13.26	15.68	3.13	3.13	
	orthorhombic GdSi <sub>2</sub>							
ScSi <sub>2</sub>	hexagonal AlB <sub>2</sub>	3.664		3.877	14.21	-4.58		0.96
	tetragonal	3.758	3.758	4.761	14.12	-2.13	-2.13	
	Orthorhombic	3.998	9.882	3.659		4.11	-4.71	
	hexagonal AlB <sub>2</sub>	3.839		4.121	15.82	-0.03		7.32
YSi <sub>2</sub>	tetragonal ThSi <sub>2</sub>							
	orthorhombic GdSi <sub>2</sub>	4.056	3.954	13.357	16.04	5.63	2.97	
	hexagonal AlB <sub>2</sub>							
	tetragonal ThSi <sub>2</sub>	4.111	4.111	13.56	16.89	7.06	7.06	
NdSi <sub>2</sub>	orthorhombic GdSi <sub>2</sub>							

Si:  $a_{Si}=3.84$  Å,  $area=14.74$  Å<sup>2</sup>

Table 1.7 Relationship between rare earth metals and disilicide structures

Sc								Y							
T [41]								O/H [33]							
Light rare-earth disilicides								Heavy rare-earth disilicides							
La	Ce	Pr	Nd	Pm	Sm	Eu	Gd	Tb	Dy	Ho	Er	Tm	Yb	Lu	
T/O			O/H					H [33]							
T/O [42]								H/O/T				H			

H: hexagonal, T: Tetragonal, O: Orthorhombic

### 1.2.3 Epitaxial growth of RE disilicides

Silicide films on monocrystalline Si substrates, in general, exhibit a polycrystalline microstructure [22]. But almost all transition-metal silicides can grow epitaxially to a certain extent on silicon under controlled growth conditions [22, 40, 43, 44]. All silicides currently used in device structures are usually polycrystalline due to the difficulty in making epitaxial silicides [45, 46], and that the crystallinity and interface perfection are not of overriding importance in these applications [47]. However, there has been tremendous attention on the growth of epitaxial silicide films out of scientific interest in studying perfect interfaces and technological interest in potential applications in novel devices [22, 45, 48-50]. Also, epitaxial silicide layers have an increasing advantage over polycrystalline silicide layers when junction depths continue to shrink. The good layer uniformity and high thermal stability of epitaxial silicides are very attractive for shallow junction formation. Therefore, the development of reliable and convenient epitaxial silicide technologies is likely to be important for sub 0.1 $\mu$ m devices [45].

It is generally accepted that the reactions between deposited RE metal films and Si substrates are nucleation controlled [24, 26, 51]. For nucleation controlled kinetics, the film nucleates in isolated regions, and then grows rapidly both vertically and laterally,

resulting in a rough, pitted surface [23, 24, 38, 52, 53]. Additionally, nucleation usually occurs over a very limited temperature range (325-400°C for RE silicides grown on Si (111)), below which nothing happens and above which the reactions are too fast to measure [25, 32]. It was also suggested that the contamination layer at the interface is the primary cause of surface pitting [38, 40]. But this seems to be questionable since pinholes can be formed in the RE silicide films grown on a pre-cleaned substrate in UHV (ultra high vacuum) [54-56].

The most common methods used to produce thin epitaxial silicide films on top of silicon are solid phase epitaxy (SPE, i.e., depositing a thin metal layer on an atomically clean substrate at room temperature or elevated temperature under UHV conditions, with or without subsequent annealing at higher temperature) and molecular beam epitaxy (MBE, the metal and silicon are co-deposited onto the silicon substrate under similar conditions as SPE) [36, 39, 40, 43, 57-59]. Other techniques have been developed to improve the surface morphology, such as rapid annealing [3, 60], and intermediate template layers [37, 61, 62]. Sometimes an additional thin layer of Si or metal, such as Pt, W, Mo, etc., is deposited on top of the RE silicide films to keep them from oxidizing [3, 23, 60].

### *1.2.3.1 Epitaxial growth on Si (111)*

As mentioned above, the bulk heavy RE disilicides crystallize in the hexagonal  $AlB_2$  type structure. However, the real situation is more complicated when growing RE disilicide thin films on silicon substrates.

Good-quality epitaxial growth of hexagonal RE silicides is expected on Si (111) substrates since the atoms in the plane normal to  $c$  axis in the silicides are essentially

identical to those on the Si (111) surface, as shown in Figure 1.3(a), resulting in a nearly ideal epitaxial arrangement. Typically, the mismatch is within 1.5%, as shown in Table 1.6. Therefore, major attention has been concentrated on epitaxial growth of RE silicide films on Si (111) surface in the past. It has been found that all of the heavy RE metal disilicides, including  $\text{YSi}_{2-x}$ , can grow epitaxially on Si (111) substrates, and nearly all of them crystallize in the hexagonal  $\text{AlB}_2$  type structure with a unique epitaxial relationship:  $\text{RESi}_{2-x}(0001) // \text{Si}(111)$ ,  $\text{RESi}_{2-x}[\bar{1}2\bar{1}0] // \text{Si}[0\bar{1}1]$  [1, 3, 40, 58, 61-66]. A few references showed that orthorhombic structure could appear for  $\text{GdSi}_{2-x}$  after the hexagonal structure is formed, with a dependence on thickness and annealing temperature [67, 68].

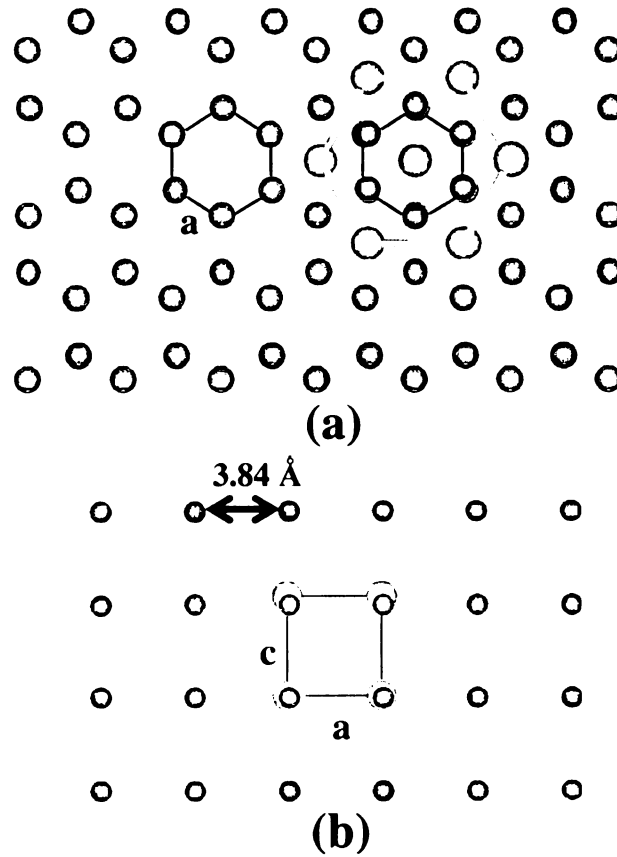


Figure 1.3 Lattice matching between (a)  $\text{RESi}_2(0001)$  and  $\text{Si}(111)$ , and (b)  $\text{RESi}_2(1100)$  and  $\text{Si}(001)$ .

Many techniques, such as LEED, STM and transmission electron microscopy (TEM) etc, have been used in studying the surface reconstruction and vacancy ordering of RE silicides. The hexagonal RE silicides on Si (111) generally show a  $p(1 \times 1)$  reconstruction below 1ML and  $\sqrt{3} \times \sqrt{3}$  reconstruction above 1 ML [54, 55, 63, 69, 70], and this behavior may be temperature dependent [62, 71]. Experiments and theoretical models show that both of the 2D reconstructions result from a buckled Si top layer without vacancies, instead of the graphite-like Si termination expected for a simple truncation of the bulk silicide structure [69, 72-79]. The  $\sqrt{3} \times \sqrt{3}$  periodicity is possibly a reflection of the 3D vacancy ordering superstructure within the film, which has been seen by TEM [63, 64].

### *1.2.3.2 Epitaxial growth on Si (001)*

Compared to Si (111), less research activity has been dedicated to growth on Si (001) since the lattice match between disilicides and Si (001) is not as good as that on Si (111), and the epitaxial relationship is less straightforward. Most of the data on epitaxial growth of continuous RE silicide films on Si (001) are summarized in Table 1.8, which shows that all of the three types of structures, hexagonal  $AlB_2$ , orthorhombic  $GdSi_2$ , and tetragonal  $ThSi_2$ , can grow epitaxially on Si (001), and that the hexagonal phase can coexist with orthorhombic or tetragonal phases, depending on the detailed growth conditions. It is generally observed that there are two types of orientations between the hexagonal structure and Si (001) surface,  $RESi_{2-x}(\bar{1}\bar{1}00) // Si(100)$  with  $RESi_{2-x}[0001] // Si[01\bar{1}]$  and  $RESi_{2-x}(\bar{1}\bar{1}00) // Si(100)$  with  $RESi_{2-x}[0001] // Si[0\bar{1}\bar{1}]$  [39, 64, 80, 81]. These two orientations are normal to each other, and equivalent in volume fraction and



Table 1.8 Growth conditions, and orientation of appeared phases in RESi<sub>2</sub> growth on Si (001)

RESi <sub>2</sub>	Growth conditions		Phase	Orientation relationship
	T <sub>grow</sub> (°C)	T <sub>anneal</sub> (°C) t <sub>anneal</sub> (min)	Thickness (nm)	
Tb/Er/YSi <sub>2</sub>	RT	800/2	30	[0001] <sub>hex</sub> //[01 $\bar{1}$ 1] <sub>Si</sub> , (1100) <sub>hex</sub> //(100), [0001] <sub>hex</sub> //[01 $\bar{1}$ 1], (1000) <sub>hex</sub> //(100) [64]
TmSi <sub>2-x</sub>	450	800/15	66	( $\bar{1}$ 010) <sub>hex</sub> //(100)Si, [0001] <sub>hex</sub> //[01 $\bar{1}$ 1] <sub>Si</sub> [66,6]
ErSi <sub>2-x</sub>	RT	300-900	100	(1100) <sub>hex</sub> //(100)Si, [0001] <sub>hex</sub> //[01 $\bar{1}$ 1] <sub>Si</sub> & [0001] <sub>hex</sub> //[01 $\bar{1}$ 1] <sub>Si</sub> [81]
YSi <sub>2-x</sub>	RT	above 550		(1100) <sub>hex</sub> //(100)Si, [0002] <sub>hex</sub> //[022]; (1100) <sub>hex</sub> //(100), [0002] <sub>hex</sub> //[022] [80]
GdSi <sub>2</sub>	80°C	500/5	5-100	(100)Si//[001] <sub>orth</sub> [82]
GdSi <sub>1.7</sub>	RT	320-650	20-120	amorphous at 320°C [67, 83]
ErSi <sub>2-x</sub>	400-450	800-870/30	40-50	T (100)Si $\equiv$ (001) <sub>terr</sub> , a // [011] <sub>Si</sub> , b // [011] <sub>Si</sub> , c // [100] <sub>Si</sub> [57]
Y/Er/TbSi <sub>1.6</sub>	RT	300-400	200	[11] [68]
GdSi <sub>2-x</sub>	RT	280-600/5	50-1000	H+O
Dy/Si <sub>2-x</sub>	template/co-deposition/450	800/30	60	T (001) <sub>terr</sub> //(100)Si, [010] <sub>terr</sub> //[011] <sub>Si</sub> , [100] <sub>terr</sub> //[011] <sub>Si</sub> [61]
ErSi <sub>1.7</sub>	codeposition/400-450	800-870/30	35-45	(100)Si $\equiv$ ( $\bar{1}$ 010) <sub>hex</sub> , [011] <sub>Si</sub> //[ $\bar{1}$ 010] <sub>hex</sub> , [01 $\bar{1}$ ] <sub>Si</sub> //[0001] <sub>hex</sub> (100)Si $\equiv$ ( $\bar{1}$ 010) <sub>hex</sub> , [011] <sub>Si</sub> //[0001] <sub>hex</sub> , [01 $\bar{1}$ ] <sub>Si</sub> //[ $\bar{1}$ 010] <sub>hex</sub> [39, 84]
ErSi <sub>2-x</sub>	template/RT	450-800/30	58	H ( $\bar{1}$ 010) <sub>hex</sub> //(100), [0001] <sub>Si</sub> //[011] <sub>Si</sub> , [2 $\bar{1}$ 10] <sub>Si</sub> //[01 $\bar{1}$ ] <sub>Si</sub> , [01 $\bar{1}$ ] <sub>Si</sub> //[011] <sub>Si</sub> [85]
	RT+870/ multilayer	800/30		H+T ( $\bar{1}$ 010) <sub>Si</sub> //(100), [0001] <sub>Si</sub> //[01 $\bar{1}$ ] <sub>Si</sub> , [2 $\bar{1}$ 10] <sub>Si</sub> //[011] <sub>Si</sub>
	codeposition/800			T+H (100)Si//[001] <sub>terr</sub> , [010] <sub>terr</sub> //[011] <sub>Si</sub> , [100] <sub>terr</sub> //[01 $\bar{1}$ ] <sub>Si</sub>

H: hexagonal, T: Tetragonal, O: Orthorhombic

crystalline quality [81]. The orthorhombic and tetragonal structures match onto Si (001) surface in the same way,  $\text{RESi}_{2-x} (001)_{\text{tet}} // \text{Si} (001)$  with  $[100]_{\text{tet}} // \text{Si} [01\bar{1}]$ , which is consistent with the close relationship between them. The occurrence of the orthorhombic and tetragonal phases may have a dependence on the species of RE metal. For example, the orthorhombic  $\text{GdSi}_{2-x}$  phase was usually reported [67, 82, 83], but for  $\text{ErSi}_{2-x}$ , tetragonal phase was reported [57, 85].

When we match the hexagonal  $\text{RESi}_2 (\bar{1}100)$  to the Si (100) surface as shown in Figure 1.3(b), anisotropic lattice mismatch results: quite small (0% for  $\text{YSi}_{2-x}$ ) along axis  $a$ , but quite large (8.65% for  $\text{GdSi}_{2-x}$ ) along axis  $c$ , as listed in Table 1.6. This is the proposed mechanism for the RE silicide nanowire formation: the silicides grow without restriction along the small lattice mismatch direction, but with a restriction along the large lattice mismatch direction, resulting in nanowire-like structure [4, 6, 7, 10-12].

Although the growth of RE silicide films on Si (001) has been studied since 1980 [1], the discovery of the RE silicide nanowires had been delayed until fairly recently [4] for two reasons. Firstly, people usually grew continuous thick films (e.g., 5-1000 nm, as listed in Table 1.8), but the nanowires form only at submonolayer coverage (<1 nm); secondly, it is the invention of the STM that made it possible to “see” nanowires at the atomic scale.

Experiments have shown the presence of Si vacancies and 3D vacancy ordering in tetragonal  $\text{ErSi}_{2-x}$  [39, 84] and hexagonal  $\text{RESi}_{2-x}$  (RE=Tb, Er, and Y) (e.g.,  $\sqrt{3} \times \sqrt{3}$  superstructure, same as that within the silicides grown on Si (111) [64]). Several surface reconstructions have been found, such as  $c(2 \times 2)$  on Gd/Si (001) [86], and  $3 \times 1$  and  $3 \times 2$  on Yb/Si (001) [87]. However, many important issues still remain open, such as what

species constitutes the topmost layer and what structure it has, due to the limited publications.

By comparing the behaviors of the epitaxial growth of RE silicides on Si (001) and Si (111), we can see that the substrate orientation affects the growth significantly through the lattice mismatch, which has been realized by some other authors [36, 67, 83, 88]. The epitaxial growth of different phases can also be controlled by using different growth techniques (deposition, codeposition, multilayers, and use of templates), and by controlling the growth conditions. Four factors: growth temperature, annealing temperature, annealing duration, and thickness have been proved to be critical for the epitaxial growth of RE silicides on Si (001), such as the resulting phases and the ratio between coexisting phases [39, 68, 85]. In our experiments, only thermal evaporation of pure metal with subsequent reaction with the substrate is used to form the silicide. The growth temperature, annealing temperature, annealing duration, and metal coverage are varied to study the growth behavior of RE silicide nanowires.

#### ***1.2.4 Resistivity of RE silicides***

The majority of transition metal silicides are metallic [89], and some are semiconducting ( $\text{CrSi}_2$ ,  $\beta\text{-FeSi}_2$ , etc) [90]. The resistivity of the refractory and near noble metal silicides is in the range of  $10^1$  to  $10^2 \mu\Omega \text{ cm}$  at room temperature [89]. Metal silicides have been widely used as ohmic contacts, Schottky barriers, gate electrodes, and interconnects in microelectronic devices [19, 25, 44, 91].

The study of the electrical properties of RE silicides has been less extensive compared to the other silicides. Most of the available data for heavy RE silicides are listed in Table 1.9. As shown in the table, the resistivity of RE silicides is in a similar

range as the other transition metal silicides, but varies with formation conditions and substrate orientations. The RE silicides have potential in applications such as ohmic contacts and infrared detectors because of their low Schottky barrier heights [2, 92]. However, two major problems have delayed their practical application [26]. One is that the RE silicides react with oxygen easily, forming ternary phases with different physicochemical properties. The second problem is the rough morphology of the films formed on Si substrates.

Table 1.9 Resistivity of RE silicides (RT)

Silicide	Resistivity ( $\mu\Omega$ cm)							
	Bulk		Film/Si (001)			Film/Si (111)		
<b>NdSi<sub>2</sub></b>	349	[93]						
<b>GdSi<sub>2</sub></b>	263	[93]	210	O	[34]			
	110	[94]						
<b>DySi<sub>2</sub></b>	3020	[93]	76	T	[61]	114	H	[61]
<b>ErSi<sub>2</sub></b>	59	[94]	264	H	[85]	34	H	[95]
			217	H				
			136	H				
			129	H+T				
<b>ScSi<sub>1.7</sub></b>			38	H	[41]			

### 1.3 Thesis organization

This thesis is organized as follows.

- Chapter 2 is a brief description of experimental methods, as well as a brief introduction to the working mechanism of STM and the structure of the Si (001) clean surface.

- Chapters 3 and 5 describe two dimensional (2D) reconstructions of the Si (001) surface induced by RE metal deposition. These 2D reconstructions co-exist with the 3D silicide structures that grow on the surface and are closely related.
- Chapter 4 summarizes the growth behavior of Dy on Si (001), focusing in detail on nanowire formation, and nanowire morphology.
- Chapter 6 is a comparative study of Dy and Gd silicide growth. Here, Dy growth is studied over a wider range of conditions than in Chapter 4, and the differences in behavior of the two metals are examined. This chapter also includes data on a particular variant of nanowire growth: growth of parallel arrays of Dy and Gd nanowires on single-domain, vicinal Si (001) surfaces.
- Chapter 7 is a summary of potential future research directions.

## Chapter 2 Experimental Background

In this chapter, the experimental methods used, the basic properties of the Si (001) substrate, and the basic mechanism of STM are introduced. The indexing of the Si (001) surface and the hexagonal structure are also given since both are used repeatedly in subsequent chapters.

### 2.1 Experimental methods

All experiments were performed in a UHV chamber with a base pressure of  $2 \times 10^{-10}$  Torr. The chamber was equipped with a commercial STM (Omicron, GmbH, Taunusstein, Germany), low energy electron diffraction (LEED) optics, and metal deposition facilities. Clean Si (001)  $2 \times 1$  surfaces were prepared by flashing above  $1150^\circ\text{C}$  for 30 s, quickly cooling to  $980^\circ\text{C}$  and holding for 10 min, then slowly turning down the heating current. The clean surfaces were monitored by both LEED and STM. Gadolinium and dysprosium were evaporated from tungsten filaments. Deposition rates were measured with a quartz crystal monitor. Typical deposition rates were 0.1 monolayers (ML) per minute. The nominal coverage was determined by timed exposure to the source. The samples were kept at elevated temperature during deposition, and then annealed for several minutes after deposition before cooling down to room temperature. Four different growth temperatures,  $500^\circ\text{C}$ ,  $600^\circ\text{C}$ ,  $650^\circ\text{C}$ , and  $700^\circ\text{C}$ , were used in experiments. Three methods were primarily used to prepare RE disilicide films:

- depositing RE metal onto a heated Si (001) substrate, mostly at  $600^\circ\text{C}$  with 2 to 10 min post deposition annealing

- the same deposition conditions as above, but cutting off the heating current immediately after deposition
- annealing a sample at 600°C after it has been cooled down to room temperature

The metal coverage (0.1 – 3.5 ML) was varied under each condition. All STM and LEED observations were at room temperature. The tunneling voltages are specified as sample bias, with the STM tip held at virtual ground.

## 2.2 Si (001) substrates

Bulk silicon has a diamond structure of the space group  $Fd\bar{3}m$ , as shown in Figure 2.1(a), with a lattice parameter  $a_{bulk} = 0.543$  nm. An ideally terminated Si (001) surface is shown in Figure 2.1(b), which is a square 2D lattice with a lattice parameter of  $a_{Si} = a_{bulk} / \sqrt{2} = 0.384$  nm. A  $1 \times 1$  unit cell is defined in the figure, with two basic vectors running in  $[1\bar{1}0]$  and  $[110]$ , and one Si atom in the unit cell.

Generally the unit of a monolayer (ML) is used to measure the coverage of overlayer atoms on a single crystal substrate. One monolayer is defined as an areal density equal to the number of atoms per unit area in a single atomic layer of the substrate material parallel to the surface. In the absence of reconstruction, this is the same as the number density of atoms in the top atomic layer of the substrate [96]. According to this definition, for Si (001) is  $1 \text{ ML} = 1/a_{Si}^2 = 1/(0.384^2 \text{ nm}^2) = 6.78 \times 10^{14} \text{ atoms/cm}^2$ .

As shown in Figure 2.1, each Si atom is bonded with four Si atoms in the bulk structure. However, on the Si (001) surface, each of the first layer atoms is bonded with two atoms in the second layer, leaving two dangling bonds on each surface atom. Since this configuration is not energetically favorable, the surface reconstructs to lower the

surface energy. The most common reconstruction observed is  $2\times 1$ , in which two neighboring surface atoms are bonded together to form a Si dimer, which reduces the number of dangling bonds from two per atom to one per atom. The reconstruction establishes two characteristic directions on the surface: either along or perpendicular to the surface dimer rows, in orthogonal  $\langle 110 \rangle$  directions, which will be called the dimer row direction and the dimerization direction, respectively. In this thesis, the Si dimer row direction is defined as  $[1\bar{1}0]$  and the Si dimerization direction as  $[110]$ , as already indicated in Figure 2.1(b).

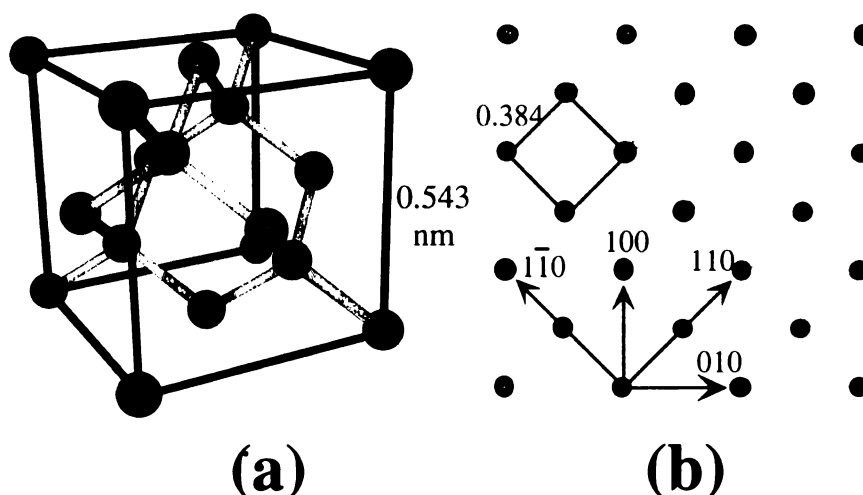


Figure 2.1 (a) Diamond structure of silicon, and (b) ideal Si (001) terminated surface.

Theories [97-99] show that the electronic structure of these dimers consists of an occupied  $\pi$  state below the Fermi energy  $E_F$  and an unoccupied  $\pi^*$  state above  $E_F$ . During STM imaging, the spatial distribution of these  $\pi$ -bonding and  $\pi^*$ -antibonding states are probed by electrons tunneling out of and into the surface, giving the filled and empty states images, respectively. The filled states image emphasize the filled dimer bond lying



between the two atoms, and the empty states image shows the dangling bonds at the end of each dimer pair. As a result, each Si dimer appears as a bean-shaped feature at negative sample bias, as shown in Figure 2.2(a), but as two well-distinguished small features at positive sample bias as shown in Figure 2.2(b), respectively.

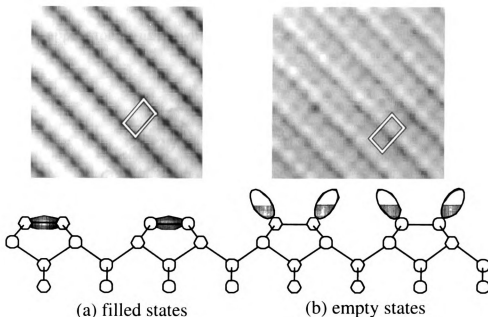


Figure 2.2 Features observed under (a) filled and (b) empty states STM imaging, and their correspondence with the dimer model. The  $2\times 1$  unit cell is marked by the two rectangular boxes in both images.

In reality, the Si (001):  $2\times 1$  surface is stressed since atoms in a dimer are closer than they are in the bulk. There is a tensile stress in the dimer bond direction, while along the dimer row direction, the stress is compressive (or at least less tensile) [99, 100]. The  $2\times 1$  structure is shown schematically in Figure 2.3, in which a  $2\times 1$  unit cell is marked. Because of the stress anisotropy, the surface is expected to break up into two degenerate stress domains with single-atomic-steps as their boundaries, with a step height of  $a_{\text{bulk}}/4=0.136$  nm. The dimer rows rotate  $90^\circ$  from one terrace domain to the next owing

to the tetrahedral coordination of diamond structure of silicon. Thus, two types of monoatomic steps coexist. Following the notations of Chadi [101], the  $S_A$  step is parallel to the upper-terrace dimer rows and the  $S_B$  step is perpendicular to the upper-terrace dimer rows. The energy required to form kinks in an  $S_A$  step is higher than that in an  $S_B$  step, hence at experimentally accessible temperatures,  $S_A$  steps typically appear smooth, while  $S_B$  steps appear rough, as shown in Figure 2.4.

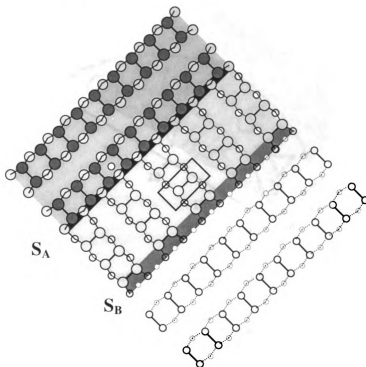


Figure 2.3 Schematic drawing of  $Si(2 \times 1)$  reconstruction, as well as  $S_A$  and  $S_B$  types of steps.

When the vicinal angle is high, double-atomic-layer high steps are favored on a Si (001) surface. One can again define purely from geometrical considerations two different types of double steps,  $D_A$  and  $D_B$ , which are parallel and perpendicular to the upper-terrace dimer rows, respectively. But in reality, because the  $D_A$  steps are much higher in energy, a Si (001) surface with a large vicinal angle contains only  $D_B$  steps. Figure 2.5 is

an STM image of a  $4^\circ$  tilted vicinal surface with  $D_B$  steps. Here, about 95% of the surface is single domain, with the Si dimer rows running from lower left to upper right. A few small areas of the alternative domain are seen where the double height  $D_B$  step has split into a pair of single height steps.

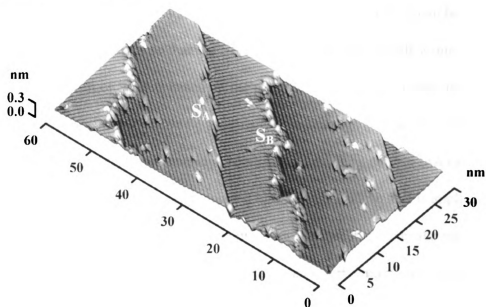


Figure 2.4 Filled states image of the two types of steps on Si (001) surface.

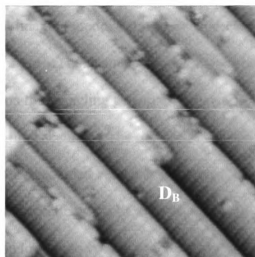


Figure 2.5 Empty states image (19 nm×19 nm) of  $4^\circ$  tilted vicinal Si (001) surface.

### 2.3 Scanning tunneling microscopy and image processing

Scanning tunneling microscopy (STM) has become a very powerful technique for the determination of the structural and electronic properties of surfaces over the last twenty years [96, 102-104]. The STM is primarily used as a high resolution imaging tool, by which a lateral resolution of 0.1 Å and a vertical resolution of 0.01 Å can be achieved. This is sufficient resolution so that the STM can actually “see” single atoms on a surface.

The mechanism of STM is based on the phenomenon of quantum mechanical tunneling. When a sharp metallic tip is brought close enough ( $\sim 5$  to  $10$  Å) to a conducting surface, electron tunneling occurs and a tunneling current (nA range) can be detected between the tip and sample when a bias voltage (mV to 5V) is applied. To obtain an image, the tip is scanned in the two lateral dimensions over the surface driven by piezoelectric elements. The STM can be operated in several imaging modes, such as constant current and constant height imaging modes. All of the STM images included in this dissertation are taken in the constant current mode, which is introduced briefly as follows.

In the constant current imaging mode, a computer-controlled feedback loop adjusts the tip height to maintain a pre-set constant current. Since the tunneling current is exponentially dependent on the tunneling gap, constant current implies constant tip to sample distance to a very high accuracy. The tip motion, as measured by the voltage applied to the z-piezo, is then recorded versus the scan position. Essentially, the corrugation in the STM image reflects the local density of states integrated over a range of energies between the tip to sample voltage and the Fermi level, at the position of the tip apex. For surfaces which have relatively uniform electronic properties, such as metals,

the STM image effectively represents the surface topography. For electronic inhomogeneous surfaces, such as semiconductors, the electronic structure becomes important in determining the nature of the image.

Generally, the STM image of semiconductors shows a very strong bias dependence, reflecting the spatial distribution of the valence and conduction band structure. A typical example is the pair of filled and empty states images of the Si (001):  $2\times 1$  reconstructed surface shown in Figure 2.2.

The most common method of displaying STM data is to construct a grayscale image, where the brightness is keyed to height. Bright features in the image represent higher features on the surface. In virtually all of the images in this thesis, only minimal image processing has been done, consisting of planar background subtraction and contrast adjustment in order to make full use of the grayscale for any given image. In some instances, a lateral linear mapping has been applied to the image to correct for the effects of thermal drift during the acquisition time of the image (typically 1 - 20 minutes).

In a few instances, additional processing has been done to emphasize small corrugations on atomic terraces at different heights. This is certainly true of all of the pseudo-3D rendered images, for example Figure 2.4. When this type of contrast enhancement is applied to 2D images, it is noted in the text.

Most of the image processing was done with Image SXM, which is a front end for NIH Image written by Steve Barrett at the University of Liverpool specifically for scanned probe images of all kinds [105]

## 2.4 Indexing of hexagonal close-packed structure

Due to the repeated usage of indices of hexagonal close-packed (hcp) structure, a fully indexed bulk structure is shown in Figure 2.6 following the four-index notation, in which the indices of any direction can be written as  $[u \ v \ t \ w]$ , where  $t = -(u+v)$ , and the indices of any plane can be written as  $(h \ k \ l \ i)$ , where  $i = -(h+k)$ .

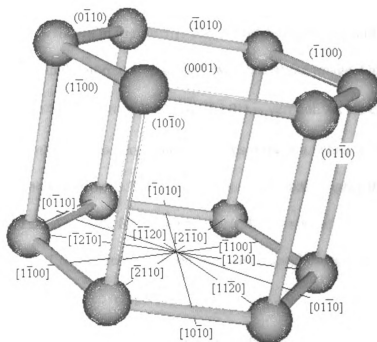


Figure 2.6 Indices of hcp structure.

## Chapter 3 The Si (001)(2×4)-Dy surface

In this chapter, the 2×4 reconstruction induced by submonolayer deposition of Dy on Si (001) is introduced.

### 3.1 Experimental observations

Deposition of Dy on Si (001) at 600°C leads to the formation of nanowires on a reconstructed surface, as shown in Figure 3.1. The 3D rendering shows a ridged nanowire in the upper part and a single-atomic-step in the lower part of the image. On the upper terrace in this image the Si dimer row direction ( $[1\bar{1}0]$ ) is vertical. As we can see, the long dimension of the nanowire is perpendicular to this direction, which is the general trend observed for nanowire growth. The nanowire is significantly higher than the single-atomic-step height (1.36 Å). Aside from the nanowire, the remainder of the surface is covered by both bare 2×1 reconstructed silicon and metal reconstructed areas, with the details depending on the metal coverage.

Generally, a 2×4 LEED pattern was observed over the coverage range 0.17- 1.6 ML, and it is sharpest around 0.5 ML, as shown in Figure 3.2. Figure 3.3 shows a 50 nm square empty states image of a surface with 0.5 ML Dy deposited. A single-atomic-step runs horizontally through the image. Each terrace has areas of bare Si as well as reconstructed areas that we associate with the Dy. The reconstructed patches show a stronger corrugation, and trenches separated by three rows of maxima. The inset is an FFT of this image that shows a 2×4 superstructure that agrees with the LEED pattern of this exact sample.

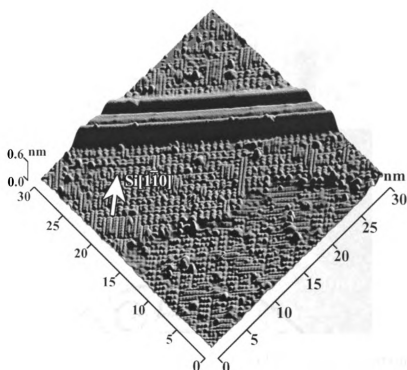


Figure 3.1 STM topography of Si (001) surface with 0.5 ML Dy deposited. At a sample bias of +1.39 V, the maximum apparent height of the nanowire is about 0.4 nm, the width is about 5 nm.

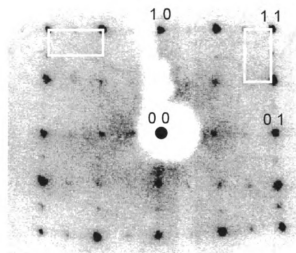


Figure 3.2  $2\times 4$  LEED pattern of 0.53 ML Dy on Si (001), grown at  $600^\circ\text{C}$ . The beam energy is 49.2 eV. The Si:  $1\times 1$  spots are indexed. Two  $2\times 4$  reciprocal unit cells are marked by two white boxes which are  $90^\circ$  rotated, reflecting the two domain structure of the Si (001) surface.



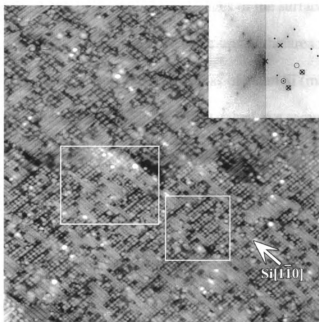


Figure 3.3 Large empty states image ( $50 \times 50 \text{ nm}^2$ ) of the reconstructed surface with 0.5 ML Dy deposited,  $V_f = +1.05 \text{ V}$ . The inset is an FFT of this image. The spots in the right half of the FFT pattern are accentuated by the black dots. The Si:  $2 \times 1$  reciprocal unit cell is marked by the crosses, and the  $2 \times 4$  by the open circles. A close-up of the area enclosed in the square box is shown in Figure 3.4, and that in the rectangular box is shown in Figure 3.5.

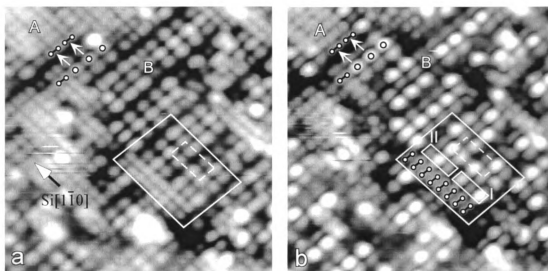


Figure 3.4 (a) and (b) are two empty states images of the area enclosed in the square box ( $10 \times 10 \text{ nm}^2$ ) in Figure 3.3, taken at  $+1.05 \text{ V}$  and  $+0.46 \text{ V}$ , respectively. Clean Si areas (A) and metal reacted areas (B) are marked. Image (a) shows all the maxima in the metal covered areas have similar height. Image (b) shows two types of maxima, one higher than the other. The broken white boxes in both images show the  $2 \times 4$  unit cell. The two small boxes in (b) mark the HLH (type I) and LHL (type II) features.

Figures 3.4(a) and (b) are two empty states images of the surface shown in Figure 3.3, taken at two different biases. Both images are close-ups of the area marked by the square box in Figure 3.3. The surface is separated into areas of clean Si (marked A) and areas reacted with the metal (marked B). In Figure 3.4(a), taken at a sample bias of +1.05 V, all the maxima in the metal covered areas have similar heights. In Figure 3.4(b), at +0.46 V, however, two types of maxima can be seen, with one much higher than the other. These maxima are in registry with the positions of Si dimers in both directions, along and perpendicular to the Si dimer rows. If we use H to denote the high maxima and L to denote the low maxima in (b), two arrangements along the Si dimer row direction can be differentiated, HLH (type I feature) and LHL (type II feature). These two types of features alternate along the Si dimer rows, and there is usually a Si dimer vacancy in between. In a few cases, the two features are adjacent directly to each other. Along the perpendicular direction, no obvious alternation between type I and type II was observed. Statistics show that the probability of having a like neighbor in the Si dimerization direction is much higher than that of having a different neighbor.

Figure 3.5(a)-(c) shows three empty states images over the area marked by the rectangular box in Figure 3.3, taken at different biases. Once again, significant differences in maxima height in the metal covered areas can be seen, implying that the maxima heights are strongly bias-dependent in the empty states. The detailed appearance of the metal covered areas varies as well. Observing the arrangement of three rows of maxima in the white box in these three images, the middle row is higher in (a), all three rows are at similar heights in (b), and the middle row is almost invisible in (c). Therefore, we can draw a conclusion here that not all maxima are visible at +1.85 V (c), but these

missing maxima show up again with stronger intensity at +0.46 V (a), and with similar intensity at +1.05 V (b). The bias-dependence of maxima height can also be observed from the height profiles along the same trace marked by dotted lines in these three images. The black and white arrows in the images show the correspondence between the specific maxima and their heights.

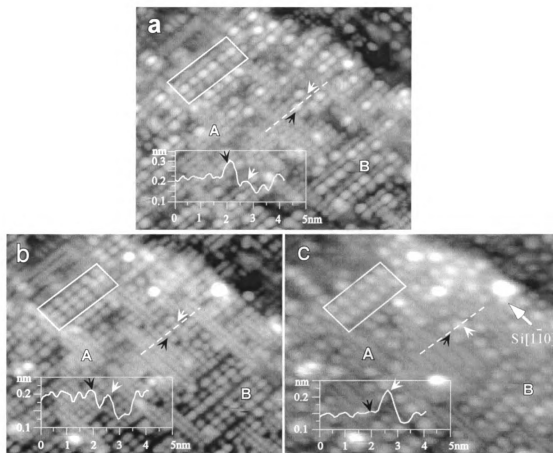


Figure 3.5 (a)-(c) are three empty states images of the area enclosed in the rectangular box ( $15 \times 12 \text{ nm}^2$ ) in Figure 3.3, taken at +0.46, +1.05 and +1.85 V, respectively. The heights marked by the black and white arrows along the profiles correspond to the positions marked by the same arrows along the dotted traces.

As mentioned above, type I and type II features alternate along the Si dimer rows. If this alternation were strict, the long range periodicity would be  $2 \times 8$ . However, the real

order is  $2\times 4$ , as seen by LEED and also the FFT of our STM data. We ascribe this ordering to the basic  $2\times 4$  building block which can be either type I or type II.

Figure 3.6 is a filled states image of a surface with 0.17 ML Dy. Areas of clean Si and reacted Si are marked by A and B, respectively. Overall, the reacted areas appear lower than the Si dimers. The  $2\times 4$  ordering is not as clear as in the empty states images. This is due to a variation in the heights and sizes of maxima in the reacted areas. A one-for-one correspondence can be found between maxima in the filled and the empty states, but not all maxima that appeared in the empty states are visible in the filled states. It is clear from Figure 3.6 that the filled states maxima line up with Si dimers in the same row.

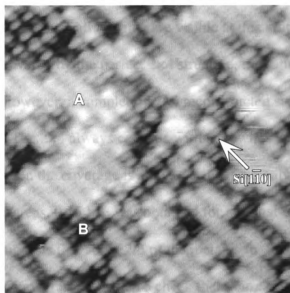


Figure 3.6 Filled states image ( $15\times 15\text{ nm}^2$ ) of the surface with 0.17 ML deposited,  $V_T = -1.93\text{ V}$ . The surface is separated into areas of clean Si (A) and areas reacted with the metal (B).

In many metal induced reconstructions of Si surfaces, it is possible to evaluate the number of metal atoms per unit area by measuring the fraction of reconstructed surface

and comparing it to the metal coverage. However, it is very difficult to do the same thing in this particular case since a significant fraction of the metal can be drawn into the silicide nanowires. Comparing images of surfaces at 0.17 ML (Figure 3.6) and 0.5 ML (Figure 3.4(a)), it is true that more of the surface is reconstructed at higher metal coverage, but this increase is not in direct proportion to the change in coverage. Since we observe three maxima within each  $2\times 4$  unit cell, the simplest possible assumption is to associate each maximum with one metal atom. It is certainly possible that the metal atoms might be below the top layer and that the observed maxima are in fact Si atoms, but in the absence of other information, we make this assumption for the purpose of estimating metal coverage. Usually, images taken at around +1 V are chosen for the coverage counting because all maxima are visible at this voltage. Under this assumption, if the surface is covered by the perfect  $2\times 4$  structure, the saturation coverage would be  $3/8=0.375$  ML. However, a completely  $2\times 4$  reconstructed surface was never observed in our experiments. The  $2\times 4$  always coexists with nanowires and with clean Si which do not disappear even when the coverage is above 3 ML. If we only count metal atoms on the 2D reconstructed areas, 0.15 ML was obtained for nominal coverage 0.5 ML, and 0.2 ML for 1 ML. This suggests that about  $2/3$  of the metal is in the nanowires at 0.5 ML and about  $4/5$  in the nanowires at 1 ML. To check the accuracy of this statement, we estimated the amount of metal corresponding to the measured volume of silicide nanowires. There is an additional 0.35 ML at 0.5 ML nominal coverage, and 0.6 ML at 1 ML. Therefore, all of the metal can be accounted for within experimental error (about 20%) if we combine the 2D surface and the 3D nanowires together. It is also possible that

some of the metal atoms diffuse into the bulk which would slightly reduce the amount of metal in the nanowires.

Note that one other possible assumption is that only the high or the low maxima in the reconstructed areas are metal atoms. Under either assumption, the density of maxima on the terraces combined with the metal density associated with the nanowires is not sufficient to account for the deposited metal, and so both the high and low maxima in the  $2\times 4$  structure are likely to be associated with metal atoms.

### **3.2 Discussion**

The relative heights of maxima and surrounding Si dimers shown in Figures 3.4-6 suggest that they are in the same layer, i.e., the Si dimers in the reacted areas were removed and the maxima sit on the next lower layer. As discussed above, the maxima are centered over the Si dimer rows and also in line with Si dimers, which implies that the maxima are exactly in the place of the missing dimers. Figure 3.7 is a model which shows the positions of the maxima in the  $2\times 4$  structure with respect to the surrounding Si dimers. The alternation between the two types of features (HLH and LHL) along the dimer rows, the Si dimer vacancies between different features, and the statistical character along the Si dimerization direction are also shown in this figure. A 3D model is shown in Figure 3.8 (note that the difference between H and L maxima are not shown here).

The presence of the two types of maxima (H and L) could be explained by a buckling of the Dy atoms based on the previous work done on Si (111) [3, 55, 63, 75, 106]. It is

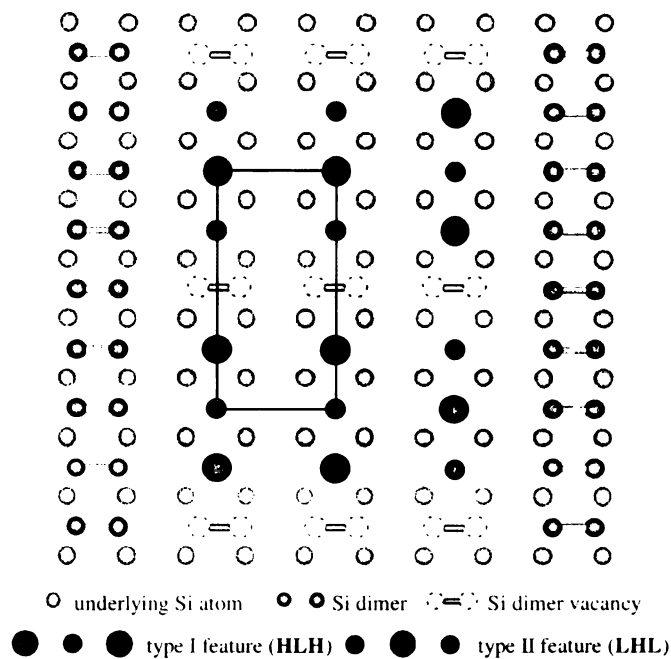


Figure 3.7 Registry of the maxima features in the  $2\times 4$  structure with respect to adjacent clean Si dimer positions. A unit cell is marked by a rectangular box.

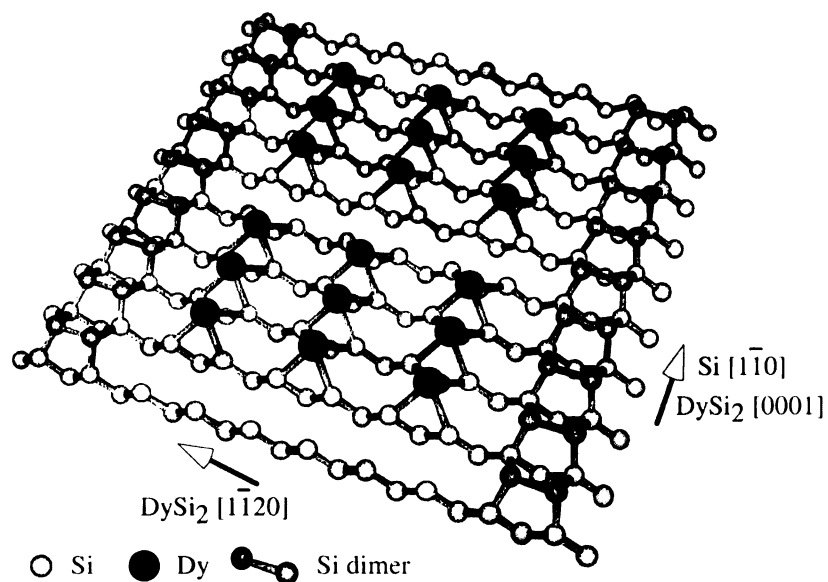


Figure 3.8 3D model of  $2\times 4$  reconstruction, in which the orientation relationship between nanowires and Si (001) surface is marked. Bonds are added to the Dy atoms for illustration purpose only.

known that the RE disilicides grown on Si (111) are a defected  $A1B_2$  structure, which includes about 15-20% Si vacancies [3]. The vacancies are believed to play a role in strain relaxation. Ordered arrangement of these vacancies has been observed in the bulk silicide [3, 75] and also in silicide films on Si (1 1 1) [55, 75]. These vacancies induce shifts in the Si and metal positions within the silicide [106] and in the surface [75]. The buckling will mimic this behavior, where the metal atoms shifting up and down cause the high and low maxima, as well as the alternation between the two features, HLH and LHL. The bias-dependence of the maxima in empty states could come from the buckling as well, which would lead to a change in the electronic charge distribution on the surface, and in turn, might affect the appearance of the maxima at different biases.

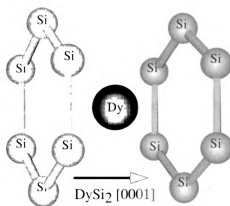


Figure 3.9 Local position of Dy atom in the bulk silicide, which is similar to that on the 2D surface.

If the assumption that each maximum in the empty states corresponds to one Dy atom is correct, then the local environment of the Dy atom on the surface, as shown in Figure 3.8, is similar to that in the bulk silicide, as shown in Figure 3.9. Comparing Figure 3.8 and Figure 3.9, the  $c$  axis of the silicide can be visualized as lying along the Si dimer row



direction. Therefore, the reconstructed 2D surface can be considered as the first step to forming the silicide, with  $\text{DySi}_2(01\bar{1}0)//\text{Si}(001)$  and  $[0001]$  parallel to the dimer row direction ( $\text{Si}[1\bar{1}0]$ ). Referring back to Figure 3.1, the long dimension of the nanowire would be along  $[11\bar{2}0]$  (direction of axis  $a$ ).

For  $\text{DySi}_2$ , the lattice parameter  $a$  is 0.3831 nm, which matches the Si surface periodicity  $a_{\text{Si}}$  (=0.384 nm) very well, but  $c$  is 0.4121 nm, which has a significant mismatch with  $a_{\text{Si}}$  [3]. So strain will develop along what would be the  $c$  axis of the silicide, which is parallel to the Si dimer row direction as observed from the nanowires. Therefore, the Si dimer vacancies along the Si dimer rows in the  $2\times 4$  surface would relieve the strain. Likewise, the growth of the silicide islands (nanowires) in the  $[0001]$  direction (the Si dimer row direction) will be limited due to the strain developed, but they will grow without limitation in the direction of  $[11\bar{2}0]$  due to the small mismatch. This is consistent with the observed orientation of the silicide nanowire, as shown in Figure 3.1.

It is entirely possible that the maxima seen in the STM images are due to rearranged Si atoms, with Dy atoms having moved below the topmost layer of atoms. We cannot rule this out on the basis of the STM data, and an appropriate model cannot be proposed for such a structure at this moment. However, the analogies between the  $2\times 4$  surface and the bulk silicide structure in regard to strain accommodation by buckling and Si dimer vacancies hold true regardless of the details of the surface structure.

### 3.3 Conclusions

When Dy is deposited on Si (001) at 600°C, highly elongated islands of Dy silicide are formed, and the surrounding substrate is reconstructed into a 2×4 periodicity. STM measurements show that the appearance of the 2×4 surface is bias-dependent. An atomic model is proposed where a Dy atom replaces a Si dimer on the top layer, sitting in an atomic position that is almost the same as that in the bulk silicide. Groups of three Dy atoms and a Si dimer vacancy form the 2×4 unit cell. The bias-dependence of the STM images is explained in terms of a buckling of the Dy atoms. Both the buckling and the presence of Si dimer vacancies contribute to strain relaxation along the Si dimer row direction.

## Chapter 4 Dy silicide nanowire growth on Si (001)

In this chapter, the growth behavior of Dy on Si (001) is described in detail, including nanowire and non-nanowire island formation, surface reconstructions of the nanowires and the substrates, nanowire nucleation, and interactions between nanowires and Si steps during growth.

### 4.1 Experimental observations

#### 4.1.1 Coverage dependence

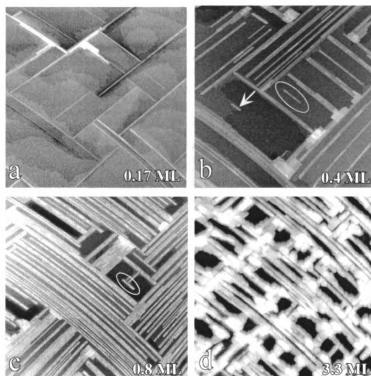


Figure 4.1 (a)-(d) are STM images (all 300×300 nm) which show coverage dependent topography of the Dy/Si (001) surface.

Figures 4.1(a-d) show a sequence of STM images at metal coverages up to 3.3 ML. At this image magnification, only the overall surface morphology is visible. All samples

in Figure 4.1 were prepared at a growth temperature of 600°C with 2-10 minutes of post-annealing. At the lowest coverage (0.17 ML) only very narrow nanowires are formed. These nanowires run in two perpendicular  $\langle 1\bar{1}0 \rangle$  directions and form a network structure, reflecting the two domain structure of the substrate surface. Single height atomic steps are visible on the uncovered areas of substrate. As coverage increases in (b) and (c), the nanowires become denser and wider, and some rectangular islands are formed, mostly at the junctions of the nanowires, as shown in Figure 4.2, which was taken from the same sample surface as Figure 4.1(b) with a higher resolution. At 3.3 ML in (d), a network structure is formed with significant formation of irregular 3D islands.

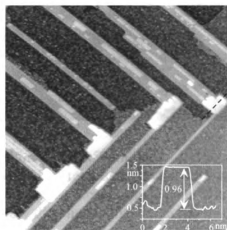


Figure 4.2 3D islands formed at the junction of the nanowires. The image size is 150×150nm, taken from the same sample surface as Figure 4.1(b). The inset is a height profile of the trace marked by the broken line.

Figure 4.3 shows a close up of a surface with a narrow and wide nanowire at 0.53 ML. Here it is clear that what was described as a wider nanowire in Figure 4.1 is actually a bundle of parallel nanowires separated by narrow trenches. Some second layer silicide growth is seen as well, exhibiting a layer-by-layer growth mode, where each second layer

island does not cross the trenches in the first layer. We make a distinction between this type of second layer growth which we interpret as a continuation of nanowire growth, and the growth of larger and wider islands seen at nanowire junctions.

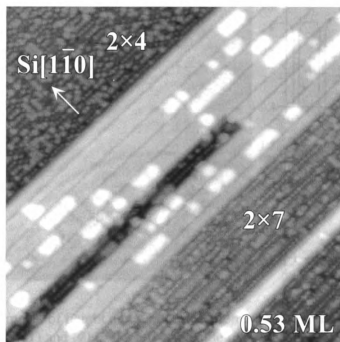


Figure 4.3 Filled states STM image ( $50 \times 50 \text{ nm}$ ,  $V_T = -1.2 \text{ V}$ ) shows that Dy silicide nanowires coexist with  $2 \times 4$  and  $2 \times 7$  reconstructed Si (001) surface. The nanowires bundle together and form wider structures. A single nanowire can be seen in the lower right corner. The Si dimer row direction is marked in the image.

Two different surface reconstructions,  $2 \times 4$  and  $2 \times 7$ , are visible in the areas of the substrate adjacent to the nanowires in Figure 4.3. The Si dimer row direction of the substrate surface is marked, which is perpendicular to the nanowires on the same terrace. Furthermore, the  $2 \times$  dimensions of the  $2 \times 4$  and  $2 \times 7$  superstructures run parallel to the nanowires, or perpendicular to the Si dimer row direction. The details of the  $2 \times 4$  reconstruction have been presented chapter 3, and the  $2 \times 7$  reconstruction will be described in chapter 5. Generally, both the  $2 \times 4$  and  $2 \times 7$  reconstructions could appear

separately or simultaneously with the nanowires, with a dependence on the detailed growth conditions. Unreconstructed Si patches usually coexist with the  $2\times 4$  reconstructed areas, as discussed in the previous chapter, but not with the  $2\times 7$  reconstructed areas.

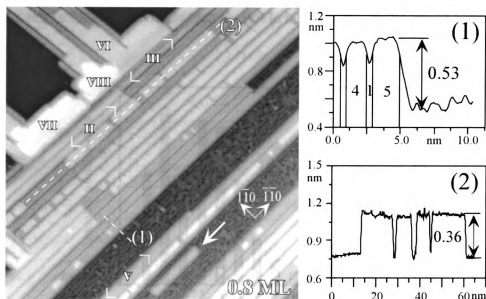


Figure 4.4 Examples of height and width measurement of the nanowires. The height profiles of traces (1) and (2) in the left-hand side panel are shown in the right-hand side panel, respectively. The image size is  $70\times 70$  nm,  $V_T=+1.04$  V.

#### 4.1.2 Width and height distribution of nanowires

By comparing the width of the nanowires to the periodicity measured from Si dimer rows or  $2\times 4/2\times 7$  superstructures in the same image, it was found that the width is quantized in multiples of the Si surface lattice parameter  $a_{Si}$  ( $=0.384$  nm). One example of the width measurement is shown in the right-hand side panel of Figure 4.4, where the curve 1 is the height profile of trace (1) in the left-hand side panel. Along this trace, the last two nanowires are  $4a_{Si}$  and  $5a_{Si}$  wide, respectively, and the trench between them is  $1a_{Si}$  wide. Note that the width measurement was calibrated by the periodicity measured within the same image. Figure 4.5(a) shows the width distribution of the bundled

nanowires measured from many images at different metal coverages. The minimum width is  $2a_{Si}$  (0.77nm), and the maximum  $16a_{Si}$  (6.14nm). Mostly, the nanowire widths are between  $2-7a_{Si}$ . All of the trenches between adjacent nanowires are measured to be  $1a_{Si}$  wide. For isolated nanowires which are not in bundles, the widths range between  $2-4a_{Si}$ .

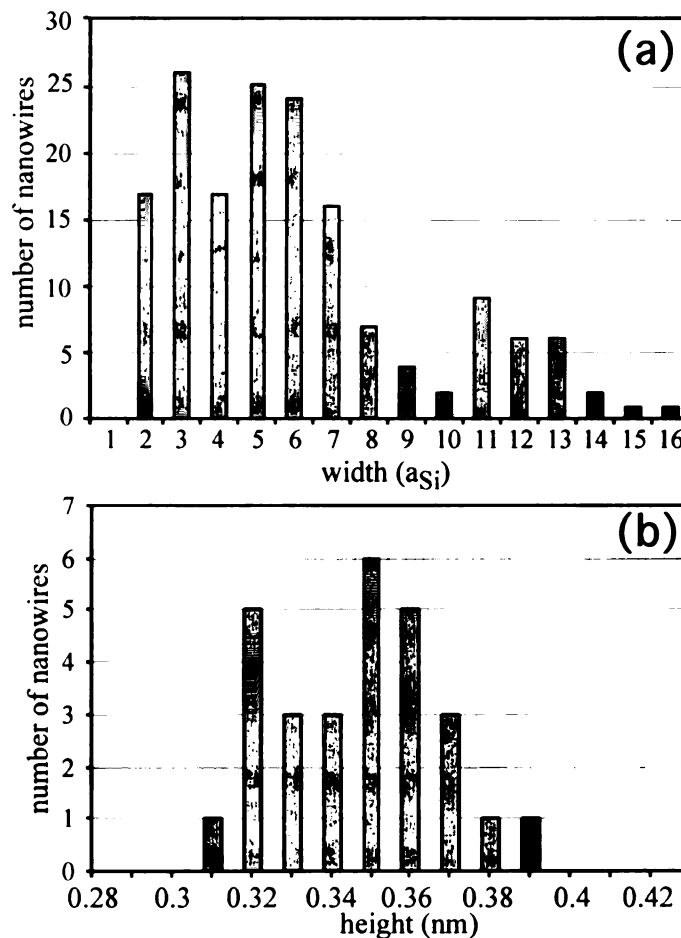


Figure 4.5 (a) Width distribution of bundled nanowires, and (b) height distribution of additional layers on nanowires.

Without considering any additional layers, the minimum nanowire heights measured with respect to the surrounding Si surface range between 0.48 nm and 0.56 nm, which varying slightly with bias in both filled and empty states. One example of this measurement is shown in Figure 4.4. The nanowire height along trace (1) in the left panel

is 0.53 nm, as indicated in profile (1) in the right-hand side panel. These measured values could be different from the geometrical heights since the reconstructed Si surface and nanowire surface have different electronic states, resulting in different apparent heights. To avoid this difficulty, heights of the islands growing atop nanowires were measured with respect to the surface of the nanowires underneath since we believe that they have the same surface. The height difference distribution of nanowires is shown in Figure 4.5(b), in which all the measured heights range from 0.31 nm to 0.39 nm with an average of  $0.34 \pm 0.02$  nm. One example of the height measurement is shown by profile (2) in the right-hand side panel of Figure 4.4, showing that the height of the islands along trace (2) in the left-hand side panel is 0.36 nm.

#### ***4.1.3 Nanowire top surface reconstruction***

The nanowire top surfaces exhibit various superstructures, which may depend on the nanowire width. Figure 4.6 shows a collection of high resolution images of nanowire top surfaces, most of which were taken from Figure 4.4 (a) except nanowire I and IV. In Figure 4.6(a) the reconstruction of nanowire I turns from  $p(1 \times 1)$  in the narrow part into a different superstructure when the width changes from  $2 a_{Si}$  to  $4 a_{Si}$ . In (b), nanowire II of width  $2 a_{Si}$  has maxima on the top which are spaced  $2 a_{Si}$  apart along the nanowire long dimension. Maxima of  $1 a_{Si}$  apart are also possible, as seen on nanowire III of the same width, but less common. Nanowires IV and V with width of  $5 a_{Si}$  in (c) have other complicated superstructures with holes in the center, with a periodicity of  $2 a_{Si}$  along the nanowire for V but larger for IV. We did not observe the well-ordered  $2 \times 1$  nanowire reconstruction recently reported by Preinesberger et al.[12].



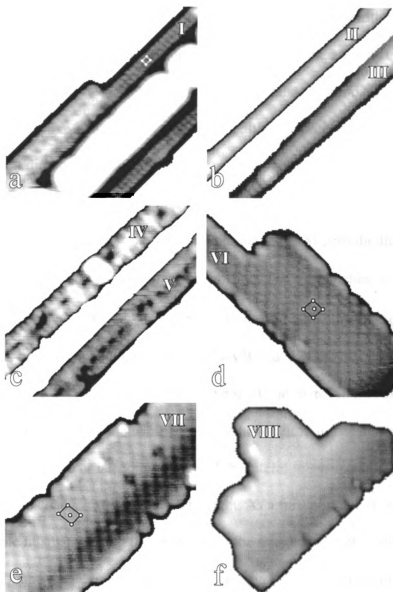


Figure 4.6 Various reconstructions of the nanowire top surfaces. All the images have the same size, 10×10 nm. Roman numerals in images (b), (d)-(f) correspond to the marked positions in Figure 4.4.

Table 4.1 Measured mismatches between the c(2×2) structure and Si substrate

island #	Longitudinal mismatch (%)	Lateral mismatch (%)
VI	0.8	7.6
VII	2.1	10.3
VIII	2.7	10.4

The most common superstructure is  $c(2 \times 2)$  when the nanowire width is larger than  $4a_{Si}$ , as shown in (d). The reconstructed surface is atomically flat, and one unit cell is marked in the image. Figures 4.6(e) and (f) show that islands VII and VIII have the same surface reconstruction as nanowire VI underneath, although both surfaces are curved across their short dimensions. The  $c(2 \times 2)$  unit cell in Figures 4.6(d) and (e) is not square if observed closely. The maxima spacings ( $x$ ) along the longitudinal and lateral directions of the nanowires are compared with the measured Si periodicities along both directions to correct for any possible image distortion. The mismatches,  $(x - a_{Si})/a_{Si}$  expressed as percentages are listed in Table 4.1. Referring to the image shown in Figure 4.4, island VI is one height quantum, and islands VII and VIII are two height quanta, respectively, above the surface of the minimum height nanowires in this image, with each quantum being three layers of atoms. In all cases, the longitudinal mismatch along the long axis of the nanowire or island is small, and the lateral mismatch is large. The apparent mismatch changes as a function of height. As a further point of reference, there is no measurable mismatch along the long axis of the minimum height nanowires (i.e. the level below VI), and the lateral mismatch is not measurable since the reconstructions of these wires are complex and varied.

#### ***4.1.4 Nanowire nucleation***

Short nanowires are often observed at a step edge, or on a flat terrace, as marked by the arrows in Figure 4.1(b) and Figure 4.4, respectively. This suggests that the nanowire could nucleate at a step edge or on a flat terrace. In the first case, as the nanowire grows, the Si atoms around it will be consumed to construct the nanowire, causing new steps to form, as shown in Figure 4.7(a). In the second case, the nanowire takes Si atoms directly

from Si step edges, causing Si steps to bunch up at the end of the nanowire and forming a “snow-plow” effect, as noted by Chen et al.[6, 11]. A typical example is shown in Figure 4.7(b). Due to the consumption of Si atoms from the step edges, the steps retract and form a channel in the upper terraces at the lower right end, and produce a quantity of run-steps and form a significant “snow-plow” effect in the lower terraces during growth. The nanowire can affect the terraces significantly below and above the terrace on which it grows, but always grows on a single flat terrace, never crosses a step.

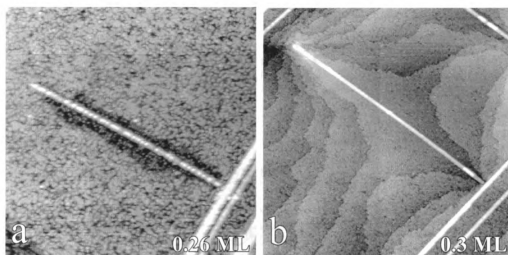


Figure 4.7 Nanowire nucleates (a) on a flat terrace, forming a new step around it by consuming the Si atoms in the neighborhood, and (b) at a step edge, interacting with Si steps on both ends during growth.

#### ***4.1.5 Effect of annealing duration***

All the samples discussed above were prepared by depositing Dy onto Si (001) at 600°C with post-annealing less than 10 min. When Dy deposition is followed by a long period of post-annealing, larger, more three dimensional (3D) silicide islands are formed. Figure 4.8 shows a surface with 0.68 ML Dy annealed for 30 minutes at the deposition temperature of 600°C. The metal coverage is between those shown in Figures 4.2(b) and

(c), and yet the topography is very different with almost no nanowires present. This makes it clear that for Dy in this general coverage range, the morphology of the silicide formed is a function of both metal coverage and annealing time, and that the nanowires are a metastable phase and consumed by the post-annealing process. Islands 1 and 2 are about 8 nm wide and 300 nm long, and islands 3 and 4 are about 25 nm wide. It is hard to measure the heights of these islands since they are situated in trenches. But our measurements still showed that all of the islands 1-4 have a minimum height of 0.97 nm with respect to the bottom of the surrounding trenches.

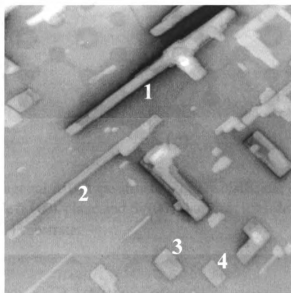


Figure 4.8 STM image showing that only a few nanowires survive when continuing to anneal a sample at 600°C for 30 min after deposition of 0.68 ML Dy, mostly large square and elongated islands are formed. The image size is 400×400 nm.

## 4.2 Discussion

The nanowire formation has been explained by anisotropic lattice mismatch between hexagonal RE disilicides and Si (001) surface [6, 7], which can be described with an atomic model shown in Figure 4.9. The hexagonal  $\text{AlB}_2$  type structure is shown in (a). If

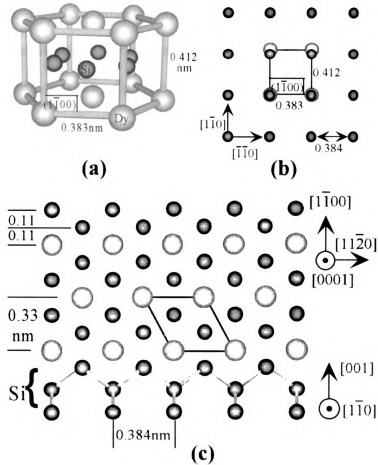


Figure 4.9 (a) Hexagonal  $\text{AlB}_2$  type structure of Dy disilicide; (b) lattice matching between the silicide  $(1\bar{1}00)$  plane and Si  $(001)$  surface; (c) side view of Dy disilicide growing on Si  $(001)$  substrate.

we match the  $(1\bar{1}00)$  onto the Si  $(100)$  surface lattice as shown in (b), for certain RE silicides,  $a$  is well matched to the silicon substrate, but  $c$  is not. For example, for  $\text{DySi}_2$ ,  $a=0.383 \text{ nm}$  and  $c=0.421 \text{ nm}$  which correspond to mismatches of  $-0.36\%$  and  $7.3\%$ , respectively[3]. Figure 4.9(c) shows the side view of the hexagonal  $\text{DySi}_2$  on Si  $(001)$  surface lattice seen from the  $[0001]$  direction. Here we make an assumption that the first layer of Dy atoms are located in the center of the Si  $(1\times 1)$  unit cells, which reserve the same positions as that of the  $2\times 4$  reconstructed Dy atoms, as suggested in the previous

chapter. If we continue to assume that the Dy atoms are 0.11 nm above the Si (001) plane underneath so that these Dy atoms in the interface have almost the same environment as they are in the bulk, providing a perfect epitaxial condition for the silicide to grow. Essentially, this model is the same as the one proposed by Chen et al. [6, 11]. The wire grows to an arbitrary length in the direction of small mismatch (horizontally in the plane of the page) and is limited in its ability to grow coherently with the substrate in the lateral direction (perpendicular to the page).

The quantized height of 0.34 nm can be explained by the model shown in Figure 4.9(c). As seen from the side view, the silicide is comprised of one layer of metal atoms and one bilayer of Si atoms alternatively along the vertical direction. The spacing between each layer is 0.11 nm, and the height of one unit cell is 0.33 nm. The average height of islands on nanowires (0.34 nm) is very close to this number, which suggests that the layer height on top of the nanowires is just one silicide unit cell high.

The orientation relationship between hexagonal structure and Si (001) substrate shown in Figure 4.9 is consistent with that observed during RE silicide film growth, i.e., the hexagonal phase grows on Si (001) surface in two orientations,  $\text{RESi}_{2-x}(\bar{1}\bar{1}00) // \text{Si}(001)$  with  $\text{RESi}_{2-x}[0001] // \text{Si}[1\bar{1}0]$ , and  $\text{RESi}_{2-x}(\bar{1}\bar{1}00) // \text{Si}(100)$  with  $\text{RESi}_{2-x}[0001] // \text{Si}[\bar{1}\bar{1}0]$  [39, 64, 80, 81], which are normal to each other, and equivalent in volume fraction and crystalline quality due to the four-fold symmetry of the Si (001) substrate. Our STM data add more details to this statement. On a single  $2 \times 1$  reconstructed Si (001) terrace, the nanowires run only in one specific direction, the long dimension  $[1\bar{1}20]$  perpendicular to the Si dimer row direction  $[1\bar{1}0]$ , as seen in Figures 4.4 & 4.5. The presence of the two perpendicular orientations of the hexagonal phases is caused by the

fact that the Si dimer rows run in perpendicular directions on adjacent terraces. Although the Si (001) substrate has four-fold symmetry, a single terrace only has two-fold symmetry regulated by the  $2\times 1$  reconstruction. The preferred orientation could result from the chemical bonding between silicide and Si substrate, as discussed in references [6, 11].

It has been determined that the hexagonal RE disilicides grown on Si (111) terminate with a buckled Si bilayer instead of the graphite-like Si termination expected for a simple truncation of the bulk silicide structure [69, 72]. The RE silicides on Si (111) generally show  $p(1\times 1)$  reconstruction below 1 ML and  $\sqrt{3}\times\sqrt{3}$  reconstruction above 1 ML [54, 55, 63, 69, 70]. Both of the 2D reconstructions result from a buckled Si top layer without vacancies, but the  $\sqrt{3}\times\sqrt{3}$  periodicity is a modulation of the  $p(1\times 1)$  periodicity caused by the 3D vacancy ordering superstructure within the film [69, 72-78]. The same issue, however, still remains open for the RE silicides on Si (001) since no experimental data and theoretical simulation have been done on this system. As shown in Figure 4.9(c), the nanowires could be terminated by either by a Si atomic layer or a metal atomic layer. Compared to Si (111), it would be natural to believe that the top layer of the RE silicides on Si (001) has a Si bilayer as a termination since it is exactly like the Si (001) termination of bulk silicon, as in reference [12] which suggests that a  $2\times 1$  surface seen on nanowires is terminated with Si dimers. The  $p(1\times 1)$  reconstruction shown in Figure 4.6(a) would also be a proof for this statement. It would not be hard to construct a model for the  $c(2\times 2)$  superstructure by removing some Si atoms from the top layer, similar to that proposed for the  $c(2\times 2)$  superstructure seen on larger Er silicide islands grown on Si (001) [107]. It is also possible that these superstructures result from the 3D vacancy

ordering within the nanowire, as discussed above for Si (111). The existence of the 3D vacancy ordering has been observed for RE silicide films on Si (001) by TEM[64]. However, the holes appearing in the top layer of nanowire V, as shown in Figure 4.6(c), could result from the Si vacancies in the surface, different from the vacancy free top surface of RE silicides on Si (111).

It is well established that strain relaxation plays a very important role in heteroepitaxial growth due to the mismatch between dissimilar materials[108-110]. For large lattice mismatch systems ( $>2\%$ ), three dimensional island growth is favored over the layer-by-layer growth mode[111, 112]. Theoretical simulation shows that the early stages of binary epilayer growth on a solid surface may self-assemble into ordered parallel stripes with identical width in nanoscale due to anisotropic surface stress [113, 114]. The bundled nanowires may resemble this behavior, but the width distributes in a wide range. No ordering can be derived from the distribution of single nanowires, probably resulting from the random nucleation of the nanowires.

As discussed above, the Si atoms move from Si step edges or adjacent areas on the same terrace to form the nanowires, which is consistent with the fact that the Si atoms are the dominant diffusive species during the RE silicide growth on Si (111) [23, 115]. In the second case, new steps will be formed and make the surface rough. But the nanowires always grow on a flat terrace and never cross a step, whose growth could be stopped by another perpendicular nanowire, or at step edges, as seen in Figures 4.2, 3, and 8. Figure 4.7(b) is a typical example of a nanowire that is stopped by one nanowire on one end and at Si step edges on the other end. The nanowire could also stop in the middle of a terrace due to shortage of metal atoms, as seen in Figures 4.2(b) and (c), where the only short



nanowires that do not terminate at either a step or an intersecting nanowire are those (circled) that are entirely framed by other nanowires. In this situation, the nanowire must compete with the surroundings for metal atoms.

As seen in Figure 4.8, some 3D islands can be fairly elongated. However, we still call them ‘islands’ since their widths lie well outside the range of width distribution defined for ‘nanowires’ in Figure 4.4(a), and also, they have similar minimum height as that of compact islands shown in Figures 4.3 and 4.9, much higher than that of the nanowires. One example of the height measurement is shown in Figure 4.2 that the island marked by the broken line is 0.96 nm, as indicated by the height profile in the inset.

The formation of the nanowires has been explained by the hexagonal  $\text{AlB}_2$  type structure in this chapter and other references [6, 7, 11], and the restricted width is related to the poor mismatch along  $c$  direction [7]. Evidently, we are going to encounter difficulties to explain these compact and elongated islands with the same structure. Considering the fact that the hexagonal phase usually coexists with orthorhombic or tetragonal phase in the RE silicide films on Si (001), and their mismatches with the silicon substrate are not nearly as anisotropic as for the hexagonal phase, it is natural to propose that these rectangular and square shaped islands have orthorhombic or tetragonal structure. This is consistent with the TEM observation that only the tetragonal phase is seen in thicker films that were annealed for 30 minutes [61]. Similar 3D Er silicide islands on Si (001) have also been assigned to the tetragonal phase [107], which are definitely different from the Er disilicide nanowires discussed by Chen et al. [6, 11].

How do these 3D islands compare with the rectangular islands at the nanowire junctions seen in Figure 4.4? Close examination shows that the islands in Figure 4.4 have

geometries that are still defined or restricted by the underlying or adjacent nanowire structure. In this respect, these islands are considered as upper layers of nanowire layer by layer growth. It is possible that the highest of these small islands are right at the transition between nanowire and 3D island growth. Close examination of the nanowires, islands at nanowire junctions, and the large 3D islands with high resolution diffraction techniques will be necessary to understand the different crystal structures. However, at this point in time, all that we can conclude is that true nanowires (corresponding to the hexagonal silicide) have widths less than 6 nm and minimum height 0.5 nm, whereas 3D islands have a minimum width of 8 nm, and a larger minimum height.

#### **4.3 Conclusions**

When Dy is deposited onto Si (001) surface at 600°C, a network of nanowires is formed, and the width and density of the nanowires strongly depend on the deposited coverage. These nanowires grow only on a flat terrace, running perpendicular to the Si dimer rows. The nanowires coexist with a 2×4 and/or 2×7 reconstructed Si surface. The top surface of the nanowires are reconstructed into p(1×1), c(2×2), and other superstructures. 3D islands appear with increasing coverages and longer annealing duration, which could have orthorhombic or tetragonal structure, different from the hexagonal structure of the nanowires. The nanowire width is quantized in terms of  $a_{Si}$ , with a range from  $2a_{Si}$  to  $16a_{Si}$ . The nanowires grow layer-by-layer with a quantized step height of one unit cell of the hexagonal AlB<sub>2</sub> type structure.

## Chapter 5 The Si (001)(2×7)-Gd, Dy surfaces

As discussed in Chapter 3 and 4, deposition of Dy onto Si (001) leads to the formation of a 2D reconstructed Si surface, nanowires and 3D islands. Growth of Gd on Si (001) shows very similar behavior. For example, both metals can induce 2×4 and 2×7 reconstructions of the Si (001) substrate. In this chapter, a detailed study of these 2D phases is presented. The structure of the 2×7 phase will be discussed in terms of what is known about the 2×4. The similarities and differences between the reconstructions induced by the two different metals will also be discussed.

### 5.1 Experimental observations

#### 5.1.1 General observations

Deposition of RE metals (Dy, Gd in this study) leads to the formation of RE disilicide nanowires on a reconstructed surface, which can be a 2×4 or 2×7 superstructure, or a mixture of both. This latter case is shown in Figure 5.1(a) for Dy and (b) for Gd, respectively. Morphological similarities can be seen for Dy and Gd with nanowires or nanowire bundles coexisting with the reconstructed substrate.

Figure 5.2(a) is an empty states image of an area that is covered entirely with the 2×7 phase. Figure 5.2(b) is a low energy electron diffraction (LEED) pattern of the sample shown in (a). The 7× periodicity is clearly discernable from the pattern. Streaks appear at the half order positions, caused by anti-phase disorder[116]. Figure 5.2(c) is the fast Fourier transform (FFT) of image (a), which matches with the LEED pattern very well. The 2×7 reciprocal unit cell is marked by a white box, and the Si: 1×1 reciprocal unit cell is marked by a black square box in both (b) and (c).

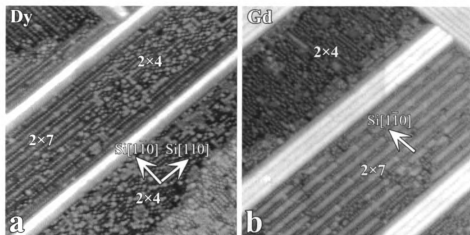


Figure 5.1 STM images ( $50 \text{ nm} \times 50 \text{ nm}$ ) showing nanowires coexisting with  $2 \times 4$  and  $2 \times 7$  superstructures on a (a) 0.18 ML Dy deposited Si (001) surface,  $V_T = -1.25 \text{ V}$ , and (b) 0.63 ML Gd deposited Si surface,  $V_T = +0.6 \text{ V}$ .

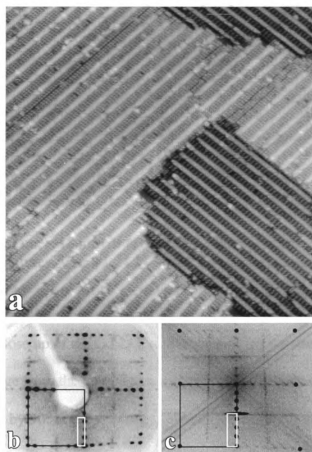


Figure 5.2 (a) STM image ( $60 \text{ nm} \times 60 \text{ nm}$ ) showing a  $2 \times 7$  reconstructed surface with 0.46 ML Gd deposited at  $500^\circ\text{C}$ ,  $V_T = +1.17 \text{ V}$ . (b) LEED pattern from the sample shown in (a). (c) FFT pattern of image (a). The black box and white box in (b) and (c) denote Si:  $1 \times 1$  and Gd:  $2 \times 7$  reciprocal unit cells, respectively.

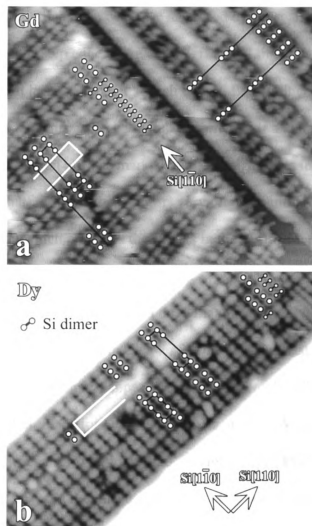


Figure 5.3 Close ups ( $15 \text{ nm} \times 18 \text{ nm}$ ) of (a) Gd:  $2 \times 7$  superstructure,  $V_T = +1.17 \text{ V}$ , and (b) Dy:  $2 \times 7$  and  $2 \times 4$  mixtures,  $V_T = +1.24 \text{ V}$ . Image (a) is taken from the same sample as Figure 5.2.

Figure 5.3(a) is a close up of the Gd:  $2 \times 7$  superstructure, with a single-atomic-step running across the image from the upper left corner to the lower right corner. Although all the structure rotates by  $90^\circ$  at the step edge, we will denote the Si dimer row direction on any given terrace as  $[1\bar{1}0]$ , and the Si dimerization direction as  $[110]$ . At this particular sample bias of  $+1.17 \text{ V}$  (empty states), the  $2 \times 7$  superstructure appears as rows of three maxima divided by a bright strip. A  $2 \times 7$  unit cell is marked by a black box in the

image, and the  $2 \times 7$  periodicity can be easily measured by comparison to the bare Si dimers marked along the step edge. If we define groups of three maxima as a subunit, then each  $2 \times 7$  unit cell has one subunit at each corner. Each unit cell also crosses one of the bright strips. The subunits could be in line or shifted half a unit cell with respect to the adjacent subunits along  $[110]$ , as marked by the straight lines in the lower and upper terraces in (a). This half unit cell shift appears very often, resulting in antiphase disorder along the  $2 \times$  direction which produces the streaks in the 2D diffraction pattern seen in Figure 5.2 (b) and (c).

The  $2 \times 4$  unit cell is also composed of a three maxima subunit plus a “missing Si dimer” at similar bias, as discussed in Chapter 3. One can ask what the relationship is between the three maxima subunits appearing in both  $2 \times 4$  and  $2 \times 7$  superstructures. Figure 5.3(b) is an STM image for Dy taken at a bias of +1.24 V, showing that the same three maxima subunits can form both  $2 \times 4$  and  $2 \times 7$  local superstructures, whose unit cells are marked by black boxes in the image. The bright strip between two rows of subunits combines them to form a row of  $2 \times 7$  unit cells. Comparing the marked bright strips with the maxima along the same row and with adjacent maxima rows in Figure 5.3(a) and (b), it can be seen that the bright strip is two maxima wide, and has a trench one Si dimer wide separating it from the adjacent three maxima subunits on both sides. Therefore, the three maxima subunits have the same geometry for both  $2 \times 4$  and  $2 \times 7$  superstructures. Also, it can be seen that all of the maxima within each subunit in (a) and (b) share the same position as a Si dimer by comparing them to the bare Si dimers as marked.

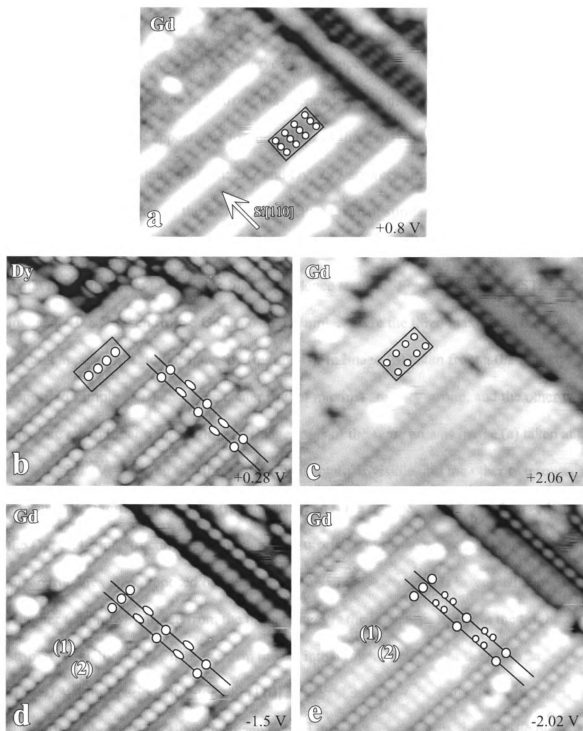


Figure 5.4 STM images ( $12 \text{ nm} \times 15 \text{ nm}$ ) showing  $2 \times 7$  bias dependence in the empty states (a)-(c) and in the filled states (d) and (e). Relative shifts of the maxima in both the subunit rows and the bright strips are marked near the straight lines in (b), (d) and (e).

### 5.1.2 Bias dependence

Significant differences can be observed in the appearance of the  $2\times 7$  superstructure shown in Figures 5.1-3 due to a strong bias dependence in the empty states. Generally, three distinct types of appearance for the groups of three maxima can be differentiated. Since the bias dependences of Gd:  $2\times 7$  and Dy:  $2\times 7$  are very similar, as evidenced by the fact that the appearance of the  $2\times 7$  superstructure taken at similar bias shown in Figure 5.3(a) for Gd and (b) for Dy is actually identical, the best images are selected from both metal reconstructions to show the bias dependence features. Figure 5.4(a) is an STM image at +0.8 V taken from a Gd deposited sample, where the three maxima in the subunit appear with similar intensity (regime II). In image (b) taken from a 0.2 ML Dy deposited sample at +0.28 V, the center row of maxima are very strong, and the other two rows are much less bright (regime I). Image (c) is of the same area as image (a) taken at a bias of +2.06 V, showing that the center row is totally invisible, but the other two rows appear with significant intensity (regime III). The same regimes have been observed in the Dy:  $2\times 4$  superstructure[13], which is not surprising to us since both  $2\times 4$  and  $2\times 7$  superstructures are composed of the same groups of three maxima as discussed above. Another feature we can see from the three images is the intensity change in the bright strips, especially in (b) where the strip breaks into a row of maxima of the same  $2a_{Si}$  ( $1a_{Si}=0.384$  nm) periodicity along Si [110] as the subunits.

Further observations show that each regime does not appear only at a specific bias, but in a certain range. Additionally, the same regime in  $2\times 4$  and  $2\times 7$  superstructures appears in similar ranges, as illustrated in Figure 5.5, in which the measurement biases are separated into the three regimes. The measurements for Dy:  $2\times 4$  are numerous



enough to assign a specific range for each regime, i.e., 0.08 ~ 1.0 V for regime I, 1.04 ~ 1.39 V for regime II, and 1.4 ~ 3.01 V for regime III (an extension from 2.01 V to 3.01 V is made to match with Dy: 2×7). The boundaries of the corresponding regime for Dy: 2×7 are shown as matching with Dy: 2×4 where data is absent. For Gd: 2×7, a certain range can also be assigned to each regime, but the available data are not enough to determine the exact boundary between regimes. However, one thing that is clear is the bias range of regime II of Gd: 2×7 overlaps with that of regime I of Dy: 2×7 or Dy: 2×4. This difference is a reflection of the difference in the electronic structure between Gd and Dy.

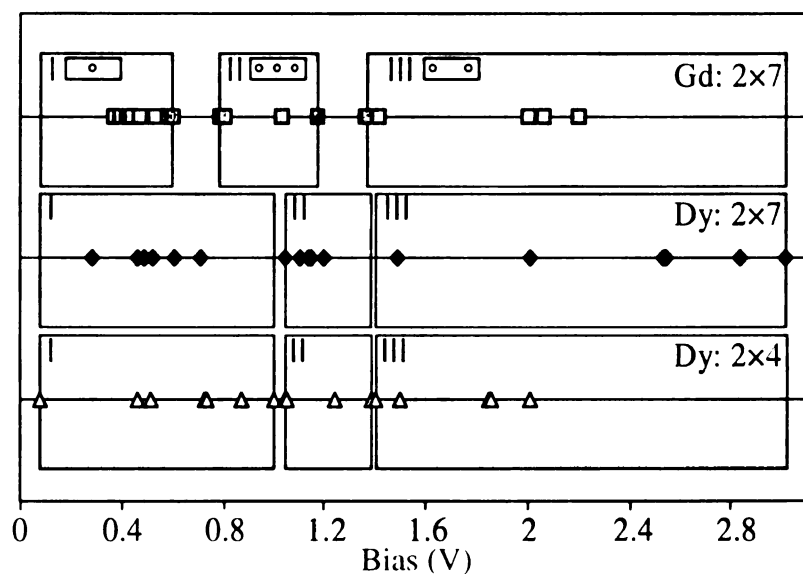


Figure 5.5 Bias voltage ranges for three different regimes in empty states imaging of the subunits in the Gd:2×7, Dy:2×7 and Dy:2×4 structures. Bias voltages for the individual measurements are shown.

The situation for the filled states is much simpler compared to the empty states. Generally, the appearance of the 2×7 superstructure is the same in a bias range of -0.45 to -3.26 V for both Dy and Gd, as shown in Figure 5.4(d). Only the center row of the three subunit maxima is visible (marked (1)), and the bright strip breaks into a row of maxima

(marked (2)) with a  $2a_{\text{Si}}$  periodicity along Si [110]. In some circumstances, the bright strip separates into two maxima along Si  $[1\bar{1}0]$ , as seen in (e). Note that Figure 5.4(d) and (e), and Figure 5.4(a) and (c) are STM images of the same area.

### 5.1.3 Atomic structure

As discussed for Figure 5.3, the three maxima subunits are the same for both  $2\times 4$  and  $2\times 7$  superstructures, and these maxima have the same registry with respect to the underlying Si, that is, in the place of a removed Si dimer. The next question is to determine the atomic configuration of the bright strip.

The structure of the bright strip can be extracted from the STM images shown in Figure 5.4(b), (d) and (e), since the bright strips in these images break into maxima. First thing we can see is that these maxima have the same periodicity as the three maxima subunits, which is  $2a_{\text{Si}}$  apart along Si [110]. If we draw straight lines parallel to Si  $[1\bar{1}0]$  in these images, antiphase shift (note that  $\frac{1}{2}$  unit cell shift along  $2\times$  direction in the  $2\times 7$  superstructure is  $1a_{\text{Si}}$  different) of the three maxima subunits can be observed in (d) and (e). Moreover, we can see that the bright strip maxima are not in line with the subunit maxima; they are about  $\frac{1}{4}$  unit cell off both sides of the straight line. Since we know the spacing between the straight lines is  $2a_{\text{Si}}$ , hence, the shift between the maxima of strips and subunits is  $\frac{1}{2} a_{\text{Si}}$ . Therefore, the strip maxima share the same atomic position in both filled and empty states, which is  $\frac{1}{2}$  Si unit cell shift from the subunits along Si [110]. The shift between maxima along the bright strip in different rows shown in (b) implies an antiphase shift, similar to that of the three maxima subunits.

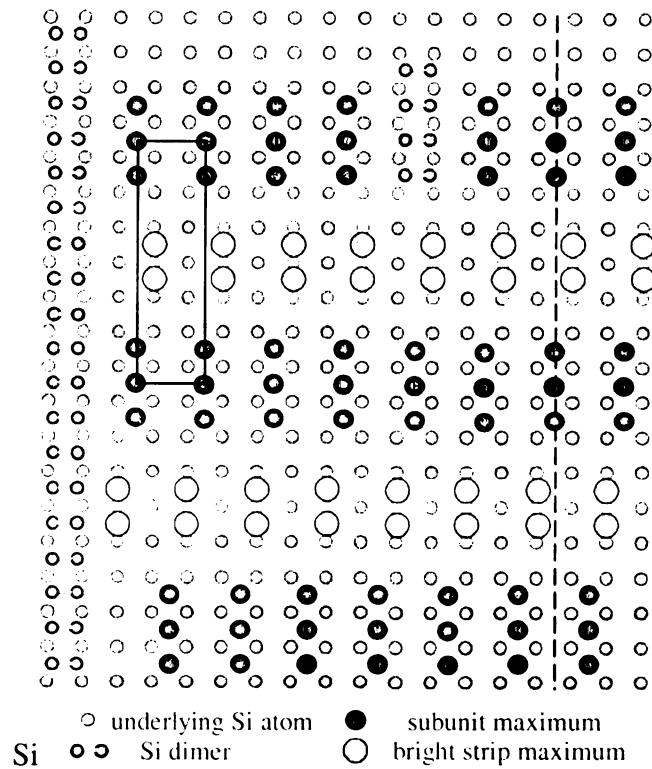


Figure 5.6 Diagram showing the atomic registry of the maxima in the  $2\times 7$  superstructure with respect to the Si (001) substrate. The  $2\times 7$  unit cell is marked by a black box, and a broken line is drawn to show the anti-phase shift of both the subunit maxima and bright strip maxima.

Based on this information, a diagram of the atomic scale features in the  $2\times 7$  superstructure is shown in Figure 5.6. The subunit maxima sit at the center of the  $1\times 1$  unit cells in the underlying layer, and the strip maxima sit in between two Si atoms, which is shifted exactly  $\frac{1}{2}$  Si unit cell away from the atomic position of the subunit maxima. The diagram also shows that the bright strips and the subunit rows actually have a gap between them. A  $2\times 7$  unit cell is marked, and the antiphase shift of both the subunits and the strip maxima is shown in the figure. One row and column of Si dimers are also shown to illustrate the registry of the  $2\times 7$  structure with the surrounding Si surface.

#### **5.1.4 Coverage dependence**

The occurrence of  $2\times 4$  and  $2\times 7$  phases are strongly coverage dependent in both Gd/Si (001) and Dy/Si (001) systems, as shown in Figure 5.7. The percentage of the surface covered by different phases is plotted against the nominal metal coverage. As seen in (a) for Gd, the Si surface is firstly  $2\times 4$  reconstructed up to 0.2 ML. Subsequently, the  $2\times 7$  reconstruction starts to appear at the cost of decreasing the  $2\times 4$  coverage up to 0.33 ML, at which the surface is almost entirely  $2\times 7$  reconstructed. Starting from 0.36 ML, 3D nanowires appear and occupy more area with increasing coverage up to 0.92 ML, decreasing the area covered by both 2D reconstructions. The  $2\times 7$  reconstruction dies off gradually, but the total percentage of surface covered by  $2\times 4$  reconstruction and  $2\times 1$  clean Si remains approximately constant after about 0.8 ML. This diagram implies that the whole surface could be totally  $2\times 7$  reconstructed at a certain coverage between 0.33 ~ 0.36 ML, which is also the coverage at which the nanowires start to nucleate.

Two methods have been used to grow Dy disilicide nanowires: depositing Dy onto a Si surface at 600°C, with and without post deposition annealing. As we can see from Figure 5.7(b) and (c), the nanowires start to appear at a much earlier coverage compared to Gd for either preparation. Details of nanowire and 3D island growth are discussed in the next chapter. What is clear is that the appearance of the Dy:  $2\times 7$  phase strongly depends on the post-annealing. It is promoted by quenching the sample immediately after the end of metal deposition at 600°C. There is no critical coverage at which the  $2\times 7$  covers the whole surface; nor is there a clear relationship between when the  $2\times 7$  phase decreases, and the nanowires appear. Nevertheless, the Dy  $2\times 7$  phase seems to be associated with coverages between 0.3 and 0.7 ML. A similar behavior is seen for the

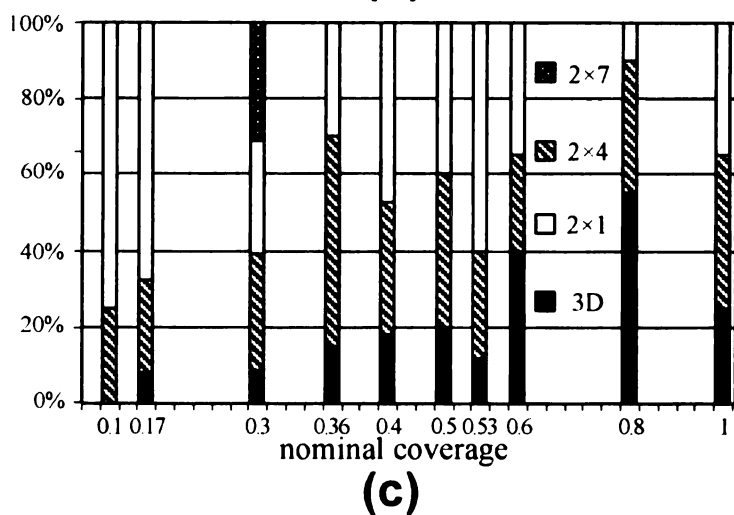
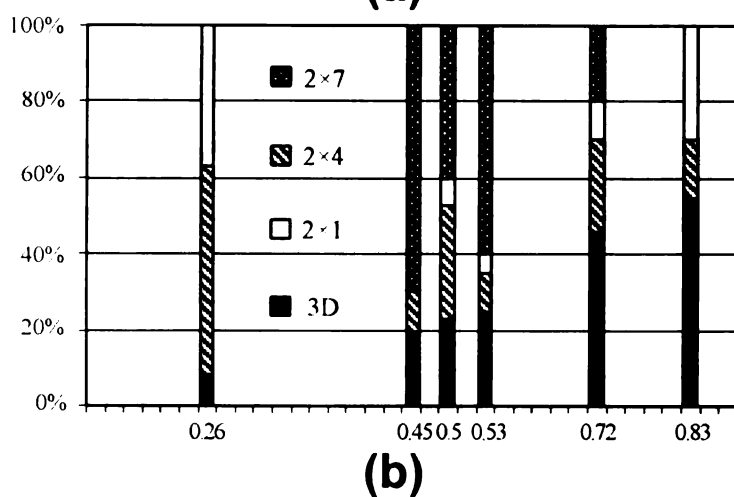
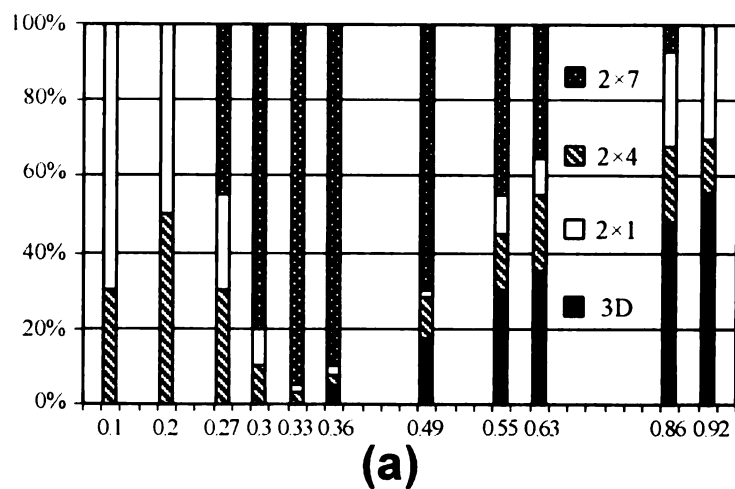


Figure 5.7 Coverage dependence of 2D and 3D phases appearing for (a) Gd grown on Si at 600°C with post deposition annealing; and Dy on Si at 600°C without (b) and with (c) post deposition annealing.

Ho/Si (001) system where the  $2\times 7$  is seen to coexist with the  $2\times 4$  in a range of coverage around 0.5 ML[117].

It is easiest to deduce a relationship between coverage dependence and the metal content of the  $2\times 7$  phase for the case of Gd. If we make the same assumption that was made for the Dy:  $2\times 4$  structure in Chapter 3, i.e., the number of metal atoms and empty states maxima in the STM images are the same, then the metal density in the  $2\times 4$  phase is  $3/8 = 0.375$  ML, and the metal density in the  $2\times 7$  phase is  $5/14 = 0.357$  ML. Both of these numbers are consistent with the behavior shown in Figure 5.7(a), at least up to 0.36 ML. The agreement beyond this point depends on our assumption about the metal content of the 3D nanowires. If we assume that there is only one layer of RE metal atoms inside the nanowires, then they have an areal density of 1 ML, as implied by the RE disilicide bulk structure[12]. Hence, a total metal coverage can be calculated based on the data given in Figure 5.7, which is plotted versus the nominal coverage as shown in Figure 5.8 for all three cases. The straight line in the figure is a reference line assuming an ideal match between calculated coverage and nominal coverage. The three curves match with the reference line very well in the beginning then start to deviate from it at a certain coverage, about 0.5 ML for both Gd and Dy-cutoff curves, and 0.36 ML for Dy-annealed curve. This deviation is caused by both second layer nanowire growth and 3D island formation, which is discussed in the next chapter. Nevertheless, the agreement between each curve and the reference line gives us a clue that the atom assignment to different phases is reasonable. We can further test this conclusion by assuming that there are other possibilities for the RE atom density assigned to the  $2\times 7$  superstructure, e.g., 2, 3, 4, 6, 7, and 8 atoms per unit cell. The total coverage is recalculated according to each assignment

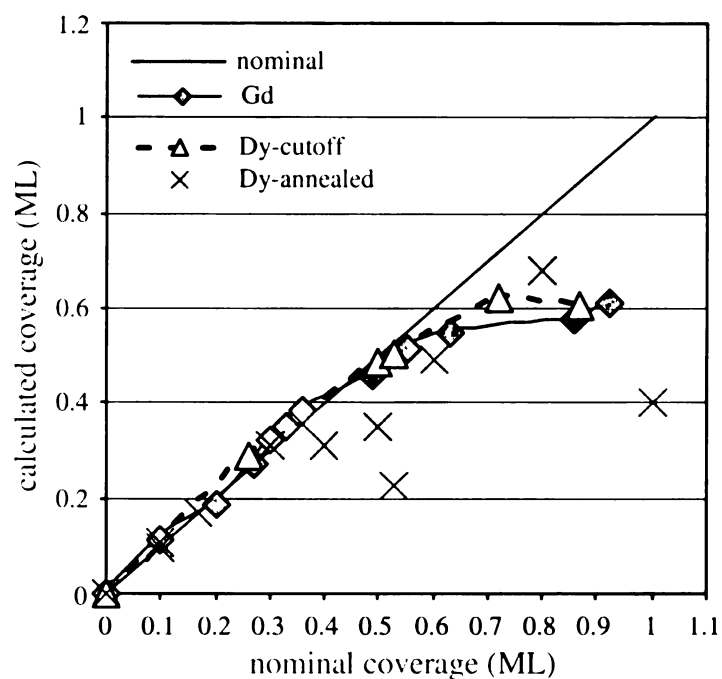


Figure 5.8 The calculated coverage of the three cases shown in Figure 5.7 is plotted against the nominal coverage.

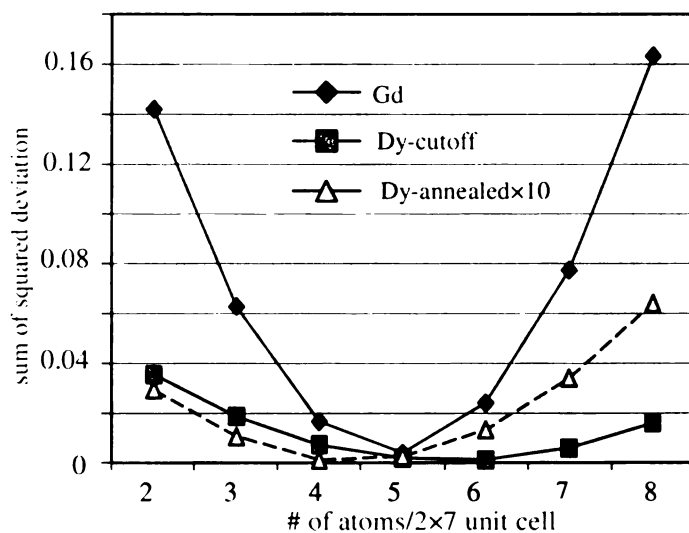


Figure 5.9 Sum of squared deviation between the actual and calculated coverage plotted versus the assumed number of metal atoms in the  $2 \times 7$  superstructure.

for the data in Figure 5.8 up to the coverage that starts to deviate from the reference line significantly, resulting in a deviation from the nominal coverage at each data point. These deviations are squared and summed up for each case and plotted in Figure 5.9. It can be seen that the minimum error is 5/14 for Gd, 6/14 for Dy-cutoff, and 4/14 for Dy-annealed. Allowing for experimental error, and the fact that the  $2\times 7$  superstructure should be the same for all cases, 5/14 ML RE atoms is the best assignment for the  $2\times 7$  superstructure.

## 5.2 Discussion

The similarities in the appearance and bias dependence of the  $2\times 7$  reconstructions formed by Gd and Dy suggest that they are actually the same superstructure. However, the chemical identities of the metals still play a role, as suggested by the difference in the details of bias dependence shown in Figure 5.5, and the difference in the coverage dependence of the  $2\times 7$  superstructure shown in Figure 5.7.

Similarities also exist in the  $2\times 4$  and  $2\times 7$  superstructures since they share the same three maxima subunits and these maxima have exactly the same atomic position and bias dependence. Considering the close relationship between  $2\times 4$  and  $2\times 7$  superstructures, the evolution from  $2\times 4$  superstructure to  $2\times 7$  superstructure could be a result of increasing strain in the  $2\times 4$  reconstructed areas, which means the appearance of bright strips between the three maxima subunit rows can ease the strain along  $\text{Si}[1\bar{1}0]$ . The intensity of the three maxima within each subunit in the  $2\times 7$  superstructure are more regular compared to the  $2\times 4$  superstructure, in which an alternation of atomic buckling (LHL, HLH) along  $[1\bar{1}0]$  is observed and explained by atomic buckling caused by strain



[13]. The absence of this alternation in the  $2\times 7$  also suggests that the  $2\times 7$  superstructure is less strained due to the formation of the bright strips.

The  $2\times 7$  reconstruction appears only after the  $2\times 4$  reconstruction covers a certain percentage, about 50%. The  $2\times 4$  phase almost always coexists with areas of clean surface. The  $2\times 7$  phase appears only when the  $2\times 4$  phase is also present. In cases where areas of  $2\times 7$ ,  $2\times 4$  and clean Si are present, the areas of clean surface are bordered by the  $2\times 4$  but not the  $2\times 7$ . Also the  $2\times 7$  reconstruction dies off at higher coverage because of the decrease in the 2D reconstructed areas due to the consumption of metal atoms by nanowires or 3D islands. The behavior of the  $2\times 7$  phase is consistent with it being associated with more metal on the surface than the  $2\times 4$  phase. This seems to be inconsistent with the fact that the areal density of metal in the  $2\times 7$  phase is slightly less than that for the  $2\times 4$  phase. However, the total amount of metal accommodated in the  $2\times 7$  phase is generally higher than that in the  $2\times 4$  phase since the percentage of the surface covered in the  $2\times 7$  phase, when it is present, is usually higher than the percentage covered by the  $2\times 4$ .

A specific atomic structure for the  $2\times 7$  phase is not being proposed here. However, any model must be consistent with the registry of atomic scale features shown in Figure 5.6. While it is highly suggestive that the number of empty states maxima and metal atoms is the same, it is not possible to state that the maxima correspond to metal atoms. In fact it is possible that the metal atoms occupy sub surface positions and that the surface is terminated by Si atoms, as has been suggested for the surfaces of RE silicides grown on both Si (111) and Si (001)[107, 118].

Furthermore, the metal content of the  $2\times 4$  and the  $2\times 7$  phases may not be exactly the same for different RE metals. The  $2\times 4$  phase appears to be the same for Gd and Dy. In addition, the Yb: $2\times 4$  structure also has three atoms per unit cell[119]. On the other hand, the Ho: $2\times 4$  structure appears to have only 1.5 metal atoms per unit cell[117]. More analysis by other analytical techniques will be necessary to solve this structure in these RE metal / Si (001) systems.

### 5.3 Conclusions

Detailed examination of the  $2\times 7$  reconstruction of the Si (001) surface induced by Gd and Dy shows that this phase appears to be the same for both metals, and is similar to the  $2\times 7$  phase induced by Ho[117]. Furthermore, the  $2\times 7$  structure contains subunits whose appearance and bias dependence in STM images is the same as the  $2\times 4$  superstructure induced by Gd, Dy, and several other RE metals. The registration of the maxima seen in the STM images with respect to the surrounding Si substrate has been determined for both the  $2\times 4$  and the  $2\times 7$  phases. Coverage dependent measurements show that the metal content of the  $2\times 4$  and the  $2\times 7$  phases is  $3/8$  and  $5/14$  ML, respectively. Any model for the atomic structure of the  $2\times 7$  phase will be constrained by the STM images and the measured metal content. Aside from the structural similarity of the Dy and the Gd induced phases, there are some differences between the two metals, particularly with respect to the coverage dependent growth behavior.

## **Chapter 6 A comparison of Dy and Gd silicide nanowire growth**

In this chapter, more data on Gd silicide growth is presented, and the behavior of the two metals is compared. In particular, some insight into the differences between the two metals is obtained by comparing the Gd data with Dy growth for a wider range of conditions than what has been previously discussed in Chapter 4. This chapter also includes data on a particular variant of nanowire growth: growth of parallel arrays of Dy and Gd nanowires on single-domain, vicinal Si (001) surfaces. Experimental results show that the growth temperature, annealing duration, metal coverage and metal varieties are important factors for RE silicide growth.

### **6.1 Growth on normal Si (001)**

#### ***6.1.1 General observations***

Generally, three types of structures can be formed when depositing RE metals onto Si (001) substrates at elevated temperature -- nanowires, 3D islands, and 2D reconstructions. All of these structures can coexist together on the same surface, as shown in Figure 6.1. This sample was prepared by depositing 0.4 ML Dy on Si (001) substrate at 600°C with 5 min post deposition annealing (PDA). As seen in the figure, long islands (nanowires or nanowire bundles) run in two perpendicular directions, with compact rectangular 3D islands lying at the nanowire junctions. Additionally, second layer growth can be observed clearly on top of both the nanowires and the 3D islands. There are two types of 3D islands can be seen, one with a flat surface and one with a wavy surface. Although it is not apparent in this rendering, the substrate is not bare Si, but is reconstructed by the RE metal. The 2D reconstructions, usually 2×4 and 2×7 for Dy and Gd, have been

discussed in Chapter 3 and 5. The nanowire and the 3D island growth of both Dy and Gd disilicides show strong coverage dependence. The Dy silicide 3D island is very sensitive to the annealing duration, as will see from the comparative experiments with and without PDA.

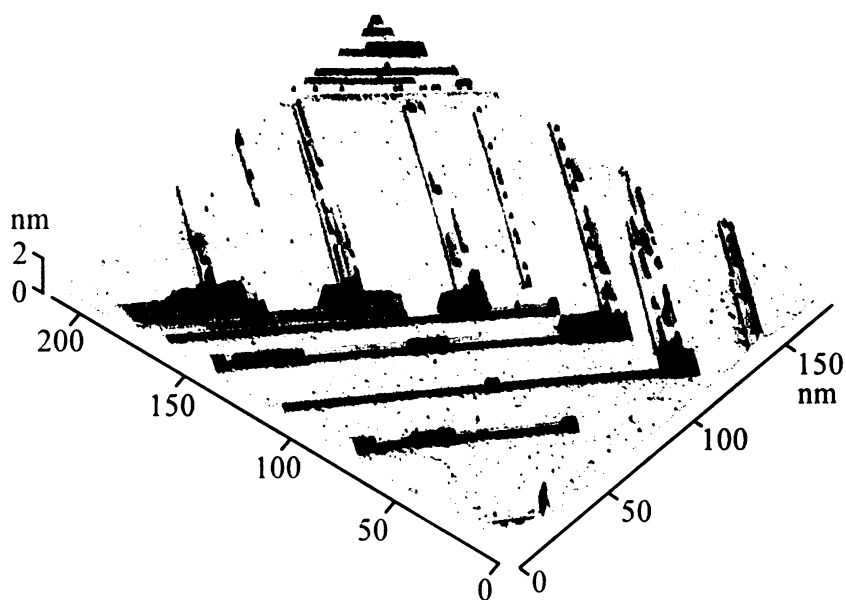


Figure 6.1 Topography of Si (001) surface with 0.4 ML Dy deposited, showing coexistence of nanowires and 3D islands, and second layer growth.

### 6.1.2 Gd silicide nanowire growth

When depositing Gd onto Si (001) surface at 600°C with 5-10 min PDA, only 2D reconstructions ( $2\times 4$  and/or  $2\times 7$ ) are formed up to about 0.33 ML. The Si surface is almost entirely  $2\times 7$  reconstructed at 0.3 ML mixed with small areas of  $2\times 4$  reconstruction and  $2\times 1$  clean Si. When an additional 0.06 ML Gd is deposited onto this sample, nanowires appear, as shown in Figure 6.2(a), implying the existence of a critical coverage for nanowire nucleation between 0.3 ML and 0.36 ML. The surface in (a) is fairly rough due to the existence of a large number of Si steps. It is clear that each

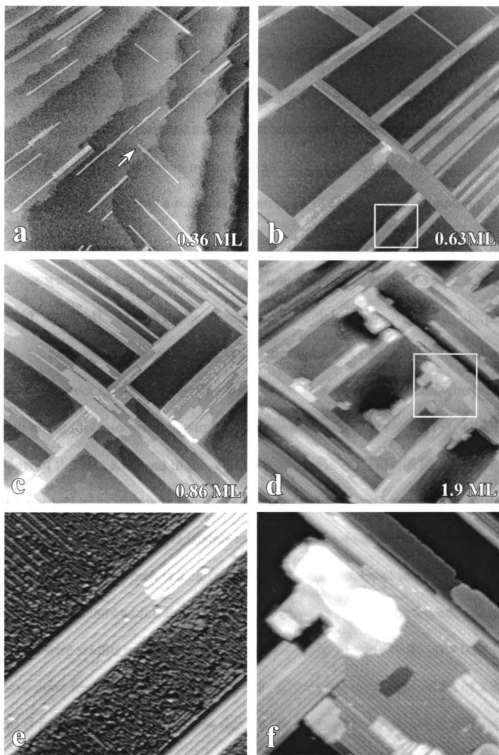


Figure 6.2 (a)-(c) ( $350 \text{ nm} \times 350 \text{ nm}$ ) and (d) ( $300 \text{ nm} \times 300 \text{ nm}$ ) are STM images which show coverage dependent topography of the Gd/Si (001) surface. (e) ( $60 \text{ nm} \times 60 \text{ nm}$ ) is a closer view of the area enclosed in the white box in (b). (f) ( $75 \text{ nm} \times 75 \text{ nm}$ ) is a closer view of the white box in (d).

nanowire grows on a flat terrace,  $90^\circ$  rotated from those on adjacent terraces. It is worthy to note that the nanowires can cross a step, an example of which is marked by an arrow in the image. This is not observed when depositing metal in one evaporation onto a clean sample. We believe this occurs due to extended annealing that occurs during evaporation calibration when adding additional metal onto an old sample. Similar phenomenon has been observed when annealing a room temperature (RT) Dy deposited sample up to  $600^\circ\text{C}$ , as will be discussed later on.

Surfaces with more Gd deposition are shown in Figure 6.2(b) at 0.63 ML, (c) at 0.86 ML, and (d) at 1.9 ML. At this image magnification, only the overall surface morphology is visible. As coverage increases in (b) and (c), the nanowires become denser and wider, with additional layer growth on top. The wide nanowires are actually nanowire bundles, consisting of parallel nanowires separated by narrow trenches, as seen in (e), which is a closer view of the area enclosed in the white box shown in (b). Gd silicide nanowires are more often observed as nanowire bundles compared to Dy silicide nanowires. At the highest coverage shown in (d), 3D islands are formed. The wide wires are still nanowire bundles, as shown in (f) which is a closer view of the area enclosed in the white box in (d), in which 3D islands with flat top and wavy surface can also be observed.

The nanowire widths are measured as multiples of the Si periodicity  $a_{\text{Si}} = 0.384 \text{ nm}$ , as we have done for Dy nanowires in Chapter 3. A minimum nanowire width of  $2 a_{\text{Si}}$  (0.77nm) is found, which is the same as that for Dy nanowire. The width distribution of Gd silicide nanowires, ranging between  $2a_{\text{Si}}$  and  $5a_{\text{Si}}$  as shown in Figure 6.3, is much narrower than that of Dy nanowires, which ranges between  $2a_{\text{Si}}$  and  $16a_{\text{Si}}$ . Nanowire

bundles can consist of a large number of single nanowires, and the total width of the bundle can be as much as 100 nm.

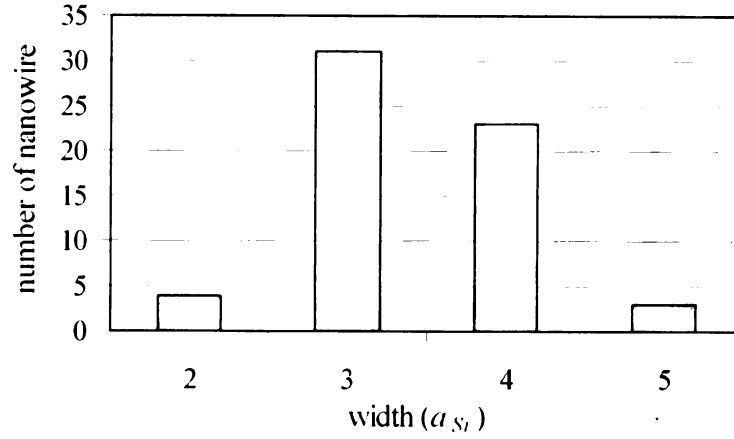


Figure 6.3 Width distribution of single Gd silicide nanowires in bundle.

### 6.1.3 Dy silicide nanowire growth

When using the same method to prepare Dy silicide nanowires, i.e., deposition with PDA, nanowires start to appear at a coverage as early as 0.1 ML, with significant 3D island formation above 0.3 ML. Figure 6.1 is a good example showing coexistence of nanowires and 3D islands at 0.4 ML. More details of growth with PDA have been discussed in Chapter 4. The growth of 3D islands is not desirable from the viewpoint of optimizing nanowire growth. We noticed in our experiments that the number of islands decrease with shorter annealing duration, implying the growth of 3D islands might be suppressed by shortening the annealing duration. Therefore, we tried another method to grow Dy silicide nanowires, shortening the annealing duration to zero by cutting off the heating current immediately after deposition, which we call post deposition quenching (PDQ). Figure 6.4(a)-(c) show the nanowire growth with increasing coverage with PDQ. No 3D islands are formed at a coverage as high as 0.53 ML in (b), and only a small

number of islands can be found at the junctions of nanowires at a coverage 0.72 ML in (c). One other significant difference from PDA growth is that most of the nanowires formed under 0.5 ML are single nanowires, as seen in (a). A small number of nanowire bundles with slight additional layer growth can be seen in (d) at 0.53 ML, which is a closer view of the area inside the square box in (b).

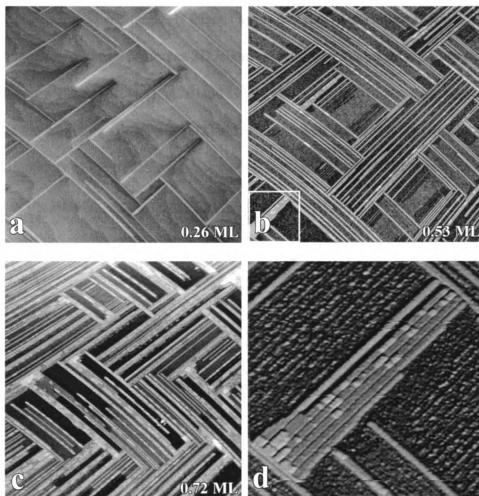


Figure 6.4 (a)-(c) are STM images (all 350 nm $\times$ 350 nm) showing coverage dependent topography of the Dy/Si (001) surface prepared by PDQ. (d) (75 nm $\times$ 75 nm) is a closer view of the area enclosed in the square box in (b).



#### 6.1.4 3D islands

As discussed above, the growth of 3D islands can be suppressed by PDQ, at least at lower coverage. On the other hand, what happens if we increase the post deposition annealing duration? Figure 6.5 (a) shows a sample prepared by depositing 0.6 ML Dy onto Si surface with 10 min post annealing. Both nanowires and 3D islands can be observed as expected. If we continue to anneal this sample at 600°C for 1 hour, most of the nanowires disappear and large 3D islands appear as shown in (b), implying that for Dy, long annealing duration promotes 3D island growth. The 3D islands can grow downward below the Si surface, e.g., island (1), or above the Si surface, e.g., island (2). The inset is the height profile of island (1) along the broken line, showing the island is situated completely in the trench, which is caused by consumption of Si atoms during formation of the island.

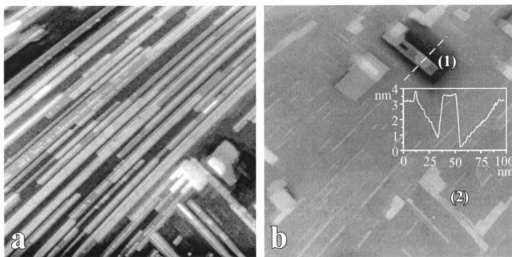


Figure 6.5 Topography of (a) 0.6 ML Dy deposited sample prepared by 10 min PDA, image size is 200 nm×200 nm, and (b) the same sample shown in (a) which was annealed another 1 hour, image size is 350 nm×350 nm. The inset in (b) is the height profile of island (1) along the broken line.

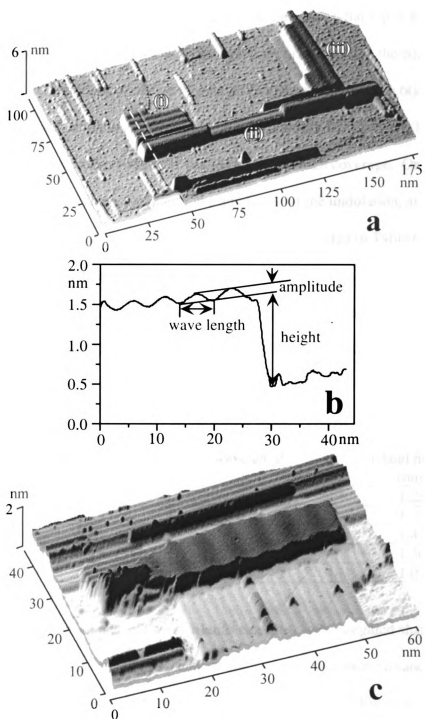


Figure 6.6 (a) 3D rendering of wavy island (2) shown in Figure 6.5(b). (b) The height profile of the wavy island along the broken line in (a). (c) Wavy island formed by deposition of 0.92 ML Gd.

Again, there are two types of islands can be seen, one with a flat top, e.g., island (1), and one with a wavy surface, e.g., island (2), which is consistent with the islands shown in Figure 6.1. A 3D rendering of the wavy island (2) is shown in Figure 6.6(a), and the surface undulates sinusoidally, as shown by the height profile in Figure 6.6(b). Wavy surfaces have also been observed in Gd silicide islands at high coverage. One example is shown in Figure 6.6(c). The wave length, the amplitude of the undulation, and the island height measured from Si surface for a number of islands are listed in Table 6.1. It shows that the undulation amplitude is very close for all of the wavy islands, on average 0.13 nm. The wavelength varies, but no obvious relationship can be established between the wave length and the island height. Note that the amplitude and wavelength are not bias dependent.

Table 6.1 Measured amplitude, wavelength and height of wavy islands.

	amplitude (nm)	wavelength (nm)	island height (nm)
DySi <sub>2</sub>	0.10	5.93	1.23
	0.14	6.24	1.05
	0.13	6.92	1.42
	0.15	7.16	1.50
GdSi <sub>2</sub>	0.13	5.58	1.07

Both of the flat top islands and wavy islands can grow into elongated shapes that look like wires. The 3D rendering in Figure 6.6(a) shows that the members (ii) and (iii) are wavy, and elongated in a direction perpendicular to the undulation direction. This is different from member (i) and the Gd island in Figure 6.6(c), which are both elongated parallel to the undulation direction but have much smaller lengths than (ii) and (iii). A general conclusion about a correlation between island elongation and undulation direction cannot be given due to the limited number of observations of these wavy islands.

We draw a distinction between these “elongated islands” and nanowires based on the fact that they are much wider; the width of these islands is in the range of 8 ~ 17 nm for Dy silicide, much larger than the width defined for nanowires, 0.8 ~ 6 nm for single Dy silicide nanowires, and 0.8 ~ 2 nm for single Gd silicide nanowires. These elongated islands can grow fairly long. The longest island we observed is 280 nm long, comparable to nanowires. These elongated islands coexist with even larger square or rectangular 3D islands whose widths are in the range of 20-30 nm.

### ***6.1.5 Height quantization***

Both the nanowires and the islands exhibit layer-by-layer growth, which is evident from Figure 6.1, 2 and 5. As we have done for Dy nanowires discussed in section 4.1.2, the height of Gd nanowires were measured with respect to the substrate surface, giving us a minimum height ranging between 0.48 nm and 0.50 nm, with an average of 0.49 nm. This height range is smaller than that of Dy nanowires, which range between 0.48 nm and 0.56 nm in both filled and empty states, with an average of 0.52 nm, as mentioned in Chapter 4. However, both averages are comparable. The height of 3D islands is hard to measure since they can grow on top of the nanowires (Figure 6.2(f)), or in a trench (Figure 6.5(b)). Generally, 3D islands have heights above 1 nm. A consistent minimum height cannot be found for the 3D islands, as shown in Table 6.1, which could be a clue that these 3D islands are different phase from nanowires.

Once again, it is useful to measure the height of additional layers with respect to the top surface of adjacent or underlying nanowires or islands in order to minimize the effects of different surface structure. It was mentioned in Chapter 4 that the height of additional layers on Dy silicide nanowires is actually quantized in increments of 0.35 nm.

The additional layers on top of wavy islands are also quantized in the same thickness, but that of flat islands have a quantum height of 0.66 nm, and another possible value larger than 0.84 nm. Similarly, the additional layers grown atop Gd silicide nanowires also have an average height of 0.35 nm. We do not have enough data for Gd silicide islands since they grow so infrequently.

#### ***6.1.6 Coverage dependence***

The appearance of each phase is strongly related to the metal coverage under different growth conditions, as shown in Figure 6.7, which has more data above 1 ML compared to Figure 5.7. The diagrams in the figure are plotted with the percentage of the surface covered by different phases versus the nominal coverage, where 3D phases include both nanowires and 3D islands. All the samples in (a) were prepared by depositing Gd onto 600°C heated Si substrates with 5 to 10 min PDA. And all the samples shown in (b) and (c) were prepared by depositing Dy onto Si surface of 600°C with PDA and PDQ, respectively. These diagrams show that the area covered by 3D phases increases with increasing coverage before 1 ML, but stop increasing after 1 ML and even drops, although it increases at the highest coverage measured in (c). A specific minimum coverage for Gd silicide nanowire growth can be seen in (a), between 0.33 ML and 0.36 ML, which might correspond to the saturation coverage of 2×7 superstructure mentioned in the previous chapter. But such a critical coverage can not be seen for Dy from the available data as illustrated in (b) and (c), and the 3D phases start to appear at a much earlier coverage compared to Gd in (a).

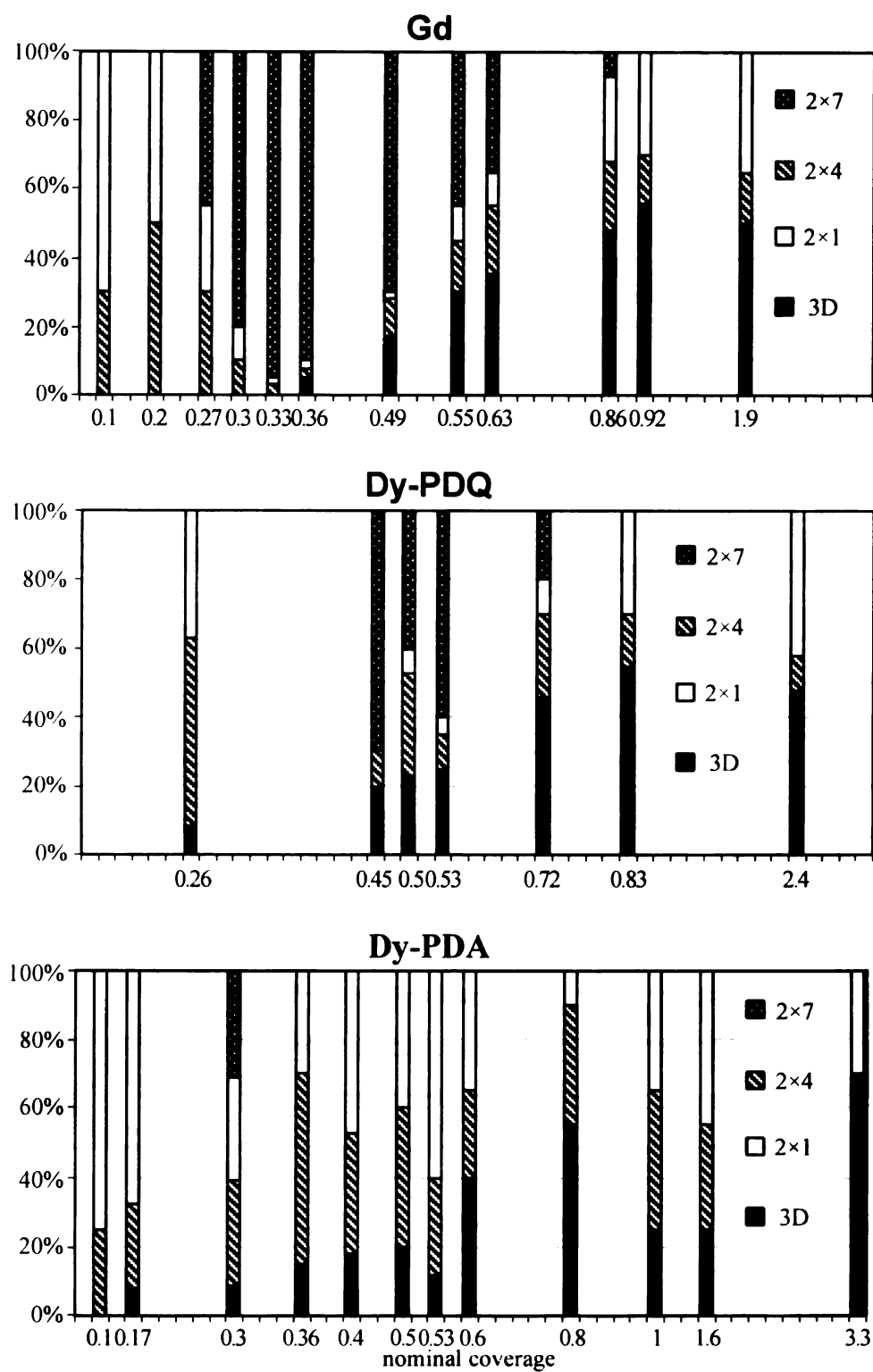


Figure 6.7 Coverage dependence of 2D and 3D phases appearing for (a) Gd grown on Si at 600°C with PDA; and Dy on Si at 600°C with (b) PDQ and (c) PDA.

Again, the total coverage can be calculated based on the same assumption made in the previous chapter, i.e., the metal density in Dy: 2×4 structure is 0.375 ML, and that in the 2×7 phase is 0.357 ML, and 1 ML in the nanowires of minimum height. The calculated results are plotted versus the nominal coverage as shown in Figure 6.8 for all three cases. The straight line in the figure is a reference line assuming an ideal match between calculated coverage and nominal coverage. The three curves match with the reference line very well in the beginning then start to deviate from it at a certain coverage, between 0.36 and 0.5 ML for all three curves. This deviation is caused by both second layer nanowire growth and 3D island formation, as shown in Figure 6.2 and 4.

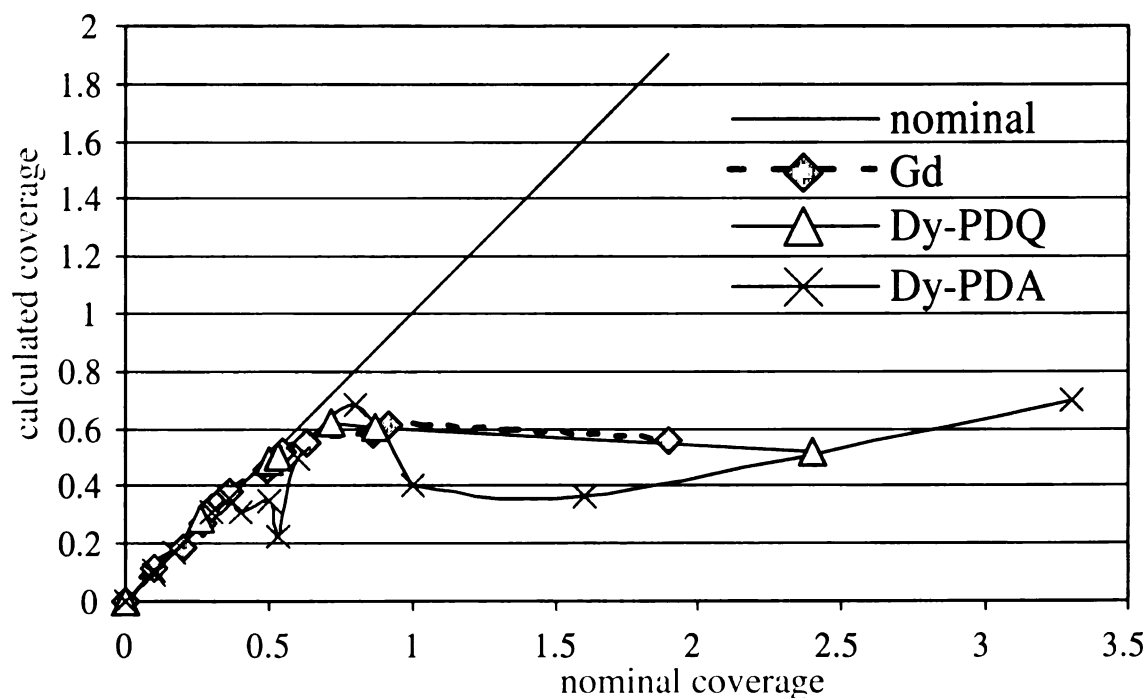


Figure 6.8 The calculated coverage of the three cases shown in Figure 6.7 is plotted versus the nominal coverage.

For Dy coverage less than 0.5 ML (Figure 6.4(a)), only single nanowires are formed. At 0.53 ML (Figure 6.4(b)), second layer growth and nanowire bundles start to appear. At

0.72 ML (Figure 6.4(c)), the nanowires are highly bundled with some population of second layer nanowire growth and 3D islands formed at the nanowire junctions. Since the second layer nanowires and 3D islands contain more metal atoms than one layer of nanowires, certain amount of metal atoms will be miscounted during calculation based on the assumption of 1 ML metal atoms in the nanowires.

The same conclusion can be obtained by observing the coverage dependence of Gd silicide growth shown in Figure 6.2. Generally, the Gd disilicide nanowires are more likely to appear as nanowire bundles, as shown in Figure 6.2(b)-(d). At 0.63 ML, second layer growth can be seen. At 0.86 ML in (c), the nanowires are highly bundled and second layer growth getting more and more populated, and 3D island growth can be seen in (d).

The coverage dependence of Dy silicide growth prepared with PDA has been discussed in Chapter 4. As shown in Figure 6.8, the Dy-PDA curve deviates from the reference line at about 0.36 ML, much earlier than that of Gd, and Dy-PDQ, which is caused by the early formation of 3D islands and second layer growth, as shown in Figure 6.1 at 0.4 ML with PDA. When the coverage is well above 1 ML, generally large 3D islands are formed no matter what condition is used. The irregular shape of the Dy-anneal curve might be a result of annealing duration since it is different from sample to sample in the range of 2 to 10 min.

Nevertheless, the degree of agreement between nominal and calculated coverages up to 0.5 ML shows that the assignment of metal density to the different phases is reasonable, as was discussed in Chapter 5.



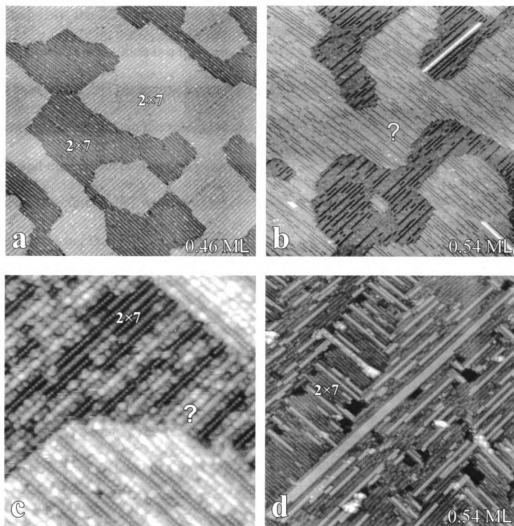


Figure 6.9 STM images (180 nm x 180 nm) showing coverage dependent topography of the Gd/Si (001) surface grown at 500°C with (a) 0.46 ML Gd deposited, taken at  $V_T = +0.44$  V; and (b) 0.54 ML Gd deposited, taken at  $V_T = +1.12$  V. (c) is a high resolution image (40 nm x 40 nm,  $V_T = -0.67$  V) of the 2D reconstruction appeared in (b). (d) is an STM image (180 nm x 180 nm) of the same sample shown in (b) which was annealed at 600°C, taken at  $V_T = +1.35$  V.

### 6.1.7 Growth behaviour at 500 °C

Figure 6.9 shows the growth behavior of Gd deposited onto Si (001) surface at 500°C. It can be seen that only 2x7 reconstruction is formed without nanowires at a coverage of 0.46 ML in (a), and nanowires start to appear at a coverage of 0.54 ML in

(b). Obviously, the 2D reconstruction in (b) is different from the  $2\times 7$  reconstruction in (a). As shown in (c), which is a high resolution image of the 2D reconstruction in (b), part of the area is still  $2\times 7$  reconstructed as marked, but the other areas are covered by an unknown structure. When the sample shown in (b) is annealed at  $600^{\circ}\text{C}$ , nanowires appear and the  $2\times 7$  reconstruction is recovered, as shown in (d). It is possible that the unknown structure is  $2\times 7$  with an excess of metal, and that this excess is able to form nanowires during the  $600^{\circ}\text{C}$  annealing.

The deposition of Dy at  $500^{\circ}\text{C}$  shows similar behavior. No nanowires are formed at 0.38 ML but  $2\times 7$  reconstruction, and large number of short nanowires are observed at 0.66 ML. Both samples were prepared without PDA. When annealed the sample in (a) was annealed at  $600^{\circ}\text{C}$  for 20 min, nanowire-like structures appear on a completely  $2\times 1$  reconstructed Si surface. Therefore, a conclusion here is that the metal atoms are more likely to be accommodated in a 2D reconstruction rather than in nanowires at lower growth temperature.

Preinesberger et al. [4] show one image of  $1\text{ \AA}$  Dy ( $= 0.47\text{ ML}$ ) on Si (001) grown at  $500^{\circ}\text{C}$ . They described the growth mode as "close-packed Dy silicide wires", but the image looks very similar to Figure 6.9(a) which is a  $2\times 7$  reconstructed surface, not wires.

#### ***6.1.8 Room temperature growth with PDA***

When depositing 0.16 ML Dy onto Si surface at room temperature, then annealing it at  $600^{\circ}\text{C}$  for 10 min, a black line is observed, as shown in Figure 6.10(a) in the filled states, and this line becomes bright in the empty states in (b). Figure 6.10(d) shows a "wire" across a step in the empty states, but it disappear in the filled states in (c). Apparently, the long nanowire-like features shown in Figure 6.10 are totally different

from the nanowires discussed elsewhere. Similar “black lines” have been observed after annealing a sample with nanowires, which could be traces of nanowires removed by annealing. Some other features could be described as nanowires that are buried so that their top surface is roughly level with the substrate. In any case, the growth behavior for RT deposited and post annealed samples is different than that seen for samples growth at elevated temperature, particularly in the initial stages of nanowire nucleation.

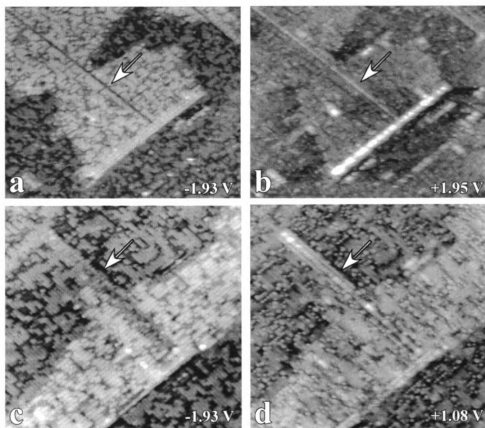


Figure 6.10 (a) and (b) (size: 60 nm $\times$ 70 nm), and (c) and (d) (size: 45 nm $\times$ 45 nm) are two pairs of dual bias images of a sample prepared by depositing 0.16 ML Dy onto Si at room temperature then annealing at 600°C.

### **6.1.9 Higher temperature growth**

Preliminary experiments have been done on growth of Gd silicide at higher temperature than 600°C. As we discussed, nanowires can be formed at 600°C when the coverage is above 0.357 ML. When we increase the growth temperature to 650°C, only 2×7 reconstruction without nanowires is seen at 0.45 ML for Gd. When depositing 0.4 ML Gd at 700°C, the Si surface is slightly 2×4 reconstructed, leaving most of the surface 2×1 reconstructed. Similarly, when depositing Dy at 700°C, no nanowires are formed at 0.48 ML. All of the nanowires are removed when the 0.78 ML sample with nanowires grown at 600°C is annealed at 700°C. In both cases for Dy, the 2×1 reconstructed clean Si surface is recovered with small area 2×4 reconstructed. Therefore, nanowires and islands cannot survive at 700°C for both Gd and Dy silicides. Furthermore, the apparent metal coverage on the surface is much less at either 650°C or 700°C than at 600°C, implying that deposited metal is lost from the surface, either by re-evaporation or diffusion into the substrate.

### **6.2 Growth on vicinal Si (001)**

For practical applications of these nanowires, it is of paramount importance to control where and how they grow. In particular, one proposed molecular electronics architecture has two perpendicular, planar nanowire arrays at two vertical levels and have switching molecules at nanowire junctions[120]. In order for RE silicide nanowires to be used as a component in this structure, growth of an array of parallel nanowires has to be realized. In the context of previous observations of nanowire growth on normal Si (001) substrates, the network structure composed of nanowires running in two perpendicular directions has

to be eliminated and the growth of secondary phases such as the 3D islands has to be suppressed.

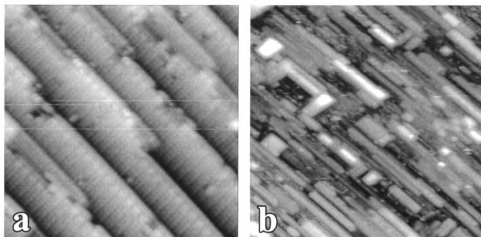


Figure 6.11 Scanning tunneling microscope (STM) images showing (a) a clean vicinal Si (001) surface with  $4^\circ$  miscut ( $19\text{ nm}\times 19\text{ nm}$ ), and (b) the vicinal surface after deposition of Dy at  $600^\circ\text{C}$  with 10 min postannealing ( $300\text{ nm}\times 300\text{ nm}$ ).

The most straightforward approach to grow a parallel array of nanowires is to use a vicinal Si (001) substrate, as shown in Figure 6.11(a). This particular substrate is tilted  $4^\circ$  off towards  $\text{Si}[1\bar{1}0]$ , resulting in a double height step spacing of  $39\text{\AA} \approx 10a_{\text{Si}}$ . All the steps are perpendicular to the Si dimer row direction, and all Si dimers are parallel to the step edge. This image shows a typical area of the surface with less than 5% minority dimer orientation, due to local splitting of the double height steps. Since nanowires grow perpendicular to the Si dimer row direction on the substrate, they would grow parallel to the step edges on the vicinal surface. Figure 6.11(b) shows the result of Dy deposition on the single domain Si (001) surface under typical growth conditions used for growth on flat substrates, i.e. deposition at a substrate temperature of  $600^\circ\text{C}$ , and several minutes of PDA at the same temperature. Dy silicide growth has disrupted the step distribution on the surface, and as a result, there are short nanowires running in both directions as well as

a significant population of rectangular silicide islands. This is clearly not the way to prepare a single domain nanowire array.

We have tried two different approaches to form parallel nanowire arrays on single domain vicinal Si (001). The first is to vary the growth kinetics, and the second is to optimize the choice of RE metal. In either case, the central issue is to minimize the growth of the large 3D islands, whose larger volume in comparison to nanowires implies a greater local consumption of silicon on the substrate, which in turn greatly affects the step distribution on the surface. This is clearly happening in the case of the  $4^\circ$  miscut vicinal surface in Figure 6.11(b).

For Dy, it is possible to greatly reduce the relative proportion of 3D islands to nanowires by cutting off the substrate heating current immediately at the point at which the metal deposition ends (i.e., PDQ, or without PDA), as discussed sections 6.1.3 and 6.1.4. It is clear that without PDA, the density of nanowires is higher and there are virtually no rectangular islands on the surface, whereas annealing time increases the relative density of 3D islands versus nanowires. This behavior suggests that the nanowires are in fact a metastable phase.

With this in mind, Dy growth experiments were repeated on vicinal surfaces, without PDA. A typical result is shown in Figure 6.12(a). The number of rectangular islands is greatly reduced, and furthermore most of the deposited Dy has formed into parallel nanowires whose length is limited only by step wandering, or misorientation between the step edge directions and the  $[1\bar{1}0]$  direction. When annealing this sample for another 30 min, nanowires disappear, and 3D islands appear, the same as what we discussed for

growth on normal Si substrates. Besides rectangular islands, a fairly long elongated island forms running from the upper right to lower left as seen in (b).

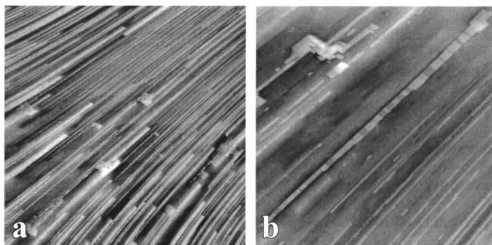


Figure 6.12 (a) STM image ( $800\text{ nm}\times 800\text{ nm}$ ) showing parallel nanowires formed on a  $0.38\text{ ML Dy}$  deposited vicinal Si (001) surface without PDA. A small number of 3D islands still can be seen. After annealing this sample 30 min, the topography is shown in (b) of image size  $420\text{ nm}\times 420\text{ nm}$ . 3D islands of various shapes appeared, and only a small number of nanowires survived.

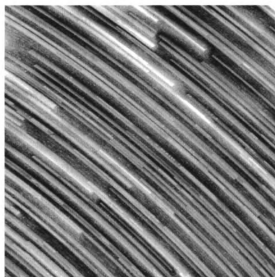


Figure 6.13 STM images showing a parallel nanowire covered surface free of islands formed by depositing  $0.77\text{ ML Gd}$  on a vicinal Si (001) substrate ( $300\text{ nm}\times 300\text{ nm}$ ). The sample was prepared with 5 min PDA.

Another approach to improving nanowire growth is the judicious choice of metal. Since these nanowires arise due to an anisotropy in lattice mismatch between the silicide and the substrate, and in particular since there is a good match between the silicide and the silicon along the long dimension of the nanowire, one possible criterion for choice of metal would be the best possible match between the a dimension of the hexagonal silicide, and the lattice constant ( $a_{Si} = 3.84\text{\AA}$ ) of the Si (001) surface along  $\langle 1\bar{1}0 \rangle$  directions. For example, Dy has a mismatch of -0.23% in this direction, and in general, nanowire formation is seen for metals with less than 1.2% mismatch [7]. Y would appear to be an even better choice with 0.0% mismatch. However, we have found that Y nanowire growth can be problematic due to growth of 3D islands that are not suppressed by quenching.

A more objective figure of merit for growth is a high ratio of nanowires to 3D islands. We have obtained the best results for Gd which has +0.96% mismatch along  $a$ . Figure 6.2(b) shows 0.63 ML of Gd grown on flat Si (001), with PDA. These are similar growth conditions as the Dy surface shown in Figure 6.5(a). There are only well-ordered bundles of nanowires on the surface, with no islands seen even at the nanowire junctions. Gd nanowire growth on the vicinal surface is shown in Figure 6.13. In this case, the surface was grown under very similar conditions as on the flat surface, i.e. with 5 minutes PDA. The surface is covered in parallel nanowires, and 3D island growth is absent, just as on the flat surface.



## **6.3 Discussion**

### ***6.3.1 Effects of annealing and growth temperature***

Annealing duration plays a very important role in the growth of Dy silicide growth. Longer annealing duration promotes 3D island growth. With PDA, the 3D islands can appear as early as 0.3 ML, but appear after 0.5 ML with PDQ. Further annealing drives metal atoms to leave nanowires and form large 3D islands. Annealing can also affect the nanowire bundling. Similar to island growth, the nanowires start to bundle at about 0.3 ML with PDA, but are still in single at 0.5 ML with PDQ. Additionally, annealing can affect the growth of 2D phases, for example, the  $2\times 7$  reconstruction appears in a very narrow range with PDA.

The effect of annealing on Gd silicide growth does not appear to be as strong as on Dy silicide growth. The Gd nanowires are very stable upon annealing without transforming into islands, and the island growth depends mainly on coverage. Unfortunately, we have not done comparable experiments on Gd silicide growth with PDQ and with longer time annealing.

The growth temperature is also an important factor during RE silicide growth. At low temperature like 500°C, the nanowires start to appear at higher coverage compared to 600°C, more metal atoms enter the 2D phases. But at higher temperature than 600°C, the surface starts to lose metal atoms due to re-evaporation or diffusion, and it seems that silicides do not survive extended annealing at 700°C.

### ***6.3.2 Multiphase coexistence and atomic model***

The effect of annealing duration on the growth of nanowires and islands could result from the competition between tetragonal/orthorhombic and hexagonal phases, which has

been observed for thick films (>20 nm) of Gd silicide on Si substrates by Molnár et al. [67, 68, 121]. The hexagonal phase has lower activation energy of formation than the orthorhombic phase, but the difference is very small, and the ratio of two phases strongly depends on the annealing temperature, annealing duration and thickness. This is relevant to submonolayer growth of RE silicides on Si (001) if we assign hexagonal structure to nanowires and orthorhombic/tetragonal structure to 3D islands as has been done for the case of Dy silicide in Chapter 4.

The three types of structures are closely related. When growing on Si (001), the hexagonal structure has two orientations,  $\text{RESi}_{2-x} (1\bar{1}00) // \text{Si} (100)$  with  $\text{RESi}_{2-x} [0001] // \text{Si} [01\bar{1}]$  and  $\text{RESi}_{2-x} (1\bar{1}00) // \text{Si} (100)$  with  $\text{RESi}_{2-x} [0001] // \text{Si} [0\bar{1}\bar{1}]$  [39, 64, 80, 81], and the orthorhombic and tetragonal structures have the same orientation (note that the orthorhombic  $\text{GdSi}_2$  type structure is only a deformation of the tetragonal  $\text{ThSi}_2$  type structure),  $\text{RESi}_{2-x} (001) // \text{Si} (001)$  with  $[100] // \text{Si} [1\bar{1}0]$  [57, 61, 82]. Based on this information, atomic models can be built for the growth of hexagonal and tetragonal phases, as shown in Figure 6.14, in which (b) and (c) are the side views of the first and second layer nanowire growth and 3D island growth, respectively. 14(b) is a revised version of the model shown in Figure 4.9. It can be seen that at the interface between silicide and Si substrate in both models, the metal atoms occupy a position essentially the same as that in the bulk silicide of both structures.

The two silicide structures in (b) and (c) can be described as different arrangements of the same building unit block: a parallelepiped with eight silicon atoms as apexes, and a rare earth atom at the center [33], which is shown in (a) and marked by a rectangular box in both models. These unit blocks are stacked along the [001] direction in the tetragonal

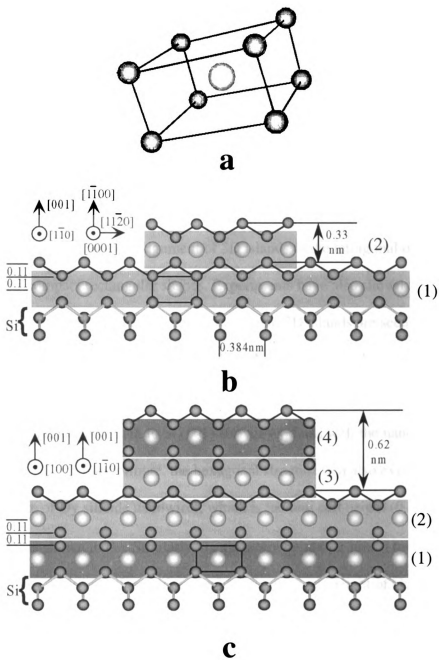


Figure 6.14 Side views of (b) hexagonal and (c) tetragonal RE silicides grown on Si (001) substrate, both of which can be built from the unit block shown in (a).

and orthorhombic structures, and along the  $[1\bar{1}00]$  direction in the hexagonal structure.

All of the blocks in (b) are in the same vertical plane, translated half unit block between each other in the hexagonal structure. While in (c), the layers (2) and (3) are in the same

vertical plane and reserve the same relationship between blocks as that in the hexagonal structure, but layers (1) and (4) are in another vertical plane, translated half unit block into the paper with respect to layers (2) and (3), as marked by different shades. In addition, the largest face of the building element is square in the tetragonal structure, and rectangular in the orthorhombic and hexagonal ones. The lattice parameters of the tetragonal and hexagonal structures are related,  $a=b \approx (a_{hex}+c_{hex})/2$  and  $c \approx 2\sqrt{3}a_{hex}$  [39].

The first rationale for the assignment of 3D islands to the tetragonal or orthorhombic phase is their compact rectangular shapes. Experiments have also shown that for the similar Er/Si (001) system where both nanowires and 3D islands are seen, the crystal structure of the islands is tetragonal [107]. Even though it has not been proved by any experimental techniques that Gd or Dy nanowires are of hexagonal  $AlB_2$  type structure, the anisotropic lattice mismatch to Si (001) surface explains well the nanowire formation mechanism [6, 7, 14]. Furthermore, the hexagonal structure can also explain the 0.35 nm height quantum of Dy silicide nanowires, which is the unit cell height (0.332 nm) along  $[1\bar{1}00]$  [14], as shown in (b). Similarly, the quantum height (0.35nm) for Gd silicide nanowires also agrees with this model, in which the unit cell height of Gd disilicide is 0.336 nm. Following this line of reasoning, the quantum height 0.66 nm of flat 3D islands can be explained by the tetragonal  $ThSi_2$  model, which is the total height (0.62 nm) of layers 3 and 4 in (c), including two layers of metal atoms inside.

Notice that in both models the top surface is shown as terminated with a Si bilayer, similar to the Si (001) termination of bulk silicon. This is analogy to the fact that RE silicides grown on Si (111) terminate with a buckled Si bilayer [69, 72]. If this is the case, the first layer of nanowires should consist of one layer of metal atoms (as discussed in

Section 3.4), and one Si bi-layer as a termination, as shown in (b). The apparent height of the nanowires of minimum height, 0.52 nm for Dy, and 0.49 nm for Gd, is larger than the measured quantum height of 0.35 nm. This is possibly caused by the different electronic states of the top surface of the nanowire, and the substrate which can be either clean Si (001)2×1, or either the 2×4 or the 2×7 reconstructions.

Note that the first layer of tetragonal phase in the 3D islands is drawn including two layers of metal atoms in (c) for convenience. The thickness may vary in the real situation as suggested by the measurements that no unique number can be found for the minimum height for the 3D islands. However, it is worthy to note that the distinction between the hexagonal and the other two silicide phases only arises when there is more than one layer of metal atoms present.

### ***6.3.3 Lattice mismatch and strain relaxation***

Apparently, the competition between nanowires and islands, or between the hexagonal phase and the tetragonal/orthorhombic phases, is a function of annealing duration and metal coverage, as well as the metal species since the coexistence of nanowires and islands is easier to realize for Dy silicides compared to Gd silicides. The hexagonal Gd silicide nanowires are more stable than Dy silicide nanowires, but islands do appear for Gd silicides at higher coverage and with longer annealing duration.

Essentially, the competition is controlled by the ease of epitaxial growth of each phase. As we know, lattice mismatch and chemical bonding at the interface are two factors to determine the realization of a heteroepitaxial system [108, 109, 122]. Due to the existence of lattice mismatch, a pair of superlattices with similar translational symmetry across the interface can be defined instead of a common superlattice (or

coincidence lattice) [108, 122]. The mismatch between the two superlattices and the unit cell area of the superlattices are two parameters that characterize the lattice match [88]. For RE silicide/Si (001) systems, the disilicides of different structures can form almost the same interface, implying similar chemical bonding configuration, as shown in Figure 6.11. Therefore, the lattice mismatch would be crucial for the epitaxial growth. As shown in Table 1.6, comparing the hexagonal to either the orthorhombic or the tetragonal silicide phases, a large uniaxial strain in the former can be redistributed over two axes in the latter. Unit cell area is a measure by which one can assess the effect of biaxial strain on epitaxial growth [88, 123]. We can use the ratio of the unit cell area of the tetragonal phase to the hexagonal phase as a measure of strain, and the percentage deviation from 1.0 as an areal mismatch (AM), where  $AM(tet/hex) = (area_{tet}/area_{hex} - 1)$ . Then  $AM(tet/hex)$  is 40% higher for Gd than Dy. Similarly,  $AM(orth/hex)$  is 50% higher for Gd than Dy. In both cases, this would support the tendency for Gd to be less likely to form non-hexagonal phases than Dy. If we consider the case of Er,  $AM(tet/hex)$  is very small which is consistent with the fact that small coverages of Er form at least as many 3D islands (tet) as nanowires (hex). In any case, the mismatch in unit cell area correctly predicts trends in the different behavior of different RE metals, even if it cannot be used to predict the details of the growth behavior for a particular system.

The presence of elongated 3D islands could also be related to strain relaxation. Firstly, we believe that these elongated islands are different from the nanowires in that they usually appear after annealing and are much wider and higher than nanowires. These islands could result from a shape transformation proposed by Tersoff and Tromp [124], where compact, symmetric islands are favored below a critical island size, while

elongated islands with high aspect ratios are the preferred shape for large islands. Thus the shape transformations taking place as a result of the system relaxing its strain may provide a convenient way of producing quasi-one-dimensional quantum-wire structures, without the necessity of an anisotropic lattice mismatch.

Sinusoidal undulated 3D islands could be of orthorhombic or hexagonal structure since a one dimensional undulation is more like to be related to anisotropic strain relaxation, and the measured quantized height 0.35 nm is the same as that of the nanowires, but different from that of the flat 3D islands. Similar phenomenon has been found in film growth and explained by variations in elastic strain energy and surface energy of the film related to lattice mismatch [110, 125-127].

Therefore, many phenomena apparent in the growth of RE silicides on Si (001) can be related to effect of strain relaxation. Based on the STM results, we can do little more than enumerate the different growth morphologies that can occur. The detailed connection between strain and the growth behavior, as well as the assignment of nanowires and the 3D islands to different silicide phases, awaits confirmation from other analytical techniques.

It is illuminating to draw an analogy to the extensive literature on the growth of Ge on Si (001). This is a system that is in principle easier to understand than the RE silicide /Si (001) system since the growth is pseudomorphic, with a mismatch (4%) that is similar to that between tetragonal RE silicides and silicon [128, 129]. Nevertheless, the behavior of this system is very complex, with three different forms of islands formed (hut clusters, pyramids, and domes), and it is only after many years of effort that a basic understanding of the growth in terms of strain relaxation has been achieved.

## 6.4 Conclusions

The growth of Dy, Gd silicide nanostructures is a function of growth temperature, annealing duration, and metal coverage. At temperatures lower than 600°C, metal accommodation in 2D reconstructions is preferable, and at higher temperatures, metal is lost from the surface. Longer annealing duration promotes the formation of 3D islands. The proportions of 2D reconstructions, nanowires and 3D islands in the surface are also related to metal coverage. The Gd is accommodated in 2D phases up to a critical coverage, 0.357 ML, and then nanowires start to nucleate. 3D islands form for both Gd and Dy at higher coverage. Gd grows nanowires without 3D islands over a wider range of conditions than Dy. The differences in behavior between the metals can be correlated with the areal mismatch of the surface lattice unit cells which is a measure of biaxial strain. Both the nanowires and islands grow layer-by-layer with quantized step heights which are consistent with the bulk RE silicide crystallographic structures by assigning nanowires to the hexagonal phase, and 3D islands to the orthorhombic or tetragonal phases. The RE silicide growth on the vicinal Si substrate shows similar kinetics as on the normal Si substrate. In order to grow a single domain, parallel arrays of nanowires on the vicinal surface, it is crucial to suppress the growth of 3D islands which are accompanied by significant Si redistribution and step redistribution.



## **Chapter 7 Future work**

As discussed in the introduction, the idea of using anisotropic lattice mismatch systems to produce nanowires was just realized two years ago, and it seems that RE silicides/Si (001) are the only systems under study. Generally, people are more familiar with biaxially lattice mismatched systems, and most of the knowledge comes from the extensive and intensive studies of heteroepitaxial growth of semiconductor thin films and quantum dots. Essentially, most of the phenomena during heteroepitaxial growth can be related to strain relaxation in these systems, which originates from the biaxial lattice mismatch. In this chapter, a brief review is given of the effect of lattice mismatch and strain relaxation on epitaxy, and some possible nanowire forming systems are pointed out. More research work is needed to better understand the strain related effects in the growth of RE silicides, and to find other systems in which uniaxial strain results in the formation of nanowires.

### **7.1 Epitaxy**

Epitaxial growth is a key process in modern microelectronics technology and has been studied extensively and intensely to pursue new classes of artificially structured materials to produce novel devices [109, 130, 131].

The term epitaxy is derived from the Greek words epi (meaning "on") and taxis (meaning "arrangement") [132]. The epitaxial growth refers to the deposition of a thin layer of material onto the surface of a single crystal substrate in such a manner that the layer is also a single crystal and has a fixed and predetermined crystal orientation with respect to the substrate. If the material grown is the same as the substrate such as silicon

on silicon, then it has the same crystal orientation as that of substrate. This type of epitaxy growth is called homoepitaxy. If the materials are different, such as Ge on Si, this is called heteroepitaxy. Obviously, the growth of silicides on silicon substrates belongs to the second case.

It is generally accepted that the epitaxial growth proceeds by three growth modes at thermodynamic equilibrium: layer-by-layer [Frank-van der Merwe (FM)], island [Volmer-Weber (VW)], and layer-by-layer growth followed by 3D islands [Stranski-Krastanov (SK)] growth modes [129, 130, 133, 134].

In the lattice matched systems, the growth mode is governed by the interface and surface energies only. If the sum of the surface free energy of the epitaxial film and the free energy of the film/substrate interface is smaller than the surface free energy of the substrate, layer-by-layer mode occurs. The opposite case results in island growth mode. In the intermediate case, Stranski–Krastanov mode occurs. The situation is further complicated if lattice mismatch is present between film and substrate. Figure 7.5 is an equilibrium phase diagram of a lattice-mismatched heteroepitaxial system [135], showing that the FM mode only occurs at small lattice mismatch (up to 10%), but at large lattice mismatch, SK mode and VW mode are favored. Transition from FM mode to SK mode could happen at a certain thickness for a given mismatch due to the increasing strain energy with thickness during growth.

In practice, epitaxial growth (or deposition) is a non-equilibrium process determined by kinetic phenomena, growth morphologies will deviate more or less from the thermodynamic picture [130, 134]. The growth mode strongly depends on the detailed growth conditions, and also on the combination of film and substrate. For semiconductor

heteroepitaxy, for example, GeSi/Si [136] and InGaAS/GaAs [137, 138], three dimensional island growth is favored over the layer-by-layer growth mode when the lattice mismatch is larger than 2% [111].

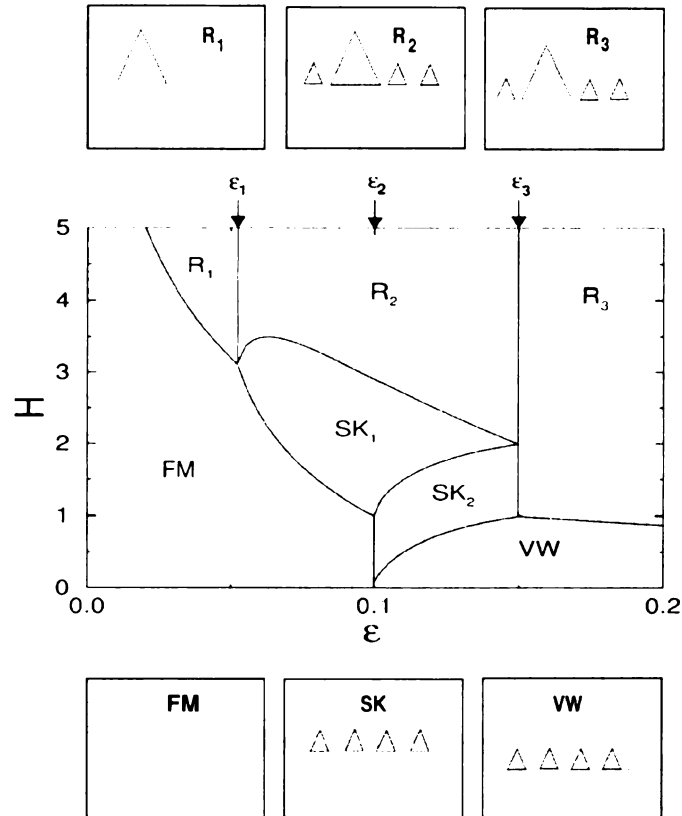


Figure 7.1 Equilibrium phase diagram in function of the coverage  $H$  and misfit  $\epsilon$ . The small panels on the top and the bottom illustrate the morphology of the surface.

## 7.2 Lattice Mismatch

As we can see, lattice mismatch plays a central role in determining the final overlayer morphology. A brief discussion on lattice mismatch would be helpful in finding new systems to form nanowires.

Zur and McGill [88] suggested a criterion for lattice match in the heteroepitaxial system that the interface translational symmetry could be compatible with the symmetry on both sides of the interface within a given precision. A pair of superlattices with similar translational symmetry across the interface can be defined instead of a common superlattice (or coincidence lattice) [108, 122] due to the existence of mismatch. The mismatch between the two superlattices and the unit cell area of these superlattices are two parameters that characterize the lattice match. Following this criterion, a number of ways can be defined to match the two lattices, but actual orientation will be determined by the chemical bonding at the interface [109]. The simplest case for heteroepitaxy is that the overlayer and substrate have similar matching lattices and similar lattice parameters (mismatch <10%), then the matching between the two cubic lattices can be described in Figure 7.2(a). In this case, the mismatch can be defined as  $f = (a_0 - a_s) / a_s$  (note that this is only one type of definition commonly in use). For high mismatch systems (>10%), a coincidence lattice can be defined with lattice parameter  $na_0$  or  $ma_s$ , as shown in Figure 7.2(b), where  $m/n$  is the closest integer ratio of  $a_0 / a_s$ . In this case, the mismatch is defined as  $f = (na_0 - ma_s) / ma_s$  [108, 122]. Sometimes, a rotation between the two lattices is involved to match them together, as shown in Figure 7.2(c). Obviously, the lattice matching between hexagonal RE disilicide (0110) and Si (001) substrate belong to the first case. And that between cubic  $\text{CaF}_2$  (110) with Si (001) belong to the second case since it has a 45% mismatch along one direction, which amounts to -4.64% if we use the mismatch definition for coincidence lattice.

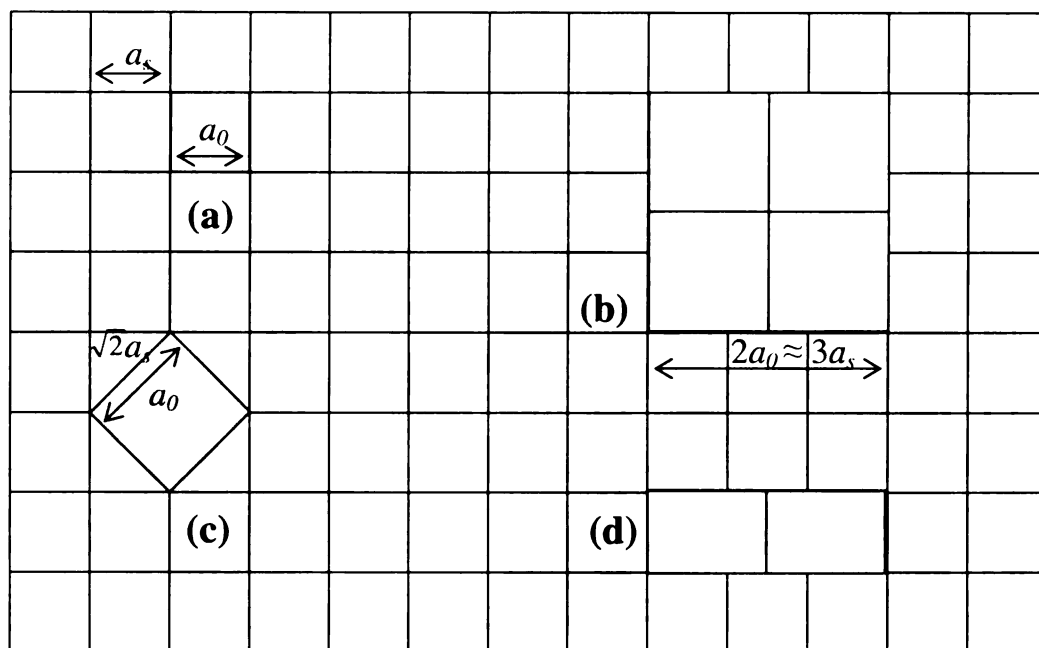


Figure 7.2 Lattice matching in heteroepitaxial systems, where  $a_s$  denotes substrate lattice parameter, and  $a_0$  denotes the overlayer lattice parameter. The overlayer lattice is the shaded area.

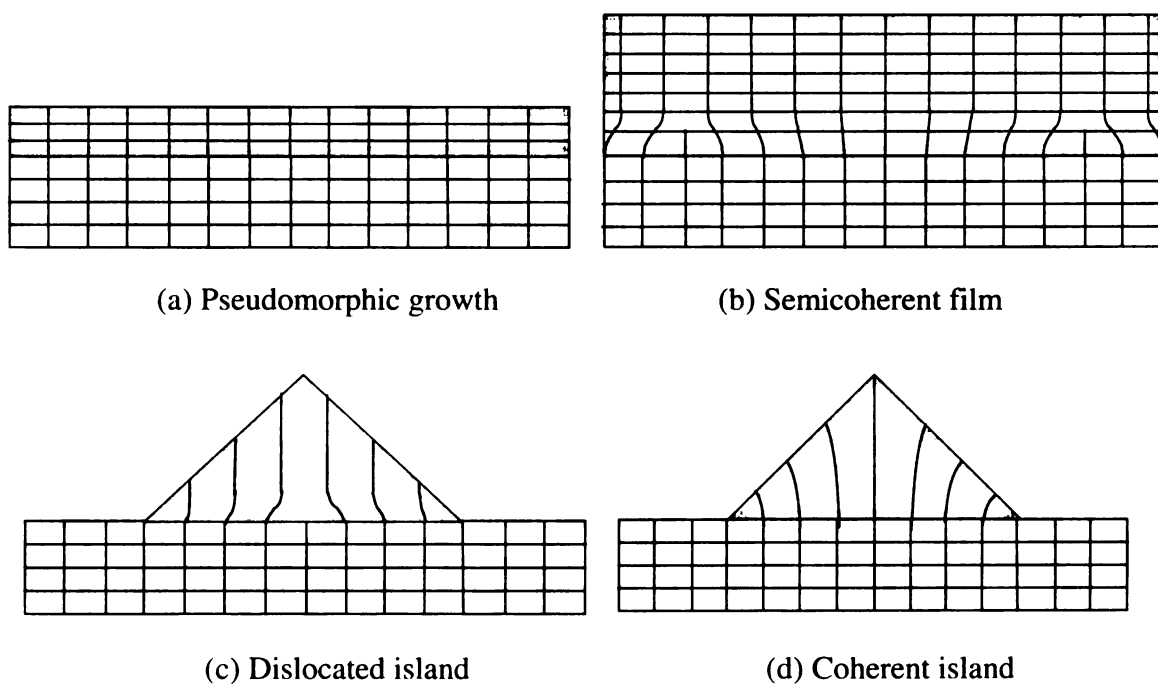


Figure 7.3 Registry between overlayer and substrate.

### 7.3 Strain relaxation

In the early stages of epitaxial growth, the overlayer will strain elastically to match the substrate lattice coherently at the interface as a wetting layer, which is usually called “pseudomorphic” growth [139], as shown in Figure 7.3(a). Up to a critical thickness, strain built up during growth will be relieved by forming misfit dislocations in the interface, resulting in a semicoherent film [108, 140, 141], as shown in (b), or by a transition from the layer-by-layer growth mode to SK mode by forming islands on top of the wetting layer [142]. The islands could be unstrained with dislocation at the interface [143, 144], which is called ‘dislocated islands’, as shown in (c), or could be strained elastically to keep in registry with wetting layer lattice, which is called ‘coherent islands’ [129, 134], as shown in (d). It is generally stated that the islands formed in the VW system are incoherent or dislocated [143]. Only recently, it was reported that coherent islands can be formed in Gd/Si (111) system which proceed by VW growth mode [145].

Misfit dislocation is just one way for strain relaxation. The strain caused by lattice mismatch can also be relieved by surface roughening and other defects resulting from the interaction between misfit dislocation and surface roughening during heteroepitaxial growth [110, 131, 146]. All of these mechanisms are closely related to the growth modes, determining the final morphologies [111, 146]. For systems with small mismatch ( $<2\%$ ), growth proceeds by layer-by-layer mode and ‘cross-hatch’ morphology usually forms [111, 147]. For systems with larger mismatch, growth proceeds by coherent or incoherent islanding (SK or VW mode), resulting in a series of strain-relief morphologies [110]. Theory and experiments show that systems with tensile strain could be more resistant to roughening [133, 148, 149].

Strain-induced roughening can be problematic in the fabrication of coherently strained device structures, but on the other hand, it is beneficial for the fabrication of quantum dots [150], for example, GeSi quantum dots on Si (001) [128, 129, 151, 152] and InGaAs quantum dots on GaAs [153, 154]. The quantum dots could form ordering arrays spontaneously, called self-organization, driven by long-range elastic interaction [129, 134, 155].

The formation of quantum dots generally involves two square lattices which are highly mismatched biaxially, thus the growth is limited along the two matching crystallographic axes, forming square-shaped islands. There are circumstances that the symmetry is broken then islands grow into elongated shapes, forming wire-like structure. For example, the formation of Ge ‘hut’ shaped islands on Si (001) is due to surface energy anisotropy [128, 156], and the formation of InAs/InP (001) quantum wires results from anisotropic stress relaxation [157]. In these two cases, the geometric symmetry is still reserved. If the geometric symmetry is destroyed, anisotropic strain will result, leading to the formation of nanowires. There are two ways to break the geometric symmetry, using low symmetry substrate, such as Ge nanowires on Si (113) [158], and using low symmetry overlayer, such as CaF<sub>2</sub> nanowires on Si (001) [159, 160]. Obviously, the formation of RE disilicide nanowires on Si (001) under investigation belongs to the latter case.

#### **7.4 Possible systems to form nanowires**

Out of scientific curiosity and technological interest, it is desirable to seek if there are other substrate/overlayer combinations that have anisotropic mismatch and might form

nanowires of metals, insulators, and semiconductors. For nanowire forming RE silicide/Si (001) systems, the mismatches range between  $-1.09\%$  and  $0.96\%$  along the good match direction, and between  $6.5\%$  and  $8.6\%$  along the poor match direction ( $-4.58\%$  for  $\text{ScSi}_2/\text{Si}$  (001)). We can conclude here that a system might be used to form nanowires if the mismatch between the two lattices fall in a similar range as the RE silicide/Si (001) systems. One interesting system that would be a straightforward extension of the present work is RE silicide/SiGe (001). As mentioned above, we can manipulate the lattice parameters of SiGe alloy by changing the ratio between Si and Ge, hence it is possible to make zero mismatch along the good match direction, but keep the mismatch along the poor match direction still within the required range, for example,  $\text{GdSi}_2/\text{Si}_{0.75}\text{Ge}_{0.25}$  ( $0\%$ ,  $7.61\%$ ), in which it is possible to manipulate the width and length of the nanowires which are regulated by the according mismatch. This system can also be used to manipulate the mismatch anisotropy to test the lattice mismatch model.

Our understanding on nanowire formation with systems of anisotropic superlattice mismatch is very limited since we only have one example of  $\text{CaF}_2/\text{Si}$  (001). The  $\text{CaF}_2$  is of face-centered cubic structure, having a lattice parameter  $5.463\text{\AA}$ .  $\text{CaF}_2$  matches onto Si (001) surface with  $\text{CaF}_2$  (110) // Si (001) and  $\text{CaF}_2$  [110] parallel to one of the Si<110> directions on Si surface, as shown in Figure 7.3(d). The mismatch is  $0.6\%$  along the longitudinal direction, and  $-4.64\%$  along the lateral direction of the nanowire. The  $\text{CaF}_2$  nanowire is about 5-10 nm wide, and typically  $1\mu\text{m}$  long [159]. There are a number of systems which have similar anisotropy as  $\text{CaF}_2$  (110) // Si (001), as shown in Table 7.1, which are possible to form nanowires. All of the metal silicides listed in the table belong to the category of refractory metal (RM) silicides, as shown in Table 1.2.



It is also possible to use lower symmetry substrates, such as Si (110) to form nanowires. For example, if tetragonal  $\text{GdSi}_2$  (001) can match onto the Si (110) surface with  $\text{GdSi}_2$  [100] // Si [001], then we have anisotropic mismatches of 0.68% along one direction and 6.77% along the other direction. Therefore, nanowires could be formed with this system.

## **7.5 Future work**

### ***7.5.1 Growth of nanowires with other systems***

As we can see, following the anisotropic lattice mismatch model, it is possible to find new systems to form nanowires, such as the refractory metal (Nb, Ta, Mo and W) silicides mentioned above, and other systems on lower symmetry substrates, such as  $\text{GdSi}_2/\text{Si}$  (110). Although it is easy to form nanowires with RE/Si (001) systems, it is not the best system due to their low thermal stability and high reactivity with oxygen. In contrary, RM silicides are very stable against heating and oxygen [19]. Therefore, the nanowires formed by RM silicides would be a good alternative to RE disilicide nanowires. Although the transition metal silicides have been studied extensively, the formation of nanowires is not observed possibly because attention has been concentrated on continuous films, and the early stages of growth are not very fully studied. Similar to RE/Si systems, RM/Si systems have rich phase diagrams with a variety of stoichiometries (see Table 1.2). Growth conditions need to be manipulated to produce the correct phase that might potentially form nanowires.

Table 7.1 Lattice matching of some RE disilicides with Si (001) [44]

Matching planes	Epitaxial orientation	Silicide superlattice		Silicon superlattice		mismatches	
		a (Å)	b (Å)	a (Å)	b (Å)	%a	%b
(1 $\bar{1}$ 00) NbSi <sub>2</sub> //(001)Si	$[\bar{1} \bar{1} 23]$ NbSi <sub>2</sub> // $[\bar{1} \bar{1} 0]$ Si $[22\bar{4}3]$ NbSi <sub>2</sub> // $[\bar{1} \bar{1} 0]$ Si	8.15	11.64	7.68	11.51	6.12	1.13
TaSi <sub>2</sub> ( $\bar{1} \bar{2} \bar{1} 4$ )//(001)Si	TaSi <sub>2</sub> $[\bar{1} 0 10]$ //Si $[110]$ TaSi <sub>2</sub> $[2\bar{4}23]$ //Si $[\bar{1} 10]$	8.28	11.60	7.68	11.52	7.81	0.69
(0001)MoSi <sub>2</sub> //(001)Si	$[2 \bar{1} \bar{1} 0]$ // $[\bar{1} \bar{1} 0]$	7.99	23.07	7.68	23.04	4.04	0.13
(0001)WSi <sub>2</sub> //(001)Si	$[2 \bar{1} \bar{1} 0]$ // $[\bar{1} \bar{1} 0]$	7.99	23.04	7.68	23.04	4.04	0.13

### **7.5.2 Strain relaxation in RE silicide/Si (001) systems**

As discussed above, strain relaxation plays an important role in heteroepitaxial growth. Generally, the heteroepitaxy of GeSi alloy on Si has been studied as a model system for strain relaxation due to its technological importance, simplicity, and the fact that the lattice mismatch can be tuned by changing the ratio between Ge and Si in the film [128, 129]. The growth of RE silicides on Si (001) would also be a good system for studying strain effect on heteroepitaxial growth since they form the same crystal structures and the lattice mismatch varies from metal to metal. Most interestingly, the mismatch could be biaxial or uniaxial, depending on the detailed silicide structure, which provides new insight into the heteroepitaxy. Unfortunately, this issue is left unstudied for  $\text{RESi}_2/\text{Si}$  (001) system for several reasons. Firstly, additional complications have to be considered due to the difference in chemical properties between different RE metals, such as valency and chemical bonding, compared to Ge/Si system. Secondly, attention is focused on improvement of surface morphology and properties of  $\text{RESi}_2/\text{Si}$  interfaces. And most probably, the RE silicides have not been widely used in the semiconductor industry.

In our experiments, many interesting phenomena have been found in the early stages of RE (Dy, Gd, and Er) silicide growth on Si (001), e.g., transformation between  $2\times 4$  and  $2\times 7$  superstructures, nanowire bundling, wavy islands, elongated islands, all of which can be related to strain relaxation effect. More experimental and theoretical work need to be done to understand these phenomena. A good understanding of these strain related issues in the RE silicide/Si (001) systems will not only contribute to the growth of low dimensional materials, but also contribute to the theory of heteroepitaxy.

Another important issue is the difference in growth behavior of different RE metals, which could be controlled by strain relaxation due to different lattice mismatch in different systems. As an example, the  $\text{ScSi}_2/\text{Si}$  (001) system is worthy to try since Sc silicide has negative mismatch (tensile strained) along the poor mismatch direction ( $[10\bar{1}0]$ ), opposite to that of Dy and Gd silicides which are compressive strained on Si (001). As we know, the relaxation of compressive and tensile strained systems is different. Therefore, it would be interesting to see what differences we can observe in the growth of Sc silicide on Si (001).

### 7.5.3 TEM work

In this thesis, we have made different plausibility arguments for the assignment of the hexagonal silicide phase to nanowires, and tetragonal or orthorhombic phase to large 3D islands. Transmission electron microscopy (TEM) is needed to examine these structures individually to test these assignments. Convergent beam diffraction has to be used since most of the structures are very small.

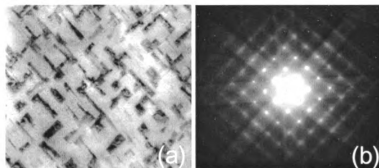


Figure 7.4 (a) Bright field image ( $1\mu\text{m}\times 0.9\mu\text{m}$ ) of a Dy/Si (001) sample at a metal coverage of 3.4 ML. (b) The diffraction pattern from the same sample.

We have done a preliminary TEM study of the Dy/Si (001) surface. The sample was prepared by gluing a Mo ring on the film side of 3.4 ML Dy deposited sample, then

gluing the Mo ring to a sapphire and thinning the sample from back side to 10  $\mu\text{m}$  by mechanical polishing and ion milling. H-800 TEM was used for observation. Plan view bright field TEM images of  $\text{DySi}_{1.7}$  islands show diffraction/scattering contrast. The morphology is the same as that seen by STM on the same sample, indicating that the wires are stable after exposure to air. The lack of extra spots in the diffraction pattern from the overlayer, along with the absence of Moire fringes in the images, indicate that the islands are coherent with the substrate, at least in the direction along the long axis of the elongated islands.

STM measurements shown in Chapter 4, Table 4.1 show that the top surface of islands is relaxed to a certain degree with a dependence on thickness. The best explanation would be that the islands grow coherently with the substrate at the interface, but relaxed at the top, matching the model shown in Figure 7.3(c). Further experiments with cross sectional TEM observation is also needed to characterize the interface structure between islands (or nanowires) and Si substrate.

## APPENDIX

### List of Publications

1. Liu, B.Z. and J. Nogami, *An STM study of Cu on Si(001) in the  $c(8\times 8)$  structure*. Surf. Sci., 2000. **453**: p. 173.
2. Liu, B.Z. and J. Nogami, *An STM study of the Si(001)( $2\times 4$ )-Dy surface*. Surf. Sci., 2001. **488**: p. 399-405.
3. Nogami, J., B.Z. Liu, M.V. Katkov, C. Ohbuchi, and N.O. Birge, *Self-assembled rare-earth silicide nanowires on Si (001)*. Phys. Rev. B, 2001. **63**: p. 233305.
4. Liu, B.Z. and J. Nogami, *An STM study of Dysprosium silicide nanowire growth on Si (001)*. J. Appl. Phys., 2003. **93**(1): p. 593.
5. Liu, B.Z. and J. Nogami, *Growth of parallel rare earth silicide nanowire arrays on vicinal Si(001)*. in preparation.
6. Liu, B.Z. and J. Nogami, *An STM study of the Si(001)( $2\times 7$ )-Gd, Dy surface*. in preparation.
7. Liu, B.Z. and J. Nogami, *A comparison of Dy and Gd silicide nanowire growth*. in preparation.

## REFERENCES

1. Baglin, J.E., F.M. d'Heurle, and C.S. Petersson, *The formation of silicides from thin films of some rare-earth metals*. Appl. Phys. Lett., 1980. **36**(7): p. 594.
2. Tu, K.N., R.D. Thompson, and B.Y. Tsaur, *Low Schottky barrier of rare-earth silicide on n-Si*. Appl. Phys. Lett., 1981. **38**(8): p. 626.
3. Knapp, J.A. and S.T. Picraux, *Epitaxial growth of rare-earth silicides on (111) Si*. Appl. Phys. Lett., 1986. **48**(7): p. 466.
4. Preinesberger, C., S. Vandr , T. Kalka, and M. D hne-Prietsch, *Formation of dysprosium silicide wires on Si (001)*. J. Phys. D: Appl. Phys., 1998. **31**: p. L43.
5. Markoff, J., *Computer scientists are poised for revolution on a tiny scale*, in *The New York Times*. November 1, 1999.
6. Chen, Y., D.A.A. Ohlberg, G. Medeiros-Ribeiro, Y.A. Chang, and R.S. Williams, *Self-assembled growth of epitaxial erbium disilicide nanowires on silicon (001)*. Appl. Phys. Lett., 2000. **76**(26): p. 4004.
7. Nogami, J., B.Z. Liu, M.V. Katkov, C. Ohbuchi, and N.O. Birge, *Self-assembled rare-earth silicide nanowires on Si (001)*. Phys. Rev. B, 2001. **63**: p. 233305.
8. Katkov, M. and J. Nogami, *Y growth on Si(001)*. Bull. Am. Phys. Soc., March meeting, 2002, 2002. **47**(1): p. 283.
9. Liu, B.Z. and J. Nogami, *Optimizing the growth of rare-earth silicide nanowires on Si(001)*. Bull. Am. Phys. Soc., March meeting, 2002, 2002. **47**(1): p. 169.
10. Chen, Y., D.A.A. Ohlberg, and R.S. Williams, *Nanowires of four epitaxial hexagonal silicides grown on Si(001)*. J. Appl. Phys., 2002. **91**(5): p. 3213.
11. Chen, Y., D.A.A. Ohlberg, and R.S. Williams, *Epitaxial growth of erbium silicide nanowires on silicon(001)*. Mater. Sci. Eng. B, 2001. **87**: p. 222-226.

12. Preinesberger, C., S.K. Becker, S. Vandr , T. Kalka, and M. D hne-Prietsch, *Structure of DySi<sub>2</sub> nanowires on Si(001)*. J. Appl. Phys., 2002. **91**(3): p. 1695.
13. Liu, B.Z. and J. Nogami, *An STM study of the Si(001)(2 4)-Dy surface*. Surf. Sci., 2001. **488**: p. 399-405.
14. Liu, B.Z. and J. Nogami, *An STM study of Dysprosium silicide nanowire growth on Si (001)*. J. Appl. Phys., 2003. **93**(1): p. 593.
15. Liu, B.Z. and J. Nogami, *Growth of parallel rare earth silicide nanowire arrays on vicinal Si(001)*. in preparation.
16. Liu, B.Z. and J. Nogami, *An STM study of the Si(001)(2 7)-Gd, Dy surface*. in preparation.
17. Liu, B.Z. and J. Nogami, *A comparison of Dy and Gd silicide nanowire growth*. J. Appl. Phys., in preparation.
18. <http://public.itrs.net/>, *International Technology Roadmap for Semiconductors (2001)*.
19. Murarka, S.P., *Silicides for VLSI Applications*. 1983, New York: Academic Press, Inc.
20. Maex, K., M. Van.Rossum, and A. Reader, *Crystal structure of TM silicides*, in *Properties of Metal Silicides*, K. Maex and M. Van.Rossum, Editors. 1995, INSPEC: London. United Kingdom. p. 3.
21. Xu, Z., *Basic physical properties of RE silicides*, in *Properties of Metal Silicides*, K. Maex and M.V. Rossum, Editors. 1995, INSPEC: London. United Kingdom. p. 45.
22. Reader, A.H., A.H. van.Ommen, P.J.W. Weijs, R.A.M. Wolters, and D.J. Oostra, *Transition metal silicides in silicon technology*. Rep. Prog. Phys., 1992. **56**: p. 1397-1467.



23. Thompson, R.D. and K.N. Tu, *Comparison of the three classes (rare earth, refractory and near-noble) of silicide contacts*. Thin Solid Films, 1982. **93**: p. 265-274.
24. Thompson, R.D., B.Y. Tsaur, and K.N. Tu, *Contact reaction between Si and rare earth metals*. Appl. Phys. Lett., 1981. **38**(7): p. 535.
25. Gambino, J.P. and E.G. Colgan, *Silicides and ohmic contacts*. Materials Chemistry and Physics, 1998. **52**: p. 99-146.
26. Netzer, F.P., *Rare earth overlayers on silicon*. J. Phys.: Condens. Matter, 1995. **7**: p. 991.
27. Hedrick, J.B., *Rare Earths*. The American Ceramic Society Bulletin, 2000. **79**(8): p. 74.
28. Xu, Z., *Schottky barrier heights of RE silicides on Si*, in *Properties of Metal Silicides*, K. Maex and M.V. Rossum, Editors. 1995, INSPEC: London, United Kingdom. p. 169.
29. Derrien, J., *Schottky barrier heights of TM silicides on Si and GaAs*, in *Properties of Metal Silicides*, K. Maex and M.V. Rossum, Editors. 1995, INSPEC: London. United Kingdom. p. 164.
30. Baglin, J.E.E., F.M. d'Heurle, and C.S. Petersson, *Diffusion marker experiments with rare-earth silicides and germanides: Relative mobilities of the two atom species*. J. Appl. Phys., 1981. **52**(4): p. 2841-2846.
31. Anderson, R., J. Baglin, J. Dempsey, W. Hammer, F. d'Heurle, and C.S. Petersson, *Nucleation-controlled thin-film interactions-some silicides*. Appl. Phys. Lett., 1979. **35**(3): p. 285-287.
32. d'Heurle, F.M. and P. Gas, *Kinetics of formation of silicides: A review*. J. Mater. Res., 1986. **1**(1): p. 205.
33. Houssay, E., A. Rouault, O. Thomas, R. Madar, and J.P. Senateur, *Metallurgical reinvestigation of rare earth silicides*. Appl. Surf. Sci., 1989. **38**: p. 156-161.

34. Travlos, A., P. Aloupogiannis, E. Rokofyllou, and C. Papastaikoudis, *Growth, characterization and electrical properties of gadolinium silicide thin layers*. Philos. Mag. B, 1993. **67**(4): p. 485-495.
35. Perri, J., I. Binder, and B. Post, *Rare earth metal "disilicides"*. J. Phys. Chem., 1959. **63**: p. 616.
36. Frangis, N., G. Van.Tendeloo, J.V. Landuyt, P. Muret, and T.T.A. Nguyen, *Structural characterization of erbium silicide thin films on an Si(111) substrate*. J. Alloys and compounds, 1996. **234**: p. 244-250.
37. Siegal, M.P., F.H. Kaatz, W.R. Graham, J.J. Santiago, and J. VanderSpiegel, *Formation Of Epitaxial Yttrium and Erbium Silicide On Si(111) in Ultrahigh-Vacuum*. Appl. Surf. Sci., 1989. **38**: p. 162.
38. Knapp, J.A., S.T. Picraux, C.S. Wu, and S.S. Lau, *Kinetics and morphology of erbium silicide formation*. J. Appl. Phys., 1985. **58**(10): p. 3747.
39. Frangis, N., J. Van.Landuyt, G. Kaltsas, A. Travlos, and A.G. Nassiopoulou, *Growth of erbium-silicide films on (100) silicon as characterised by electron microscopy and diffusion*. J. Cryst. Growth, 1997. **172**: p. 175-182.
40. Xu, Z., *Epitaxial growth of RE silicides*, in *Properties of Metal Silicides*, K. Maex and M.V. Rossum, Editors. 1995, INSPEC: London, United Kingdom. p. 78.
41. Thomas, O., C.S. Petersson, and F.M. d'Heurle, *The Reaction of Scandium Thin-Films with Silicon-diffusion, Nucleation, Resistivities*. Appl. Surf. Sci., 1991. **53**: p. 138-146.
42. Vantomme, A., M.F. Wu, S. Hogg, U. Wahl, W. Deweerdt, H. Pattyn, G. Langouche, S. Jin, and H. Bender, *Stabilisation and phase transformation of hexagonal rare-earth silicides on Si (111)*. Nucl. Instrum. Methods in Phys. Res. B, 1999. **147**: p. 261-266.
43. Clevenger, L.A. and R.W. Mann, *Formation of epitaxial TM silicides*, in *Properties of Metal Silicides*, K. Maex and M.V. Rossum, Editors. 1995, INSPEC: London, United Kingdom. p. 61.

44. Chen, L.J. and K.N. Tu, *Epitaxial-growth of Transition-metal Silicides on Silicon*. Mater. Sci. Rep., 1991. **6**(2-3): p. 53-140.
45. Tung, R.T. and S. Ohmi, *Epitaxial silicide interfaces in microelectronics*. Thin Solid Films, 2000. **369**: p. 233-239.
46. Mantl, S. and H.L. Bay, *New method for epitaxial heterostructure layer growth*. Appl. Phys. Lett., 1992. **61**(3): p. 267.
47. Hensel, J.C., A.F.J. Levi, R.T. Tung, and J.M. Gibson, *Transistor Action In Si/CoSi<sub>2</sub>/Si Heterostructures*. Appl. Phys. Lett., 1985. **47**: p. 151.
48. Tung, R.T., *Epitaxial CoSi<sub>2</sub> And NiSi<sub>2</sub> Thin-Films*. Mater. Chem. Phys., 1992. **32**((2)): p. 107-133.
49. Tung, R.T., J.M. Poate, J.C. Bean, J.M. Gibson, and D.C. Jacobson, *Epitaxial Silicides*. Thin Solid Films, 1982. **93**((1-2)): p. 77-90.
50. Yu, B.D., Y. Miyamoto, O. Sugino, A. Sakai, T. Sasaki, and T. Ohno, *Structural and Electronic Properties of Metal-Silicide/Silicon Interfaces: A First-Principles Study*. J. Vac. Sci. Technol. B, 2001. **19**(4): p. 1180-1185.
51. Xu, Z., *Thin film formation of RE silicides*, in *Properties of Metal Silicides*, K. Maex and M.V. Rossum, Editors. 1995, INSPEC: London, United Kingdom. p. 73.
52. Lau, S.S., C.S. Pai, C.S. Wu, T.F. Kuech, and B.X. Liu, *Surface-Morphology Of Erbium Silicide*. Appl. Phys. Lett., 1982. **41**: p. 77.
53. Wu, C.S., S.S. Lau, T.F. Kuech, and B.X. Liu, *Surface-Morphology and Electronic-Properties of ErSi<sub>2</sub>*. Thin Solid Films, 1983. **104**: p. 175.
54. Polop, C., C. Rogero, J.L. Sacedón, and J.A. Martín-Gago, *Surface morphology of yttrium silicides epitaxially grown on Si(111) by STM*. Surf. Sci., 2001. **482-485**: p. 1337-1342.

55. Vandr , S., T. Kalka, C. Preinesberger, and M. D hne-Prietsch, *Epitaxial growth and electronic structure of lanthanide silicides on n-type Si(111)*. J. Vac. Sci. Technol. B, 1999. **17**(4): p. 1682.
56. Shen, G.H., J.C. Chen, C.H. Lou, S.L. Cheng, and L.J. Chen, *The growth of pinhole-free epitaxial DySi<sub>2-x</sub> films on atomically clean Si(111)*. J. Appl. Phys., 1998. **84**(7): p. 3630.
57. Kaltsas, G., A. Travlos, A.G. Nassiopoulos, N. Frangis, and J. Van.Landuyt, *High crystalline quality erbium silicide films on (100) silicon, grown in high vacuum*. Appl. Surf. Sci., 1996. **102**: p. 151-155.
58. Siegal, M.P., W.R. Graham, and J.J. Santiago-Aviles, *Growth of pinhole-free epitaxial yttrium silicide on Si(111)*. J. Appl. Phys., 1990. **68**(2): p. 574.
59. Bennett, P.A. and H. vonK nel, *Scanning tunneling microscopy studies of silicides*. J. Phys. D: Appl. Phys., 1999. **32**: p. R71.
60. Hsu, C.C., Y.X. Wang, J. Hu, J. Ho, and J.J. Qian, *The effect of thermal treatment on the thin-film reaction of La, Ce, and Nd on silicon surfaces*. J. Vac. Sci. Technol. A, 1989. **7**(5): p. 3016.
61. Travlos, A., N. Salamouras, and N. Boukos, *Epitaxial dysprosium silicide films on silicon: growth, structure and electrical properties*. Thin Solid Films, 2001. **397**: p. 138-142.
62. Kaatz, F.H., W.R. Graham, and J. VanderSpiegel, *Modification of the microstructure in epitaxial erbium silicide*. Appl. Phys. Lett., 1993. **62**(15): p. 1748.
63. Shen, G.H., J.C. Chen, and L.J. Chen, *The structures and variation of vacancy ordering in epitaxial DySi<sub>2-x</sub> thin films on (111)Si*. Appl. Surf. Sci., 1999. **142**: p. 300-304.
64. Luo, C.H., G.H. Shen, and L.J. Chen, *Vacancy ordering structures in epitaxial RESi<sub>2-x</sub> thin films on (111)Si and (001)Si*. Appl. Surf. Sci., 1997. **113/114**: p. 457.
65. Gurvitch, M., A.F.J. Levi, R.T. Tung, and N. S., *Epitaxial yttrium silicide on (111) silicon by vacuum annealing*. Appl. Phys. Lett., 1987. **51**(5): p. 311.

66. Travlos, A., N. Salamouras, and N. Boukos, *Growth, structure and electrical properties of epitaxial thulium silicide thin films on silicon*. J. Appl. Phys., 1997. **81**(3): p. 1217.
67. Molnár, G.L., G. Petö, E. Zsoldos, N.Q. Khánh, and Z.E. Horváth, *Amorphous alloy formation and thickness dependent growth of Gd-silicide in solid phase thin film reaction*. Thin Solid Films, 1998. **317**: p. 417-420.
68. Molnár, G., I. Geröcs, G. Petö, E. Zsoldos, E. Jároli, and J. Gyulai, *Thickness-dependent formation of Gd-silicide compounds*. J. Appl. Phys., 1988. **64**(12): p. 6746.
69. Wetzel, P., S. Saintenoy, C. Pirri, D. Bolmont, G. Gewinner, T.P. Roge, F. Palmino, C. Savall, and J.C. Labrune, *STM investigation of 2- and 3-dimensional Er disilicide grown epitaxially on Si(111)*. Surf. Sci., 1996. **355**: p. 13-20.
70. Roge, T.P., F. Palmino, C. Savall, J.C. Labrune, S. Saintenoy, P. Wetzel, C. Pirri, D. Bolmont, and G. Gewinner, *Initial growth mode of Er silicide on Si(111) by solid phase epitaxy*. Surf. Sci., 1996. **352-354**: p. 622-627.
71. d'Avitaya, F.A., A. Perio, J.-C. Oberlin, Y. Campidelli, and J.A. Chroboczek, *Fabrication and structure of epitaxial Er silicide films on (111) Si*. Appl. Phys. Lett., 1989. **54**(22): p. 2198.
72. Wetzel, P., S. Saintenoy, C. Pirri, D. Bolmont, and G. Gewinner, *Surface states and reconstruction of epitaxial root 3× root 3R30 Er silicide on Si(111)*. Phys. Rev. B, 1994. **50**(15): p. 10886.
73. Lohmeier, M., W.J. Huisman, G.t. Horst, P.M. Zagwijn, E. Vlieg, C.L. Nicklin, and T.S. Turner, *Atomic structure and thermal stability of two-dimensional Er silicide on Si(111)*. Phys. Rev. B, 1996. **54**: p. 2004.
74. Spence, D.J., S.P. Tear, T.C.Q. Noakes, and P. Bailey, *Medium-energy ion scattering studies of two-dimensional rare-earth silicides*. Phys. Rev. B, 2000. **61**: p. 5707.
75. Baptist, R., S. Ferrer, G. Grenet, and H.C. Poon, *Surface Crystallography of YSi<sub>2-x</sub> Films Epitaxially Grown on Si(111): An X-Ray Photoelectron Diffraction Study*. Phys. Rev. Lett., 1990. **64**(3): p. 311.

76. Martín-Gago, J.A., J.M. Gómez-Rodríguez, and J.Y. Veuillen, *Growth and morphology of epitaxial ErSi<sub>1.7</sub> films on Si(111)7×7 studied by scanning tunneling microscopy*. Surf. Sci., 1996. **366**: p. 491-500.
77. Roge, T.P., F. Palmino, C. Savall, J.C. Labrune, P. Wetzel, C. Pirri, and G. Gewinner, *Surface reconstruction of ErSi<sub>1.7</sub>(0001) investigated by scanning tunneling microscopy*. Phys. Rev. B, 1995. **51**(16): p. 10998.
78. Tuilier, M.-H., P. Wetzel, C. Pirri, D. Bolmont, and G. Gewinner, *Interfacial structure of two-dimensional epitaxial Er silicide on Si(111)*. Phys. Rev. B, 1994. **50**: p. 2333.
79. Martín-Gago, J.A. and J.M. Gómez-Rodríguez, *Surface atomic structure of epitaxially grown erbium silicide films on Si(111)7×7*. Phys. Rev. B, 1997. **55**(8): p. 5136.
80. Lee, Y.K., N. Fujimura, and T. Ito, *Epitaxial-Growth of Yttrium Silicide YSi<sub>2-x</sub> on (100) Si*. J. Alloys and Compounds, 1993. **193**(1-2): p. 289-291.
81. Lee, Y.K., N. Fujimura, T. Ito, and N. Itoh, *Epitaxial-Growth and Structural Characterization of Erbium Silicide Formed on (100)Si Through a Solid-Phase Reaction*. J. Cryst. Growth, 1993. **134**(3-4): p. 247-254.
82. Geröcs, I., G. Molnár, E. Járóli, E. Zsoldos, G. Petö, and J. Gyulai, *Epitaxy of orthorhombic gadolinium disilicide on <100> silicon*. Appl. Phys. Lett., 1987. **51**(25): p. 2144.
83. Molnár, G., G. Petö, E. Zsoldos, Z.E. Horváth, and N.Q. Khanh, *The effect of silicon substrate orientation on the formation of Gd-silicide phases*. Appl. Surf. Sci., 1996. **102**: p. 159-162.
84. Frangis, N., G. Van.Tendeloo, J. Van.Landuyt, G. Kaltsas, A. Travlos, and A.G. Nassiopoulou, *New Erbium Silicide Superstructures: A Study by High Resolution Electron Microscopy*. phys. stat. sol. (a), 1996. **158**: p. 107.
85. Travlos, A., N. Salamouras, and E. Flouda, *Epitaxial erbium silicide films on (100) silicon: growth, structure and electrical properties*. Appl. Surf. Sci., 1997. **120**: p. 355-364.

86. Henle, W.A., M.G. Ramsey, and F.P. Netzer, *The gadolinium-Si(100)2×1 interface*. Surf. Sci., 1991. **243**: p. 141-150.
87. Pasquali, L., S. D'Addato, and S. Nannarone, *Growth of epitaxial Yb silicide on Si(100) studied by metastable atom deexcitation spectroscopy and photoemission*. Phys. Rev. B, 2002. **65**: p. 115417.
88. Zur, A. and T.C. McGill, *Lattice match: An application to heteroepitaxy*. J. Appl. Phys., 1984. **55**(2): p. 378.
89. Gottlieb, U., F. Nava, M. Affronte, O. Laborde, and R. Madar, *Electrical transport in metallic TM silicides*, in *Properties of Metal Silicides*, K. Maex and M.V. Rossum, Editors. 1995, INSPEC: London. United Kingdom. p. 189.
90. Gottlieb, U., F. Nava, M. Affronte, O. Laborde, and R. Madar, *Electrical transport in semiconducting TM silicides*, in *Properties of Metal Silicides*, K. Maex and M.V. Rossum, Editors. 1995, INSPEC: London. United Kingdom. p. 205.
91. d'Heurle, F.M., *Silicide Interfaces in Silicon Technology*. Journal of Electronic Materials, 1998. **27**(11): p. 1138.
92. Unewisse, M.H. and J.W.V. Storey, *Electrical and infrared investigation of erbium silicide*. J. Appl. Phys., 1992. **72**(6): p. 2367.
93. Xu, Z., *Electrical transport in RE silicides*, in *Properties of Metal Silicides*, K. Maex and M.V. Rossum, Editors. 1995, INSPEC: London, United Kingdom. p. 217.
94. Guizzetti, G., E. Mazzega, M. Michelini, F. Nava, A. Borghesi, and A. Piaggi, *Electrical and optical characterization of GdSi<sub>2</sub> and ErSi<sub>2</sub> alloy thin films*. J. Appl. Phys., 1990. **67**(7): p. 3393.
95. Duboz, J.Y., P.A. Badoz, F.A. d'Avitaya, and J.A. Chroboczek, *Electronic transport properties of epitaxial erbium silicide/silicon heterostructures*. Appl. Phys. Lett., 1989. **55**(1): p. 84.
96. Woodruff, D.P. and T.A. Delchar, *Modern Techniques of Surface Science*. 2nd ed. 1994: Cambridge University Press.

97. Kubby, J.A. and J.J. Boland, *Scanning tunneling microscopy of semiconductor surfaces*. Surf. Sci. Rep., 1996. **26**: p. 61-204.
98. Appelbaum, J.A., G.A. Baraff, and D.R. Hamann, *Si(100) Surface Reconstruction: Spectroscopic Selection of a Structural Model*. Phys. Rev. Lett., 1975. **35**(729).
99. Becker, R. and R. Wolkow, *Semiconductor surfaces*, in *Scanning tunneling microscopy*, J.A. Stroscio and W.J. Kaiser, Editors. 1993, Academic Press: San Diego. p. 149.
100. Zhang, Z., F. Wu, and M.G. Legally, *An atomistic view of Si(001) homoepitaxy*. Ann. Rev. Mater. Sci., 1997. **27**: p. 525.
101. Chadi, D.J., *Stabilities of single-layer and bilayer steps on Si(001) surfaces*. Phys. Rev. Lett., 1987. **59**: p. 1691.
102. Stroscio, J.A. and W.J. Kaiser, eds. *Scanning Tunneling Microscopy*. Methods of Experimental Physics. Vol. 27. 1993, Academic Press, Inc.: San Diego.
103. Vickerman, J.C., ed. *Surface Analysis - The Principal Techniques*. 1997, John Wiley & Sons Ltd.
104. Baski, A.A., *Scanning Tunneling Microscopy of Metal Growth and Reconstruction on Si(100) and Si(111)*, in *Edward L. Ginzton Laboratory*. 1991, Stanford University: Stanford, California.
105. <http://reg.ssci.liv.ac.uk/>.
106. Magaud, J., A. Pasturel, G. Kresse, and J. Hafner, *Role of silicon vacancies in yttrium-disilicide compounds from ab-initio calculations*. Phys. Rev. B, 1997. **55**(20): p. 13479.
107. Chen, G., J. Wan, J. Yang, X. Ding, L. Ye, and X. Wang, *Surface structures of erbium silicide ultra-thin films formed by solid phase epitaxy on Si(100)*. Surf. Sci., 2002. **513**(1): p. 203.



108. Matthews, J.W., *Misfit Dislocations*, in *Dislocations in Solids*, F.R.N. Nabarro, Editor. 1979, North-Holland Publishing Company. p. 463.
109. Palmstrøm, C.J., *Epitaxy of Dissimilar Materials*. Ann. Rev. Mater. Sci., 1995. **25**: p. 389-415.
110. Gao, H. and W.D. Nix, *Surface roughening of heteroepitaxial thin films*. Ann. Rev. Mater. Sci., 1999. **29**: p. 173-209.
111. Andrews, A.M. and J.S. Speck, *Modeling cross-hatch surface morphology in growing mismatched layers*. J. Appl. Phys., 2002. **91**(4): p. 1933.
112. Chang, K.H., R. Gibala, D.J. Srolovitz, P.K. Bhattacharya, and J.F. Mansfield, *Crosshatched surface morphology in strained III-V semiconductor films*. J. Appl. Phys., 1990. **67**(9): p. 4093.
113. Lu, W. and Z. Suo, *Symmetry breaking in self-assembled monolayers on solid surfaces: Anisotropic surface stress*. Phys. Rev. B, 2002. **65**: p. 85401.
114. Suo, Z. and W. Lu, *Forces that drive nanoscale self-assembly on solid surfaces*. Journal of Nanoparticle Research, 2000. **2**: p. 333-344.
115. Baglin, J.E.E., F.M. d'Heurle, and C.S. Petersson, *Diffusion marker experiments with rare-earth silicides and germanides: Relative mobilities of the two atom species*. J. Appl. Phys., 1981. **52**(4): p. 2841.
116. Lipson, H. and K.E. Singer, *Disorder in a film of gold deposited on silicon: investigation by low-energy electron diffraction*. J. Phys. C: Solid State Phys., 1974. **7**: p. 12.
117. Ohbuchi, C. and J. Nogami, *Holmium growth on Si(001): surface reconstructions and nanowire formation*. Phys. Rev. B, 2002. **66**: p. 233305.
118. Wetzel, P., C. Pirri, P. Paki, D. Bolmont, and G. Gewinner, *Structure of a two-dimensional epitaxial Er silicide on Si(111) investigated by Auger-electron diffraction*. Phys. Rev. B, 1993. **47**: p. 3677.
119. Katkov, M.V. and J. Nogami, *Yb and Nd growth on Si(001)*. Surf. Sci., 2002.

120. Heath, J.R., P.J. Kuekes, G.S. Snider, and R.S. Williams, *A defect-tolerant computer architecture: opportunities for nanotechnology*. Science, 1998. **280**: p. 1716.
121. Molnár, G., G. Petö, and E. Zsoldos, *Solid phase reaction and epitaxy of Gd-silicide films on Si substrates*. Appl. Surf. Sci., 1993. **70/71**: p. 466.
122. Trampert, A. and K.H. Ploog, *Heteroepitaxy of large-misfit systems: role of coincidence lattice*. Cryst. Res. Technol., 2000. **35**(6-7): p. 793-806.
123. Zur, A., T.C. McGill, and M.-A. Nicolet, *Transition-metal silicides lattice-matched to silicon*. J. Appl. Phys., 1985. **57**(2): p. 600.
124. Tersoff, J. and R.M. Tromp, *Shape transition in growth of strained islands - spontaneous formation of quantum wires*. Phys. Rev. Lett., 1993. **70**: p. 2782.
125. Grinfeld, M.A., *The stress driven "rearrangement" instability in crystalline films*. J. Intell. Mater. Syst. Struct., 1993. **4**(76).
126. Grilhe, J., *Study of roughness formation induced by homogeneous stress at the free surfaces of solids*. Acta metall. mater., 1993. **41**(3): p. 909.
127. Cullis, A.G., *Strain-induced modulations in the surface morphology of heteroepitaxial layers*. MRS Bulletin, 1996. **April**: p. 21.
128. Voigtländer, B., *Fundamental process in Si/Si and Ge/Si epitaxy studied by scanning tunneling microscopy during growth*. Surf. Sci. Rep., 2001. **43**: p. 127.
129. Teichert, C., *Self-organization of nanostructures in semiconductor heteroepitaxy*. Physics Reports, 2002. **365**: p. 335-432.
130. Bauer, E.G., et al., *Fundamental issues in heteroepitaxy-A Department of Energy, Council on Materials Science Panel Report*. J. Mater. Res., 1990. **5**(4): p. 852.
131. Schowalter, L.J., *Heteroepitaxy and Strain: Applications to Electronic and Optoelectronic Materials*. MRS Bulletin, 1996(April): p. 18.

132. Sze, S.M., *Physics of semiconductor devices*. 1981, New York: John Wiley & Sons.
133. Markov, I., *Recent theoretical developments in epitaxy*. Mater. Chem. Phys., 1993. **36**: p. 1-30.
134. Shchukin, V.A. and D. Bimberg, *Spontaneous ordering of nanostructures on crystal surfaces*. Rev. Mod. Phys., 1999. **71**(4): p. 1125.
135. Daruka, I. and A.-L. Barabási, *Dislocation-free island formation in heteroepitaxial growth: a study at equilibrium*. Phys. Rev. Lett., 1997. **79**(19): p. 3708.
136. Bean, J.C., L.C. Feldman, A.T. Fiory, S. Nakahara, and I.K. Robinson, *Ge<sub>x</sub>Si<sub>1-x</sub>/Si strained-layer superlattice grown by molecular beam epitaxy*. J. Vac. Sci. Technol. A, 1984. **2**: p. 436.
137. Snyder, C.W., B.G. Orr, D. Kessler, and L.M. Sander, *Effect of strain on surface morphology in highly strained InGaAs films*. Phys. Rev. Lett., 1991. **66**: p. 3032.
138. Leonard, D., K. Pond, and P.M. Petroff, *Critical layer thickness for self-assembled InAs islands on GaAs*. Phys. Rev. B, 1994. **50**: p. 11687.
139. Pashley, D.W., *The nucleation, growth, structure and epitaxy of thin surface films*. Advances in physics, 1965. **14**: p. 327.
140. vanderMerwe, J.H. and C.A. Ball, in *Epitaxial growth*, J.W. Matthews, Editor. 1975, Academic: New York. p. 493.
141. Fitzgerald, E.A., *Dislocations in strained-layer epitaxy - theory, experiment, and applications*. Mater. Sci. Rep., 1991. **7**(3): p. 91.
142. Politi, P., G. Grenet, A. Marty, A. Ponchet, and J. Villain, *Instabilities in crystal growth by atomic or molecular beams*. Phys. Rep., 2000. **324**: p. 271-404.
143. Kern, R., G. LeLay, and J.J. Metois, in *Current topics in materials science, vol.3*, E. Kaldis, Editor. 1979, North-Holland: Amsterdam. p. 128-419.

144. Markov, I. and S. Stoyanov, *Mechanisms of epitaxial-growth*. Contemp. Phys., 1987. **28**: p. 267.
145. Raviswaran, A., C.P. Liu, J. Kim, D.G. Cahill, and J.M. Gibson, *Evolution of coherent islands during strained-layer Volmer-Weber growth of Si on Ge(111)*. Phys. Rev. B, 2001. **63**(12): p. 125314.
146. LeGoues, F.K., *The effect of strain on the formation of dislocations at the SiGe/Si interface*. MRS Bulletin, 1996. **April**: p. 38.
147. Lutz, M.A., R.M. Feenstra, F.K. LeGoues, P.M. Mooney, and J.O. Chu, *Influence of misfit dislocations on the surface morphology of  $\text{Si}_{1-x}\text{Ge}_x$  films*. Appl. Phys. Lett., 1995. **66**(6): p. 724.
148. Guyer, J.E. and P.W. Voorhees, *Morphological stability of alloy thin films*. Phys. Rev. Lett., 1995. **74**: p. 4031.
149. Xie, Y.H., et al., *Semiconductor surface roughness: dependence on sign and magnitude of bulk strain*. Phys. Rev. Lett., 1994. **73**: p. 3006.
150. Jesson, D.E., K.M. Chen, and S.J. Pennycook, *Kinetic pathways to strain relaxation in the Si-Ge system*. MRS Bulletin, 1996. **April**: p. 31.
151. Eaglesham, D.J. and M. Cerullo, *Dislocation-free Stranski-Krastanow growth of Ge on Si(100)*. Phys. Rev. Lett., 1990. **64**(16): p. 1943.
152. Koch, R., G. Welder, and B. Wassermann, *Evolution of stress and strain relaxation of Ge and SiGe alloy films on Si(001)*. Appl. Surf. Sci., 2002. **190**(1-4): p. 422.
153. Tillmann, K. and A. Forster, *Critical dimensions for the formation of interfacial misfit dislocations of  $\text{In}_{0.6}\text{Ga}_{0.4}\text{As}$  islands on GaAs(001)*. Thin Solid Films, 2000. **368**(1): p. 93.
154. Ramachandran, T.R., A. Madhukar, I. Mukhametzhanov, R. Heitz, A. Kalburge, Q. Xie, and P. Chen, *Nature of Stranski-Krastanow growth of InAs on GaAs(001)*. J. Vac. Sci. Technol. B, 1998. **16**(3): p. 1330.

155. Nötzel, R., *Self-organized growth of quantum-dot structures*. Semicond. Sci. Technol., 1996. **11**: p. 1365-1379.
156. Zhang, Y.W., *Self-organization, shape transition, and stability of epitaxially strained islands*. Phys. Rev. B, 2000. **61**(3): p. 10388.
157. García, J.M., L. González, M.U. González, J.P. Silveira, Y. González, and F. Briones, *InAs/InP(001) quantum wire formation due to anisotropic stress relaxation: in situ stress measurements*. J. Cryst. Growth, 2001. **227-228**: p. 975.
158. Omi, H. and T. Ogino, *Self-assembled Ge nanowires grown on Si(113)*. Appl. Phys. Lett., 1997. **71**(15): p. 2163.
159. Loretto, D., F.M. Ross, and C.A. Lucas, *Quasi-one-dimensional CaF<sub>2</sub> islands formed on Si(001) by molecular beam epitaxy*. Appl. Phys. Lett., 1996. **68**(17): p. 2363.
160. Pasquali, L., S. D'Addato, G. Selvaggi, S. Nannarone, N.S. Sokolov, S.M. Sutorin, and H. Zogg, *Formation of CaF<sub>2</sub> nanostructures on Si(001)*. Nanotechnology, 2001. **12**: p. 403.

MICHIGAN STATE UNIVERSITY LIBRARIES



3 1293 02328 8289